Chronic stress induces activity, synaptic and transcriptional remodeling of the lateral habenula associated with deficits in motivated behaviors

By

Ignas Cerniauskas

A dissertation submitted in partial satisfaction of the

requirements for the degree of

Doctor of Philosophy

in

Neuroscience

in the

Graduate Division

of the

University of California, Berkeley

Committee in charge:

Professor Stephan Lammel, Chair

Professor Hillel Adesnik

Professor Helen S. Bateup

Professor Linda Wilbrecht

Fall 2019

Abstract

Chronic stress induces activity, synaptic and transcriptional remodeling of the lateral habenula associated with deficits in motivated behaviors

by

Ignas Cerniauskas

Doctor of Philosophy in Neuroscience

University of California, Berkeley

Professor Stephan Lammel, Chair

Chronic stress is a major risk factor for the development of depression. In recent years, the lateral habenula (LHb) has emerged as a potential key structure in depression. LHb is connected with dopaminergic neurons in the ventral tegmental area (VTA) and serotoninergic neurons in the dorsal raphe nucleus (DR), and changes in these monoaminergic systems have been associated with depression-related behaviors. In my dissertation, I demonstrate that chronic stress-induced hyperactivity in LHb neurons projecting to VTA is associated with increased passive coping but not anxiety or anhedonia. Moreover, LHb→VTA neurons in mice with increased passive coping show increased burst and tonic firing as well as synaptic adaptations in excitatory inputs from the entopeduncular nucleus (EP). In vivo manipulations of EP→LHb or LHb→VTA neurons also selectively alter passive coping and effort-related motivation. Conversely, dorsal raphe (DR)-projecting LHb neurons do not show chronic stress-induced hyperactivity and are targeted indirectly by the EP. Using single-cell transcriptomics I reveal a set of genes that can collectively serve as biomarkers to identify mice with increased passive coping phenotype and differentiate LHb→VTA from LHb→DR neurons. Together, I provide a set of biological markers at the level of genes, synapses, cells and circuits that define a distinctive chronic stress-induced behavioral phenotype.

TABLE OF CONTENTS

PUBLICATION RELATED TO THIS WORK

My dissertation contains work that has been previously published:

Cerniauskas, I., Winterer, J., de Jong, J. W., Lukacsovich, D., Yang, H., Khan, F., Peck, J., Obayashi, K. S., Lilascharoen, V., Lim, B. K., Földy, C., Lammel, S. (2019) Chronic stress induces activity, synaptic and transcriptional remodeling of the lateral habenula associated with deficits in motivated behaviors. Neuron *104*, 899-915.

CHAPTER 1: INTRODUCTION

Heterogeneity of major depressive disorder

Depression, or major depressive disorder, is a mental disorder that dramatically affects a person's health and life. It is characterized by persistent low mood, inability to feel pleasure in previously enjoyable activities, feeling of low-esteem, fatigue, sleep disturbances, appetite changes, pain without a clear cause, and thoughts of suicide. It has become the leading cause of disability worldwide with over 300 million people affected. The prevalence of major depressive disorder increased by 18% from 2005 to 2015 (World Health Organization, 2017). Depression is also a chronic disease, as half of a people who experienced a single episode are likely to have recurrent episodes with higher frequency and severity (Akil et al., 2018).

Even though major depressive disorder is diagnosed as a single entity, it is a really heterogeneous disorder characterized by patients having widely varied symptoms, with little to even no overlap of symptomatologies in some cases (Akil et al., 2018). This heterogeneity of depression hinders both research and treatment of this highly prevalent disorder (Fried, 2017). Antidepressants available on the market today were developed based on a theory called monoamine hypothesis of depression, which was established on several key observations made in 1950s. The hypothesis states that the underlying biological reason for depression is depletion of dopamine, serotonin, and/or norepinephrine levels in the central nervous system. It has been demonstrated that increasing the levels of the aforementioned monoamine neurotransmitters in the brain, either by blockage of their reuptake or inhibition of their degradation, alleviates the depression symptoms in patients (Delgado, 2000; Hirschfeld, 2000).

Despite the relative effectiveness of currently available antidepressant medications, they are still lacking and possess a variety of drawbacks. Less than half of the patients achieve full remission after the first treatment with antidepressants (Rush, 2007). That leads to trial-and-error approach, where multiple trials of different treatment are needed until the patient is matched with optimal medication. Even then, for patients that do respond to treatment, it takes weeks or months until the depressive symptoms are alleviated (Berton and Nestler, 2006). Some patients also exhibit resistance to antidepressants, which can develop spontaneously in patients previously responsive to treatment or as a result of worsening illness over the course of time (Thase and Schwartz, 2015). Moreover, treatment with antidepressants has numerous side effects, such as fatigue, sleep disturbances, weight and appetite, and sexual dysfunction (Fergusson, 2001).

Therefore, there is still an unmet need for more effective, faster, and safer treatment for major depressive disorder. A different approach to depression treatment would be to conceptualize this disease as a circuit dysfunction instead of a neurotransmitter dysfunction. It is possible that the heterogeneity of symptoms observed in depression stems from distinct maladaptive neural circuits. Identifying such neural circuits might advance our understanding of major depressive disorder and lead to development of novel patient-tailored medication.

Habenula as an anatomical hub

In recent years, lateral habenula (LHb) and its associated circuits gained a considerable amount of attention in depression research field. The habenula is located at the most dorsal and caudal part of the thalamus and together with pineal gland forms the epithalamus. The habenula is phylogenetically preserved structure in vertebrates, present in lamprey, fish, reptiles, and mammals

(Concha and Wilson, 2001). In lower vertebrates it is subdivided into dorsal and ventral habenulae, while in mammals it is split into medial (MHb) and lateral habenulae. The subdivision between the MHb and the LHb is based on the connectivity and gene expression profiles of these two subnuclei. MHb is comprised of glutamatergic, cholinergic and substance P releasing neurons. It primarily receives inputs from the septum and projects to the intrapeduncular nucleus (IPN; Viswanath et al., 2014). On the other hand, LHb neurons are mainly glutamatergic as demonstrated by extensive expression of vesicular glutamate transporter VGlut2 (Li et al., 2011; Lammel et al., 2012). A small population of local inhibitory interneurons that express glutamate decarboxylase 2 GAD2 has also been described (Zhang et al., 2018; Flanigan, et al., 2019).

Based on its inputs and outputs, LHb is well positioned to integrated emotion into selection of action. It receives its inputs through stria medullaris and sends its outputs through fasciculus retroflexus. Majority of glutamatergic inputs to LHb arise from lateral hypothalamus (LH), entopeduncular nucleus (EP, known as globus pallidus internal (GPi) in primates), ventral tegmental area (VTA), and cortex, namely anterior cingulate cortex (ACC) and medial prefrontal cortex (mPFC; Li et al., 2011; Kim and Lee, 2012; Shabel et al., 2012; Poller et al., 2013; Lecca et al., 2014). LHb also receives GABAergic inhibition form EPN, ventral pallidum (VP), VTA, and nucleus accumbens (NAc; Shabel et al., 2012; Stamatakis et al., 2013; Lecca et al., 2014; Yang et al, 2018). Dopamine receptors have been detected in LHb (Gruber et al., 2007; Good et al., 2017) and VTA neurons targeting LHb express tyrosine hydroxylase (TH), an indicator of dopaminergic neurons, it is still unclear if these VTA neurons indeed release dopamine in the LHb (Stamatakis et al., 2013; Lammel et al., 2015). Moreover, LHb receives inputs from serotonergic dorsal (DR) raphe nucleus and serotonin receptors have been reported in the LHb (Tchenio et al., 2016).

LHb exerts strong control over midbrain aminergic nuclei, including dopaminergic VTA neurons and serotinergic median raphe (MR) and DR nuclei neurons. Overall effect of LHb neuron activation is inhibitory on the aforementioned aminergic nuclei. Electrical stimulation of LHb neurons inhibits 90% of putative dopaminergic cells in the VTA (Matsumoto and Hikosaka, 2007). Similarly, putative serotonin neurons also stop their firing after stimulation of the LHb (Wang and Aghajanian, 1977). LHb axons target dopaminergic and GABAergic neurons in the VTA to a comparable extent (45% and 52%, respectively; Kaufling et al., 2009). Similarly, in the DR nucleus, LHb innervate both serotonergic neurons and GABAergic interneurons, which provide feedforward inhibition to local serotonin neuron population (Zhou et al., 2017). Given that majority of LHb neurons are excitatory glutamatergic neurons, net inhibitory effects on monoaminergic nuclei cannot be explained by local feedforward inhibition in the VTA and DR nucleus itself. Rostral medial tegmental nucleus (RMTg), previously known as a tail of the VTA, is a purely GABAergic nucleus that receives strong inputs from the LHb and provides strong inhibition to monoaminergic nuclei (Jhou et al., 2009; Kaufling et al, 2009). It has been demonstrated by RMTg lesions, that inhibition of midbrain dopamine neurons by LHb is mainly mediated through RMTg instead of direct projections to the VTA itself (Brown et al, 2017). Stamatakis and Stuber have also shown that excitatory LHb inputs mainly target GABAergic neuronal populations in the RMTg and VTA instead of dopamine neurons (Stamatakis and Stuber, 2012). Nonetheless, there is a distinct LHb subpopulation that directly targets dopaminergic VTA neurons that exclusively project to mPFC (Lammel et al., 2012).

Reward processing by the lateral habenula

Given strong anatomical and functional connectivity between the LHb and midbrain dopamine and serotonin systems, it is not surprising that LHb plays a major role in coding rewarding and aversive stimuli in the brain. One of the most important characteristics of an organism is its ability to react to sensory cues and salient stimuli in order to maximize survival and rewards while avoiding threatening and punishing events. Such behaviors are thought to be controlled by brain reward system which consists of circuits involving forebrain limbic system and its connections to the midbrain aminergic centers (Wise, 2004; Cools et al., 2011). Animals are able to change their behavior based on stimuli by forming representations of the predicted value of performing certain actions. Dopamine neurons in VTA are critical for such action evaluation by signaling a discrepancy between the action outcome and the predicted value of the outcome, which is often referred to as reward prediction error (RPE). When the actual reward of a behavior is higher than the predicted reward (positive RPE), activity of dopamine neurons increases and such behavior is facilitated. On the other hand, when the actual reward of an action is lower than the predicted value (negative RPE), dopamine neuron activity is inhibited and actions leading to such rewards are suppressed (Schultz, 2016). Several recent studies have demonstrated that LHb neurons might provide reward-related signals to VTA. In a function magnetic resonance imaging (fMRI) experiment, humans performing a motion-prediction task had higher activity in their LHb when they have been told that their response in the task was wrong (Ullsperger and von Cramon, 2013). Using single cell *in vivo* electrophysiology recordings in macaque monkeys performing a visual saccade task with positionally-biased reward outcomes, Matsumoto showed that LHb neurons code negative RPE. LHb neurons were inhibited when the reward-predicting saccade was performed. However, when a no-reward-predicting saccade was performed, LHb neurons were excited. Similarly, LHb activity was also increased when monkeys were presented with aversive stimuli, such as an air puff to an eye (Matsumoto and Hikosaka, 2007).

Negative RPE signals observed in LHb are complete opposite to classical RPE seen in dopamine neurons in VTA, indicating that LHb contributes to reinforcement learning through inhibitory action, possibly through RMTg, on dopamine neurons. In fact, acute exposure to aversive stimuli, such as an electrical foot shock, increases excitatory neurotransmission in LHb-to-RMTg pathway. Optogenetic stimulation of LHb-to-RMTg projection also produces behavioral avoidance in real time place aversion task (Stamatakis and Stuber, 2012). Furthermore, stimulation of RMTg projections to VTA produces behavioral avoidance and inhibition of this pathway promotes conditioned place preference, most likely through removal of tonic inhibition from RMTg neurons onto VTA dopamine cells (Jhou et al., 2013).

Beyond reward-based decision making, LHb neurons are also involved in avoiding punishment. LHb have been shown to be excited by painful or aversive stimuli (Dafny and Qiao, 1990; Matsumoto et al., 1994). Recent optogenetic studies examined on how certain inputs and outputs of LHb might be controlling aversive processing. One of the strongest inputs to LHb arise from EP, a basal ganglia output nucleus that has similar reward responses as LHb neurons, i.e. it is excited by aversive stimuli and inhibited by rewards (Hong and Hikosaka, 2008). This suggest that excitatory projections from EP signal aversive stimuli. Shabel showed that EP input to LHb is mainly excitatory and that optogenetic activation of these inputs onto the LHb triggers avoidance of the environment where the stimulation happened (Shabel et al., 2012). Another major input to LHb, lateral hypothalamus, has been shown to be important in aversive behaviors, as stimulation of putative glutamatergic neurons in LH produced aversive behavioral phenotypes (Jennings et al.,

2013). In the follow up work, Stuber's lab demonstrated that LH-to-LHb modulation bidirectionally control reward, by increasing LHb neuronal activity, to suppress ongoing behavior, or decreasing glutamatergic tone in the LHb to promote ongoing behavior (Stamatakis et al., 2016).

Furthermore, aversive LHb signaling is modulated by a unique VTA GABAergic population that expresses tyrosine hydroxylase, which indicates that this population might also release dopamine. Stimulation of these GABAergic terminals suppressed the firing of LHb neurons and in turn increased firing of VTA dopamine neurons. *In vivo* activation of this pathway produced reward-related phenotypes suggesting that activity of the inhibitory neurons in VTA can suppress LHb output during rewarding conditions (Stamatakis et al., 2013). A different study showed VTA neurons targeting LHb that coexpress markers for both glutamate signaling and GABA signaling and form both symmetric and asymmetric synapses on the same LHb neurons. This indicates that such VTA-to-LHb neurons might represent a unique population of cells being able to release both glutamate and GABA from their axon terminals. Stimulation of such terminals was able to excite or inhibit LHb neurons, probably dependent on the activity pattern or membrane potential of individual postsynaptic LHb neurons (Root et al., 2014). Another inhibitory input to LHb is provided by basal forebrain and can bidirectionally control the valence of aggressive interactions. Activation of GABAergic BF terminals of non-aggressors decreases LHb neuronal firing and promotes conditioned place preference to the intruder-paired context. Silencing of GABAergic BF terminals of aggressors increases LHb neuronal firing and abolishes CPP to the intruder-paired context. These results reveal a novel role of the BF-to-LHb circuit in modulating reward in aggression context during social behaviors (Golden et al., 2016). Altogether, the aforementioned findings show how different inputs to LHb can shape its processing of aversive information.

Lateral habenula in depressive disorders

Considering that LHb plays such a pivotal role in aversive information processing as well as exerts strong control of dopamine and serotonin systems, it is reasonable to suspect that dysfunction of LHb activity could be linked to depressive disorders. There are numerous studies, both in humans and animal models of depression, showing increased activity of LHb in depression. In human volunteers, reduction of serotonin levels using tryptophan depletion induced depressive phenotype. Using positron emission tomography (PET) showed one of the few brain areas with increased activity in such subjects was LHb (Morris et al., 1999). These findings are consistent with the study carried out by Shumake et al., where they used congenitally helpless rats as their animal model of depression, where animals are selectively bred to display an immediate helpless response to stress. After comparing regional brain metabolism between congenitally helpless and non-helpless rats using quantitative cytochrome oxidase histochemistry, researchers observed increased metabolic activity, corresponding to higher neural activity, in LHb and decreased metabolism in VTA (Shumake et al., 2003). Accordingly, rats exposed to chronic mild stress developed depression-like behavioral phenotype which was accompanied by serotonin level reduction in DR. Interestingly, LHb lesion improved depression-like behaviors as well as well as increased serotonin levels in DR (Yang et al., 2008). Similarly, $GABA_A$ receptor agonist muscimol injections, which effectively reduces neural activity, into the LHb of congenitally helpless rats reduced depression like behavior, but only one week later after the intervention (Winter et al., 2011). The LHb also appears to be sensitive to neuromodulators, as microinjections of substance P agonist into the LHb produced depression-like phenotype in forced swim test in rats. On the other hand, microinjections of substance P antagonist reduced the depression-like behavior in

forced swim test, which might be mediated through increased serotonin levels in DR. Even though this study provides interesting clues, causal link between substance P and LHb neural activity needs further investigation (Yang et al., 2014).

Together these findings show that in general aberrant LHb neural activity, and most likely increased LHb activity, promotes depressive disorder. That presents an exciting opportunity that decreasing lateral habenula activity might be a potential target for novel therapeutics. It has been proposed that deep-brain stimulation (DBS), which effectively reduces neuronal hyperexcitability, in the LHb could alleviate some of the depression symptoms. Meng et al. performed unilateral LHb DBS in rats exposed to chronic mild stress. DBS not only improved depressive-like symptoms in this animal model of depression, but also was followed by increased concentration of norepinephrine, dopamine, and serotonin in the blood plasma as well as brain tissue (Meng et al., 2011). In a single patient study, bilateral stimulating electrodes were implanted in stria medularis, a major afferent bundle of the LHb. The patient, who was therapy-resistant to all standard treatments for at least 9 years and suffered from severe major depressive disorder for 46 years, showed sustained full remission of depressive symptoms after the DBS procedure. Interestingly, once the DBS was switched off for a short period of time, patient relapsed, but showed full remission again once the DBS was switched on. DBS did not produce acute antidepressant effects and 4 months of stimulation were required for a full remission, which suggests that neural plasticity changes in mood-regulatory circuits are required in recovery from depression (Sartorius et al., 2010).

Recent studies also started investigating molecular and neural circuit mechanisms associated with LHb hyperactivity in various animal models of depression. Using acute learned helplessness, where animals are exposed to periods of inescapable and unpredictable shock, and congenital learned helplessness animal models of depressions, Li et al. investigated activity changes in LHb neurons projecting to VTA. In both models of depression there was an increase in frequency, but not the amplitude, of miniature excitatory postsynaptic currents (mEPSCs) onto this LHb subpopulation, indicating stronger excitatory drive onto LHb after stress. These measures correlated with helplessness observed in individual animals. They also recorded spontaneous spiking rate measured in a cell-attached configuration in slice preparation and also saw an increase in spontaneous firing in LHb-to-VTA neurons compared to the control animals. Lastly, DBS protocol of LHb afferents, which depletes transmitter release, reduced excitatory synaptic drive onto this LHb subpopulation and improved depression-like behavior in the animals assessed by measuring the immobility rate in the forced swim test paradigm (Li et al., 2011). It is possible that these LHb neurons target VTA neuronal population specifically targeting mPFC, which has been shown to produce aversion in mice (Lammel et al., 2012). A separate study exposed mice to repeated foot shocks and recorded from LHb neurons projecting to RMTg using slice electrophysiology. Repeated aversive stimuli increased excitatory synaptic drive onto LHb-to-RMTg neurons, as indicated by increased mEPSCs frequency and increased synaptic release probability observed in paired-pulse ratio stimulation protocol. Moreover, activation of LHb inputs to the RMTg produced active behavioral avoidance and disrupted positive reinforcement (Stamatakis and Stuber, 2012). Altogether, these studies demonstrated that LHb receives increased excitatory synaptic drive in depressive phenotypes, which could translate to increased inhibition of dopamine and serotonin systems.

In order to search for the molecular mechanism underlying habenular hyperactivity, Li et al. initiated quantitative proteomic screening to compare habenular protein expression of wild-type

controls with that of congenitally learned helpless rats. They found significant selective upregulation of the β form of calcium/calmodulin-dependent protein kinase type II (βCaMKII) in their animal model of depression. However, after the helpless rats were treated with antidepressants, βCaMKII was downregulated. Overexpression of βCaMKII in wild type animals induced depressive-like phenotype, indicated by longer immobility time in a forced swim test paradigm and a reduced sucrose preference. Overexpression also increased *in vitro* firing rate of LHb neurons and increased mEPSCs frequency as well as amplitude, the latter being mediated by higher insertion of α-amino-3-hydroxy-5-methyl-4-isoxazolepropionic acid receptor (AMPAR) GluR1 subunit. Accordingly, knock-down of βCaMKII rescued depression-like behaviors and abolished increased mEPSCs frequency onto LHb neurons (Li et al., 2013). These findings identified βCaMKII as regulator of LHb neuron function and a potential molecular target for depression treatment.

The ventral pallidus (VP) is an important convergent region within the motivational and reward circuitry, and has been implicated in depression, and it sends strong inputs to LHb. Knowland et al. showed that in animals susceptible to social defeat stress exposure there is an increase in hyperexcitability in VP neurons projecting to LHb, which is reversed by chronic antidepressant treatment. Interestingly, optogenetic and chemogenetic manipulations of VP-to-LHb pathway did not modulate social withdrawal, a hallmark depressive-like phenotype induced by social defeat stress. Nonetheless, inhibiting VP-to-LHb pathway attenuated behavioral despair in tail suspension test (Knowland et al., 2017).

Apart from excitatory glutamatergic input changes in depression, LHb also undergoes adaptions involving inhibitory GABAergic transmission. Exposure to unpredictable foot shock, leads to development of depressive-like symptoms in mice, which is accompanied by increased LHb neuron excitability in slice preparation as measured by depolarizing current injections. This heightened excitability is mediated by increased activity of protein phosphatase 2A (PP2A), which in turn leads to internalization of GABAB receptor (GABABR) and G protein–gated inwardly rectifying potassium (GIRK) channel complex. Due to the aforementioned molecular changes, LHb neurons experience rapid and persistent weakening of GABAB-activated GIRK-mediated (GABAB-GIRK) currents. Pharmacological inhibition of PP2A restored both GABAB-GIRK function and neuronal excitability. Accordingly, *in vivo* PP2A inhibition ameliorates depression-like symptoms after foot shock exposure and in a learned helplessness model of depression (Lecca et al., 2016). In addition to postsynaptic inhibitory adaptions in LHb neurons in depression models, presynaptic changes of GABA release has also been reported. Researchers found co-release of GABA (which is inhibitory) and glutamate (which is excitatory) from individual EP terminals and vesicles onto LHb neurons. This unique GABA/glutamate co-release could control LHb activity based on ratio of GABA/glutamate released. In congenitally helpless rats, GABA/glutamate release ratio was reduced, thereby increasing the net depolarizing drive to the LHb from the EP. In contrast, chronic treatment with an antidepressant citalopram increased the GABA/glutamate ratio (Shabel et al., 2014).

Two recent studies also demonstrated how glia regulates LHb hyperactivity in an animal model of depression. Using a high-throughput quantitative proteomic screen, researchers identified an astroglial potassium channel (Kir4.1) that is upregulated in the LHb in rat models of depression. Astrocytes expressing this Kir4.1 channel tightly wrap around the somas of LHb neurons. During depression, upregulation of Kir4.1 may cause enhanced extracellular K+ clearance, leading to a decrease in extracellular K+ concentration around the LHb neurons. Reduction of extracellular K+

concentrations facilitates the ability of LHb neurons to enter a hyperpolarized state. Hyperpolarized resting membrane potential of LHb neurons in animals with depressive-phenotype activates T-type voltage-sensitive calcium channels (T-VSCCs), which together with N-methyl-D-aspartate receptors (NMDARs) promote burst firing in LHb neurons. Cui et al. showed that overexpression of Kir4.1 in LHb astrocytes increased the burst firing of local LHb neurons and precipitated depression-like behaviors, whereas downregulation of Kir4.1 channel had the opposing effects. Moreover, inducing burst firing in LHb neurons in wild type mice also promoted depression-like phenotypes. Excitingly, blocking NMDAR-dependent bursting by ketamine, a potent NMDAR blocker and a fast acting antidepressant in humans, reducing bursting in LHb and ameliorated depressive symptoms in their animal model of depression (Yang et al., 2018; Cui et al., 2018).

Recent decade was marked by an increased interest in the LHb and its involvement in major depression disorder. Numerous studies demonstrated LHb hyperactivity in depression, proposed molecular mechanisms that could lead to such hyperactivity, and highlighted circuit adaptations promoting LHb excitability and how LHb circuitry changes affect the rest of the brain. Nonetheless, further study of LHb is required to uncover synaptic adaptations in the LHb that underlie long term changes observed in depression. It is still unclear what exact depression-like phenotypes are controlled by LHb activity. What molecular changes are feasible as targets to reduce LHb hyperactivity? Hopefully, the next decade will provide answers to these questions and that will facilitate development of patient-tailored antidepressant medication.

CHAPTER 2: CRONIC STRESS INDUCES ACTIVITY, SYNAPTIC, AND TRANSCRIPTIONAL REMODELING OF THE LATERAL HABENULA ASSOCIATED WITH DEFICITS IN MOTIVATED BEHAVIORS

INTRODUCTION

Chronic stress (CS) is a major risk factor for the development of depression in humans (Hill et al., 2012; Mazure and Maciejewski, 2003; Willner et al., 2013). This has led to the development of several animal models of depression that have been extensively used in basic research over the last few decades (Czéh et al., 2016; Nestler and Hyman, 2010; Willner, 2017). In these models, rodents are exposed to CS in order to generate a variety of behavioral changes (e.g. anhedonia, social withdrawal), which are thought to reflect some of the core symptoms seen in depressed humans (Berton et al., 2012; Monteggia et al., 2018; Nestler and Hyman, 2010; Willner et al., 1992). Although patients with depression show a highly diverse set of combination of symptoms (Carragher et al., 2009; ten Have et al., 2016; Musil et al., 2018; Willner et al., 2013), scientists often considered CS-exposed animals as a homogeneous population in their search for a pathological mechanism (Agudelo et al., 2014; Cui et al., 2018; Frisbee et al., 2015; Li et al., 2013; Moreines et al., 2017; Ramirez et al., 2015; Schweizer et al., 2009; Seo et al., 2018; Tye et al., 2012; Yang et al., 2018). However, simply dividing animals into "stressed" and "non-stressed" groups may not account for the diversity of behavioral phenotypes that arise in response to CS exposure. Since different behavioral phenotypes presumably involve discrete brain areas and circuits, it is critical to be able to differentiate these behaviors in order to study their underlying neural correlates when searching for symptom-specific therapeutic interventions. To this end, strategies that recognize the heterogeneity of CS-induced behavioral phenotypes and their biological basis remain largely underdeveloped.

In recent years, the lateral habenula (LHb) has emerged as a potential key structure in depression (Lammel et al., 2014; Lecca et al., 2014; Proulx et al., 2014; Sartorius and Henn, 2007; Yang et al., 2017). Increased neural and metabolic activity of the LHb has been observed in various animal models of depression (Li et al., 2011; Mirrione et al., 2014; Shumake et al., 2003; Tchenio et al., 2017), and elevated LHb firing and depression-related behaviors can be reversed by antidepressant treatment and by employing a deep brain stimulation (DBS)-like protocol in rodents (Li et al., 2011; Tchenio et al., 2017; Yang et al., 2018). Notably, DBS of the LHb caused a marked reduction of depression symptoms in a therapy-refractory patient, with interruption of the stimulation rapidly leading to the recurrence of depressive periods (Kiening and Sartorius, 2013; Sartorius et al., 2010). Together, these studies suggest an important role for both CS and LHb hyperactivity in depression.

Here we introduce an unbiased approach that allows us to examine the neurobiological basis of distinct CS-induced behavioral phenotypes in mice. Using this approach, we deconstructed the molecular, synaptic and circuit architecture of the LHb. The identification of biological markers that align with specific CS-induced behavioral phenotypes constitutes an important step for reducing the complexity of depression and the development of more specific treatments of this broad, heterogeneous disease.

RESULTS

Classification of chronic stress-induced behavioral phenotypes

We exposed mice to eight weeks of chronic mild stress (CMS) and subsequently analyzed them using four different behavioral assays. We first assessed anxiety-related behaviors using the elevated plus (EPM). We found that CMS mice spent significantly less time in the open arms in the elevated plus maze (EPM) compared to non-stressed control (CTRL) mice, suggesting that on average these animals develop an anxiety phenotype in response to CMS exposure (Figure 1A, left panel). Next, we used the sucrose preference test (SPT) to assesses an animal's interest in rewarding stimuli. We found that CMS mice exhibited significantly reduced sucrose preference compared to CTRL mice, suggesting that CMS promotes anhedonia-related behavior, which is considered a core symptom of depression in humans (Figure 1B, left panel). Next, mice were tested in the tail suspension test (TST), a behavioral assay in which animals are exposed to an inescapable aversive environment. Mice initially attempt vigorous escape but then transition to a passive coping (PC) state (Koolhaas et al., 1999). PC can be modulated by genetic, behavioral, and pharmacological interventions related to depression (Andalman et al., 2019; Castagné et al., 2011; Cui et al., 2019; Warden et al., 2012; Willner, 2005; Yilmaz et al., 2002) and may be relevant to the pathological motivational impairments seen in major depression in humans. We found that CMS mice struggled significantly less in the TST when compared to CTRL mice (Figure 1C, left panel). Moreover, struggling behavior in the TST was strongly correlated with struggling behavior in the forced swim test (FST) within the same animals (Figures S1A and S1B) (Porsolt et al., 1978), suggesting that these paradigms may assess a similar behavioral phenotype. Lastly, we used a social interaction test (SIT) to assess CMS-induced deficits in sociability behavior, as social withdrawal is a common symptom of depression in humans (Nestler and Hyman, 2010). Surprisingly, we found that both CTRL and CMS mice showed a similar pattern of sociability as measured in their voluntary initiation of social interaction and their preference for social novelty, as measured by the time spent investigating a novel mouse (Figures S1C and S1D). Thus, CMS may distinguish itself from other stress paradigms (e.g. social defeat stress) in regard to the magnitude and quality of the stress response.

Our data from the behavioral screening assays showed a remarkable variability for individual test scores in both CTRL and CMS mice, making it difficult to evaluate the effects of CMS on individual animals. We therefore decided to generate receiver operating characteristic (ROC) curves, which is an objective method that has been used extensively in clinical epidemiology for the evaluation of binary classifiers (Berrar and Flach, 2012; Søreide, 2009; Zou et al., 2007). To generate ROC curves, we used the data from the three behavioral tests that showed statistically significant differences (i.e. EPM, SPT, TST). We then used the ROC curves (Figures 1A-1C, right panels) to calculate optimal cutoff values based on Youden J index (Youden, 1950), which allowed us to make an unbiased decision as to whether an individual animal is positive for a given behavioral phenotype. The cutoff values that have the combination of highest true positive and lowest false positive rates are 181.9 s for the EPM, 60.1% for the SPT and 93.5 s for the TST.

Animals may also exhibit variability being tested positive in the total number of CMS-induced behavioral phenotypes. In order to examine the number of behavioral phenotypes for

individual animals, we used separate cohorts of CTRL (n = 69) and CMS (n = 107) mice that went through the three behavioral tests on three consecutive days (Figure 1D). We then separated both CTRL and CMS mice into four groups according to the number of positive criteria met and assigned them a score between zero and three (D-score). An animal was considered positive for behavioral phenotypes anxiety, anhedonia or passivity if it scored below the respective cutoff value. Strikingly, both CTRL and CMS groups contained animals that were positive for multiple criteria or showed only one or no phenotype (Figures 1E and 1F). Mice that met all three positive criteria represented 19% of the CMS group, while only 3% of CTRL mice fell into this category. Conversely, despite being exposed to CMS, a small group of animals (5%) did not test positive to any behavioral phenotype at all, whereas the percentage of CTRL mice that did not meet positive criteria was much larger (36%; Figures 1G and 1H).

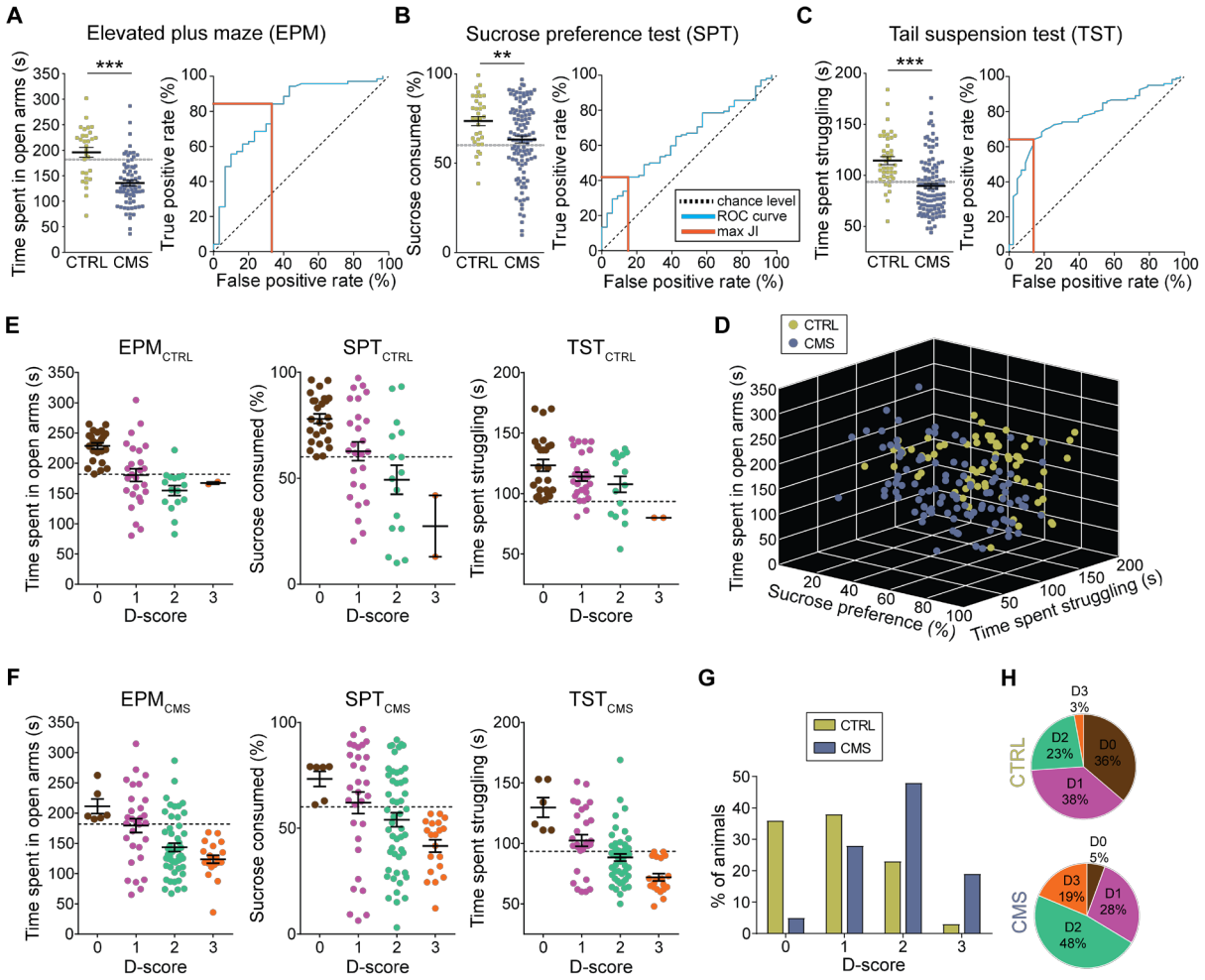

Figure 1. Classification of chronic stress-induced behavioral phenotypes

(A) Left: Time spent in open arms for CTRL (green) and CMS (blue) mice in the EPM; Right: Receiver operating characteristic (ROC) curve (blue line) for EPM data. Orange line: maximum Youden's J index (JI; *** $p < 0.001$, data represent means ± SEM).

(B) Left: Sucrose consumption (%) for CTRL (green) and CMS (blue) mice in the SPT; Right: ROC curve (blue line) for SPT data. Orange line indicates maximum JI (** $p < 0.01$, data represent means ± SEM).

(C) Left: Time spent struggling for CTRL (green) and CMS (blue) mice in the TST; Right: ROC curve (blue line) for TST data. Orange line indicates maximum JI (*** $p < 0.001$, data represent means ± SEM).
(D) 3D plot showing results from EPM, SPT and TST for individual CTRL (green) and CMS (blue) mice.
(E) CTRL mice positive for zero (brown), one (purple), two (jade) or three (orange) behavioral criteria. An animal was considered positive if it scored below the corresponding cutoff value (dashed line; data represent means ± SEM).
(F) CMS mice positive for zero (brown), one (purple), two (jade) or three (orange) behavioral criteria. An animal was considered positive if it scored below the corresponding cutoff value (dashed line; data represent means ± SEM).
(G) Comparison of total population of CTRL (green) and CMS (blue) mice positive for zero, one, two or three criteria (D-score of zero to three, respectively).
(H) Percentage of the total population of CTRL (top) and CMS (bottom) mice positive for zero, one, two, or three criteria (D-score of zero to three, respectively).

Additional evidence to support our classification of mice into different subgroups is based on the robustness of behavioral phenotypes. First, the intensity of behavioral phenotypes was proportional to the number of criteria met (Figures 1E and 1F). Second, when re-testing mice on the same behavioral assays (EPM, SPT, TST) under the same experimental conditions two weeks after they performed the test for the first time, we observed a linear correlation between the first and second test in all three behavioral assays suggesting that animals exhibit persistent behavioral phenotypes that do not change over time (Figures S1E-S1G). Third, we performed bootstrapping on our experimental data shown in Figures 1A-1C to demonstrate the consistency of our cutoff values and the distribution of the D-score subgroups (Figure S2).

Together, these results suggest that rodents, like humans, show clear behavioral differences in their response to chronic stress, and that screening mice for individual behavioral phenotypes could facilitate the analysis of neural correlates underlying depression-related behaviors.

Anatomical and physiological correlates of a distinctive chronic stress-induced behavioral phenotype

Ventral tegmental area (VTA) and dorsal raphe nucleus (DR), which contain large populations of dopamine (DA) and serotoninergic neurons, respectively, represent two major downstream projection targets of LHb (Bernard and Veh, 2012). VTA-projecting LHb (LHb→VTA) neurons exhibit hyperactivity in a learned helplessness model of depression (Li et al., 2011), but whether LHb→VTA hyperactivity is associated with a specific chronic stress-induced behavioral phenotype and whether DR-projecting LHb neurons (LHb→DR) also undergo pathological adaptations is unknown. Consistent with previous anatomical studies in rats (Bernard and Veh, 2012), we found that LHb projections to the VTA and DR are organized as independent parallel projections (**Figures S3A-S3C)** that originate from largely separate LHb subnuclei (**Figures S3D-S3G**). Despite this anatomical separation, LHb→VTA and LHb→DR subpopulations may subserve similar functional roles, as optogenetic stimulation of LHb terminals in either VTA (**Figures S3H-S3K**; Lammel et al., 2012; Stamatakis and Stuber, 2012) or DR (**Figures S3L-S3O**) induced robust real-time place aversion.

Next, we performed whole-cell patch clamp recordings from retrogradely labeled LHb→VTA (**Figures 2A and 2B)** and LHb→DR (**Figures 2H and 2I)** neurons in acute slices from CMS and non-stressed CTRL mice that were behaviorally screened based on our D-score classification approach (**Figure 1**). Animals from each group were divided into two categories based on their

individual D-scores: CTRL and CMS mice with a D-score of zero or one ($CTRL_{D0-1}$ and CMS_{D0-1}, respectively) and CTRL and CMS mice with a D-score of two or three ($CTRL_{D2-3}$ and CMS_{D2-3}, respectively). We found that under resting conditions, both LHb→VTA and LHb→DR neurons remained mostly silent and did not fire spontaneous action potentials. However, following the injection of depolarizing ramp currents, we observed remarkable differences in the firing rates of LHb→VTA neurons from animals with different D-scores. LHb→VTA neurons in CMS_{D2-3} mice showed very high firing rates in response to +150 pA current injection that were significantly higher when compared to $CTRL_{D0-1}$ or CMS_{D0-1} mice. Surprisingly, the evoked firing rate of LHb→VTA neurons from $CTRL_{D2-3}$ mice was only marginally lower when compared to CMS_{D2-3} mice, though not statistically different from $CTRL_{D0-1}$ mice (**Figures 2C, 2D and S3P**).

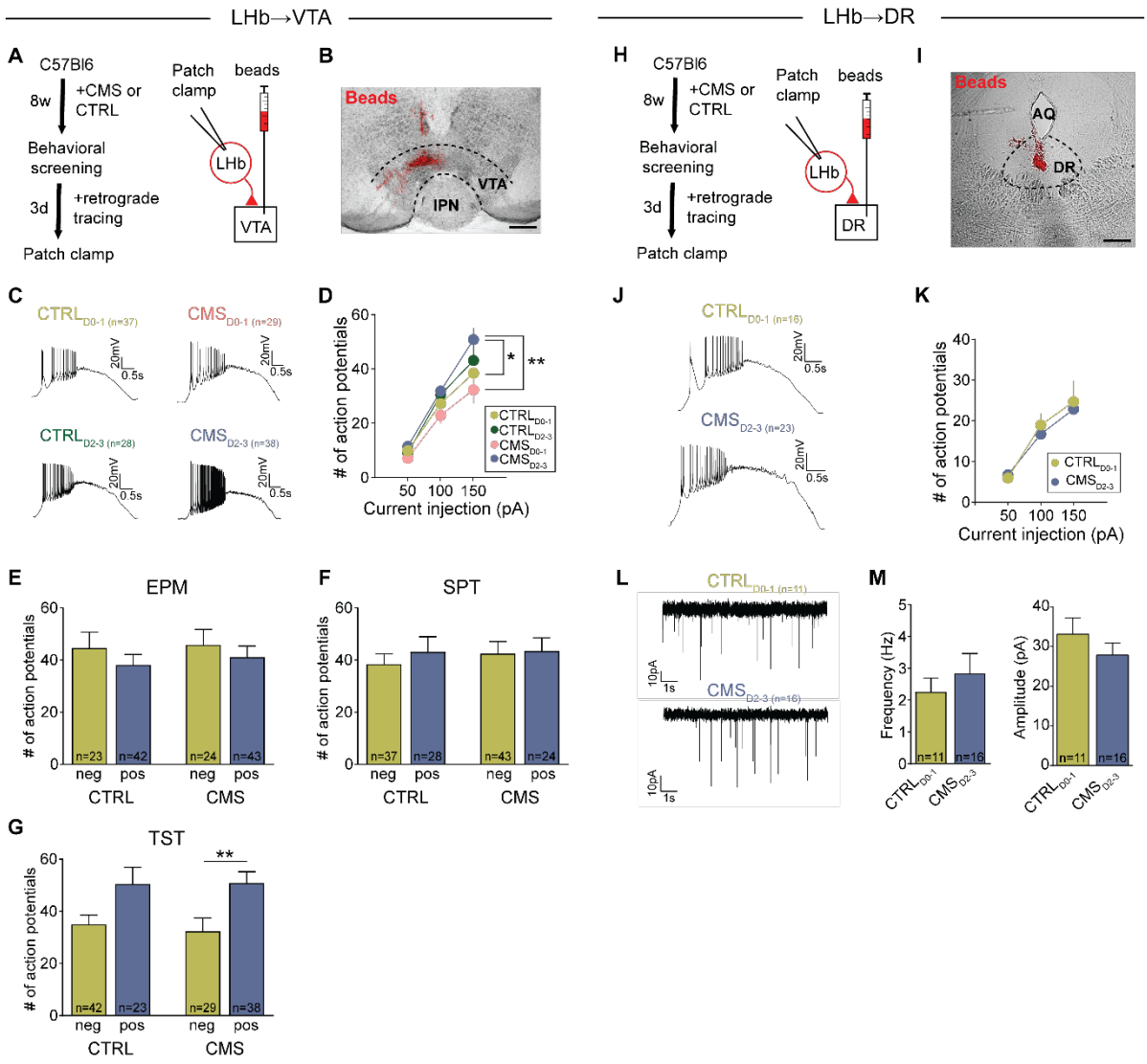

Figure 2. Hyperactivity of LHb neurons is associated with projection target and behavioral phenotype

(A) Experimental design.

(B) Injection site of beads (red) in the VTA (IPN: interpeduncular nucleus; Scale bar: 300 µm).

(C) Firing in response to +150 pA depolarizing current injection in LHb→VTA neurons from CTRL and CMS mice with different D-scores: $CTRL_{D0\text{-}1}$ (top left), $CMS_{D0\text{-}1}$ (top right), $CTRL_{D2\text{-}3}$ (bottom left) and $CMS_{D2\text{-}3}$ (bottom right) mice (Scale bars: 20 mV/0.5 s).
(D) Mean number of action potentials in response to injection of different depolarizing ramp currents recorded in LHb→VTA neurons from $CTRL_{D0\text{-}1}$ (light green), $CTRL_{D2\text{-}3}$ (dark green), $CMS_{D0\text{-}1}$ (pink) and $CMS_{D2\text{-}3}$ (blue) mice (* $p < 0.05$, ** $p < 0.01$, data represent means ± SEM).
(E-G) Mean number of action potentials in response to injection of a +150 pA depolarizing current in LHb→VTA neurons from CTRL or CMS mice that were pooled according to whether they were positive or negative for specific behavioral phenotypes (i.e. anxiety assessed in EPM (E), anhedonia assessed in SPT (F), immobility assessed in TST (G)). Animals were considered positive if they scored below the corresponding cutoff value defined in **Figures 1A-1C** (* $p < 0.05$, ** $p < 0.01$; data represent means ± SEM).
(H) Experimental design.
(I) Injection site of beads (red) in the DR (AQ: cerebral aqueduct; Scale bar: 400 μm).
(J) Firing in response to +150 pA depolarizing current injection in LHb→DR neurons from CTRL and CMS mice with different D-scores: $CTRL_{D0\text{-}1}$ (top) and $CMS_{D2\text{-}3}$ (bottom) mice (Scale bars: 20 mV/0.5 s).
(K) Mean number of action potentials in response to injection of different depolarizing ramp currents recorded in LHb→DR neurons from $CTRL_{D0\text{-}1}$ (light green) and $CMS_{D2\text{-}3}$ (blue) mice (data represent means ± SEM).
(L) mEPSCs recorded in LHb→DR neurons from $CTRL_{D0\text{-}1}$ (top) and $CMS_{D2\text{-}3}$ (bottom) mice (Scale bars: 10 pA/1 s).
(M) Mean mEPSC frequencies (left) and mEPSC amplitudes (right) recorded in LHb→DR neurons from $CTRL_{D0\text{-}1}$ and $CMS_{D2\text{-}3}$ mice (data represent means ± SEM).

When we separated the animals into subgroups based on whether they met individual behavioral criteria, we found that both in CTRL and CMS groups, mice with increased immobility in the TST, but not with anhedonia or anxiety, displayed increased firing (**Figures 2E-2G**). Strikingly, evoked firing of LHb→DR neurons was not significantly different between $CMS_{D2\text{-}3}$ and $CTRL_{D0\text{-}1}$ mice (**Figures 2J and 2K**). Furthermore, we examined excitatory transmission onto LHb→DR neurons, which is known to be altered in LHb→VTA neurons in a learned helplessness model of depression (Li et al., 2011). However, frequency and amplitude of miniature excitatory postsynaptic currents (mEPSCs) recorded from LHb→DR neurons did not significantly differ between $CMS_{D2\text{-}3}$ and $CTRL_{D0\text{-}1}$ mice (**Figures 2L and 2M**). Other electrophysiological parameters, such as membrane resistance and conductance, did not differ significantly between LHb→VTA and LHb→DR neurons (**Figure S3Q**) or LHb→VTA neurons in $CTRL_{D0\text{-}1}$ and $CMS_{D2\text{-}3}$ mice (**Figures S3R**).

To further investigate neural activity patterns in response to CMS, we performed *in vivo* tetrode recordings from LHb→VTA neurons in freely behaving mice (**Figure 3A**). Specifically, we tagged LHb→VTA neurons with channelrhodopsin-2 (ChR2) by injecting a retrogradely transported virus expressing Cre-recombinase (pseudotyped equine infectious anemia virus; RG-EIAV-Cre) into the VTA and a Cre-dependent adeno-associated virus (AAV) expressing ChR2-eYFP (AAV-DIO-ChR2-eYFP) into the LHb of C57BL/6 mice. In the same animals, a driveable optoelectrode (optrode) was implanted above the LHb and lowered in steps throughout the LHb during the recording sessions. $CTRL_{D0\text{-}1}$ and $CMS_{D2\text{-}3}$ mice were identified using our D-score classification approach. Importantly, all $CMS_{D2\text{-}3}$ mice had increased immobility in the TST (i.e. time spent struggling < 93.5 s), but none of the $CTRL_{D0\text{-}1}$ mice had this phenotype. RG-EIAV-Cre-mediated ChR2-eYFP expression and optrode placement in the LHb was confirmed using histological methods (**Figure 3B**). To identify LHb neurons that expressed ChR2 (i.e. LHb→VTA

neurons), we tested whether recorded LHb cells responded with minimal latency to 473 nm light stimulation (**Figures S4A-S4F**). Consistent with direct excitation, all optogenetically identified LHb neurons responded with short (4.79 ± 0.25 ms, n = 12 cells) latency after the light onset. Comparison of spontaneous and light-evoked spikes revealed that stimulation did not induce detectable changes in the action potential shape (**Figures S4D)**. After ChR2-tagged LHb→VTA neurons were identified, their spontaneous activity was recorded over a five-minute period while the mice were freely behaving in their home cages. The average action potential waveform of the LHb→VTA neurons was similar in $CTRL_{D0\text{-}1}$ and $CMS_{D2\text{-}3}$ mice with no significant differences in spike width (**Figure 3C**). Notably, LHb→VTA neurons from $CMS_{D2\text{-}3}$ mice showed an overall increase in both burst activity and tonic firing compared to LHb→VTA neurons from $CTRL_{D0\text{-}1}$ mice (**Figures 3D-3I and S3G**). As a result, the mean firing frequency was also significantly higher in $CMS_{D2\text{-}3}$ than in $CTRL_{D0\text{-}1}$ mice **(Figure 3J**). We also analyzed non-light responsive LHb cells that were concurrently recorded at the same depth and during the same session as the optogenetically-tagged LHb neurons, and found that tonic firing and burst activity of untagged LHb neurons was very similar between $CMS_{D2\text{-}3}$ and $CTRL_{D0\text{-}1}$ mice (**Figures S4H-S4M**). Taken together, LHb hyperactivity consists of both increased tonic and burst activity and is substantially defined by topographic organization, axonal projections and behavioral phenotype.

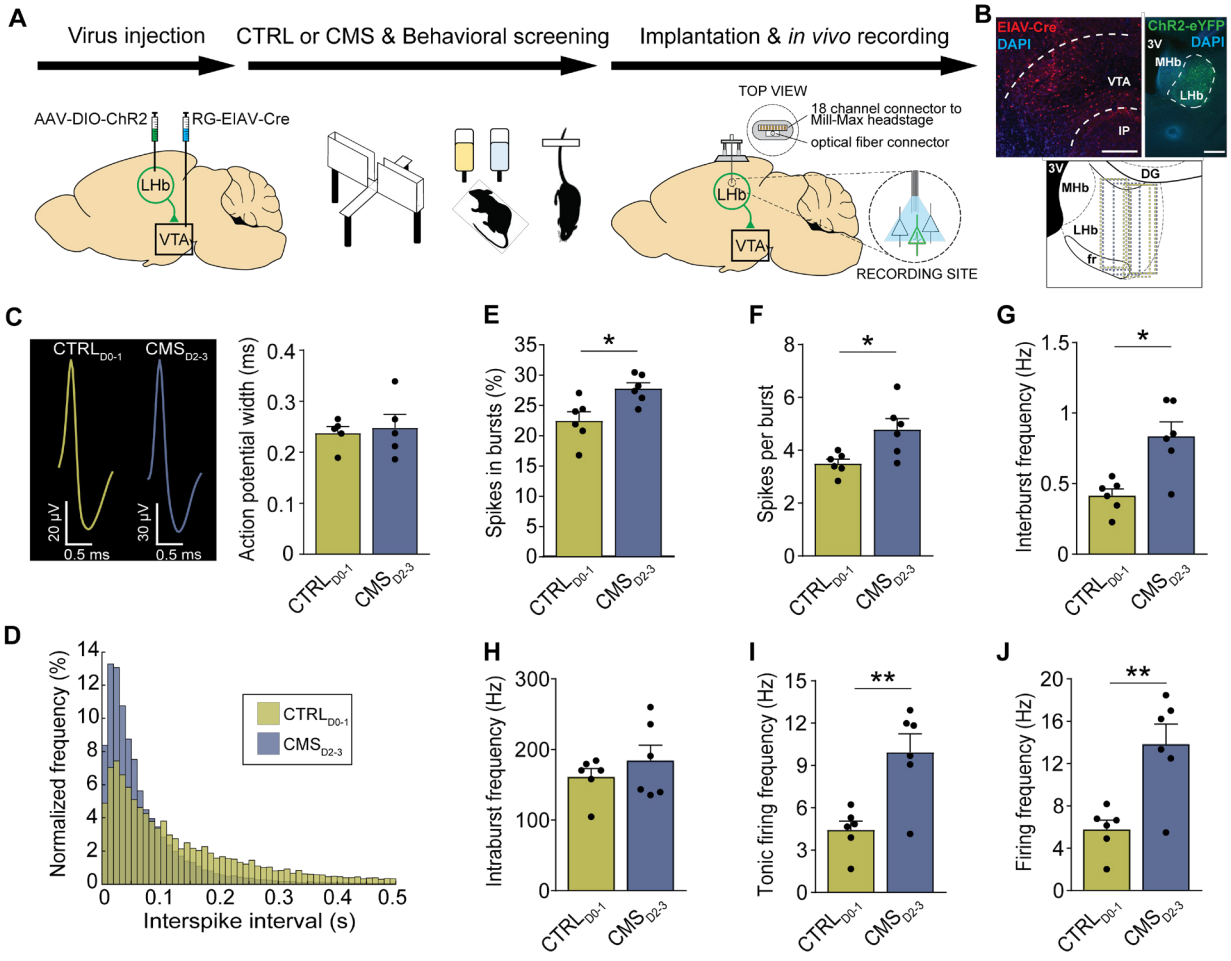

Figure 3. Chronic stress increases burst and tonic firing of LHb→VTA neurons
(A) Experimental design.

(B) Top: Injection-site of EIAV-Cre (red) in the VTA (left) and expression of ChR2-eYFP (green) in LHb→VTA neurons (right) (IP: interpeduncular nucleus, 3V: 3rd ventricle, MHb: medial habenula; DAPI: blue; Scale bars: 300 µm (left), 250 µm (right)). Bottom: Localizations of optrodes in LHb for $CTRL_{D0-1}$ (green) and CMS_{D2-3} (blue) mice (fr: fasciculus retroflexus, DG: dentate gyrus).
(C) Left: Action potential waveforms for LHb→VTA neurons in $CTRL_{D0-1}$ (green) and CMS_{D2-3} (blue) mice (Scale bars: 20 µV/0.5 ms ($CTRL_{D0-1}$), 30 µV/0.5 ms (CMS_{D2-3})). Right: Mean action potential width for LHb→VTA neurons in $CTRL_{D0-1}$ (green) and CMS_{D2-3} (blue) mice (data represent means ± SEM).
(D) Normalized frequencies of interspike intervals for LHb→VTA neurons in $CTRL_{D0-1}$ (green) and CMS_{D2-3} (blue) mice.
(E) Mean percentage of spikes in bursts recorded for LHb→VTA neurons in $CTRL_{D0-1}$ (green) and CMS_{D2-3} (blue) mice (* $p < 0.05$, data represent means ± SEM).
(F) Mean number of spikes per burst for LHb→VTA neurons in $CTRL_{D0-1}$ (green) and CMS_{D2-3} (blue) mice (* $p < 0.05$, data represent means ± SEM).
(G) Mean interburst frequencies for LHb→VTA neurons in $CTRL_{D0-1}$ (green) and CMS_{D2-3} (blue) mice (* $p < 0.05$, data represent means ± SEM).
(H) Mean intraburst frequencies for LHb→VTA neurons in $CTRL_{D0-1}$ (green) and CMS_{D2-3} (blue) mice (data represent means ± SEM).
(I) Mean tonic firing frequencies for LHb→VTA neurons in $CTRL_{D0-1}$ (green) and CMS_{D2-3} (blue) mice (** $p < 0.01$, data represent means ± SEM).
(J) Mean firing frequencies for LHb→VTA neurons in $CTRL_{D0-1}$ (green) and CMS_{D2-3} (blue) mice (** $p < 0.01$, data represent means ± SEM).

Distinct inputs onto LHb neurons based on their projections

We hypothesized that differences in the architecture of afferent inputs to projection-defined LHb neurons contribute to their selective CMS-induced hyperactivity phenotype. Classical anatomical tracing studies have shown that major inputs to the LHb arise from various brain regions including the entopeduncular nucleus (EP), lateral preoptic area (LPO), lateral hypothalamus (LH), DR and VTA (Herkenham and Nauta, 1977), but the connectivity of upstream brain structures with projection-defined LHb subpopulations has not yet been investigated. In order to map whole-brain monosynaptic inputs onto LHb→VTA and LHb→DR neurons, we used a rabies virus-based tracing strategy (Osakada and Callaway, 2013). We injected a retrogradely transported canine adenovirus expressing Cre-recombinase (CAV2-Cre) into either the VTA or DR of C57BL/6 mice. In addition, we injected two Cre-dependent AAVs, one expressing the avian tumor virus A receptor (AAV-DIO-TVA-mCherry) and the other expressing the rabies virus glycoprotein (AAV-DIO-RG) into the LHb. Four weeks later, we injected a modified rabies virus expressing GFP (Rabies-EnvA-ΔG-GFP) into the LHb (**Figure 4A**). Histological analysis revealed the specificity of the CAV2-Cre injection-sites in the VTA or DR (**Figure S5A**) and the localization of starter cells (i.e. cells that are both TVA-mCherry- and RV-GFP-immunopositive) in the LHb (**Figures 4B, S5B and S5C**). We then determined the anatomical locations as well as the number of GFP-expressing cells that synapse onto LHb→VTA and LHb→DR neurons (**Figure 4C**). We found that LHb→VTA and LHb→DR neurons receive qualitatively similar inputs, with dominant projections from the LH, VTA, pallidum, LPO and EP. Quantitatively, however, we found that the EP provides a significantly greater share of input to LHb→VTA neurons, while LH and VTA provide significantly more inputs to LHb→DR neurons (**Figure 4D**). Collectively, the EP sends substantially stronger inputs to LHb→VTA compared to LHb→DR and we speculate that chronic

stress-induced synaptic adaptations in specific excitatory inputs (e.g. EP) to LHb→VTA neurons may promote their hyperactivity in depression-related states.

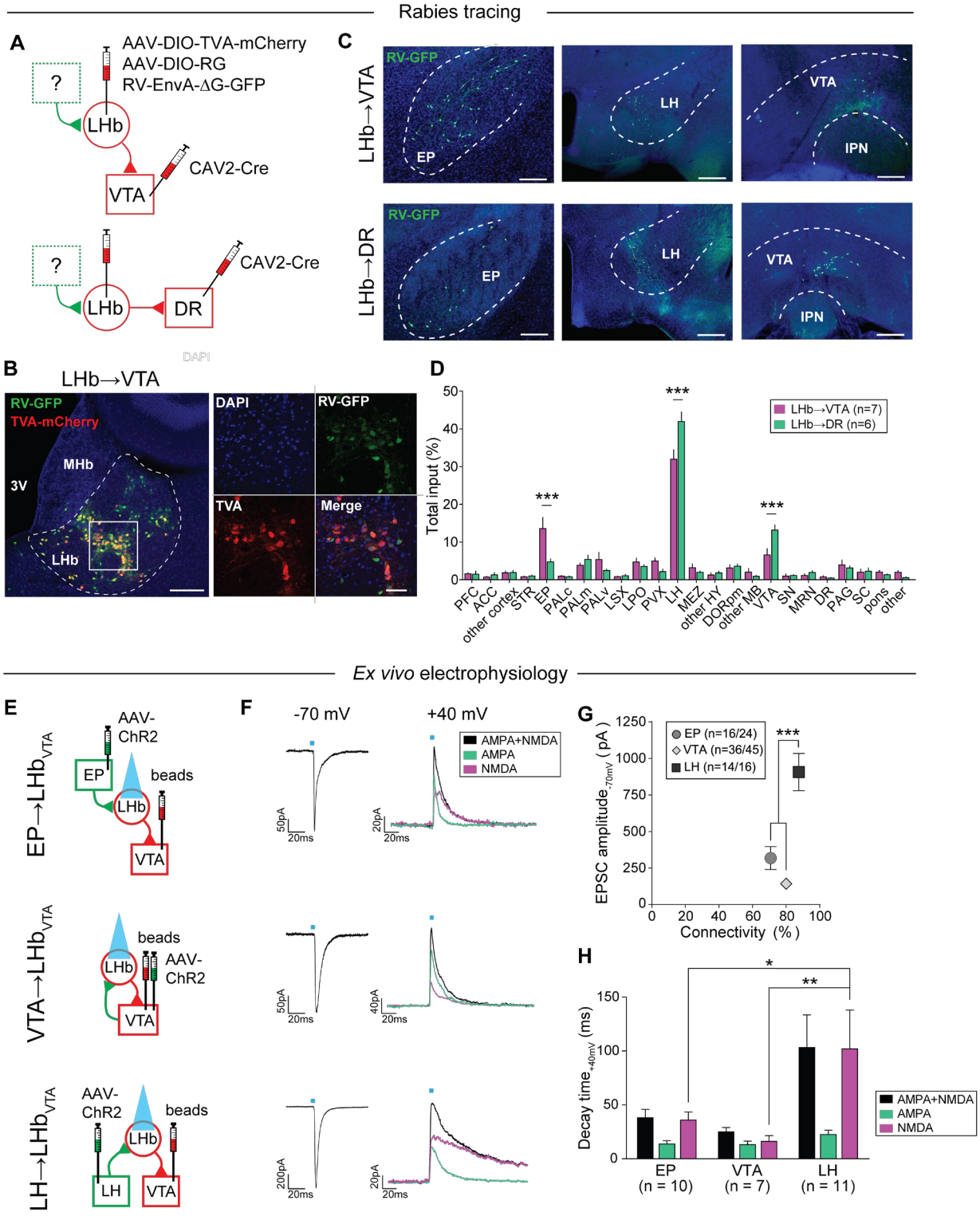

Figure 4. Anatomical and functional mapping of inputs to LHb subpopulations
(A) Experimental design.
(B) Left: Anatomical distribution of starter cells in the LHb for mapping inputs to LHb→VTA neurons. Starter cells: cells that co-express RV-GFP (green) and TVA-mCherry (red; Scale bar: 150 μm). Right: Higher magnification image (DAPI: blue; Scale bar: 60 μm).
(C) Anatomical distribution of input neurons (i.e. RV-GFP-positive cells) to LHb→VTA (top) and LHb→DR (bottom) neurons in the entopeduncular nucleus (EP, left), lateral hypothalamus (LH, middle) and VTA (right; Scale bars: 200 μm (left, right), 400 μm (middle)).
(D) Quantification of inputs to LHb→VTA (purple) and LHb→DR (green) neurons (percentage of total input counted in each individual brain). See **Figure S4** legend for abbreviations (*** $p < 0.001$, data represent means ± SEM).
(E) Experimental design.
(F) Left: EPSCs for light stimulation of EP (top; Scale bar: 50 pA/20 ms), VTA (middle; Scale bar: 50 pA/20 ms) or LH (bottom; Scale bar: 200 pA/20 ms) inputs to LHb→VTA neurons. Right: EPSCs showing dual AMPAR+NMDAR- (black), AMPAR- (jade; in 50 μM AP5) and NMDAR (purple; after digital subtraction)-mediated currents (purple) for light stimulation of EP (top; Scale bar: 20 pA/20 ms), VTA (middle; Scale bar: 40 pA/20 ms) or LH (bottom; Scale bar: 20 pA/20 ms) inputs to LHb→VTA neurons.
(G) Mean EPSC peak amplitudes and connectivity for EP, VTA and LH inputs to LHb→VTA neurons (*** $p < 0.001$, data represent means ± SEM).
(H) Mean decay time for dual AMPAR+NMDAR (black), AMPAR (jade) and NMDAR (purple) components for EP, VTA or LH inputs to LHb→VTA neurons (* $p < 0.05$, ** $p < 0.01$, data represent means ± SEM).

Aberrant pre- and postsynaptic plasticity in the LHb

To further examine the synaptic properties of identified excitatory inputs to LHb→VTA neurons, we injected an AAV expressing ChR2 under the control of the CaMKII promoter into the EP, VTA or LH and retrobeads into the VTA of C57BL/6 mice. We focused on EP, VTA and LH inputs because our whole brain mapping experiments revealed that these are the major inputs to LHb→VTA neurons (**Figure 4D**). We then performed whole-cell patch clamp recordings in acute brain slices from retrogradely labeled LHb neurons and recorded light-evoked excitatory postsynaptic currents (EPSCs; in 50 μM picrotoxin) by stimulating ChR2-expressing EP, VTA or LH terminals with blue light (**Figure 4E**). Our data revealed that even under control conditions the synaptic properties of individual excitatory inputs onto LHb→VTA neurons are remarkably different. Though the functional connectivity of the three inputs to LHb→VTA neurons is similar, the mean amplitude of light evoked EPSCs (at -70 mV) from the LH was significantly greater compared to the EP and VTA (**Figures 4F and 4G**), which is remarkably consistent with the relative input strength seen in our rabies tracing experiments (**Figure 4D**). Moreover, NMDA receptor (NMDAR)-mediated currents (recorded at +40 mV) evoked by stimulation of LH inputs exhibited significantly greater decay time compared to VTA and EP inputs, suggesting possible differences in the composition of NMDARs between individual inputs (**Figures 4F and 4H**).

Next, we compared the synaptic properties of excitatory EP, VTA and LH inputs onto LHb→VTA neurons from $CTRL_{D0\text{-}1}$ and $CMS_{D2\text{-}3}$ mice. While the AMPAR/NMDAR ratio was not significantly altered for any input when comparing $CTRL_{D0\text{-}1}$ with $CMS_{D2\text{-}3}$ mice (data not shown), we observed notable differences in the presynaptic release probability (PRP). The PRP of excitatory EP synapses was higher in $CMS_{D2\text{-}3}$ compared to $CTRL_{D0\text{-}1}$ mice (i.e. decreased paired

pulse ratio (PPR)), whereas it was the opposite for VTA inputs (increased PPR), and no significant differences were observed for LH inputs (**Figure 5A**).

Postsynaptically, AMPAR subunit composition can influence cell excitability and synaptic efficacy (Liu and Zukin, 2007). In contrast to GluR2-containing ones, GluR2-lacking AMPARs are calcium-permeable and exhibit higher single-channel conductance (Hollmann et al., 1991). We found that EP, VTA and LH inputs exhibit a characteristic inwardly rectifying AMPAR-mediated currents at +40 mV. However, only in EP inputs onto LHb→VTA neurons was the rectification index of AMPAR-mediated currents significantly increased in $CMS_{D2\text{-}3}$ compared to $CTRL_{D0\text{-}1}$ mice, suggesting an increase in surface expression of GluR2-lacking AMPARs (**Figure 5B**). To confirm an increase in GluR2-lacking AMPARs at the EP synapses, we applied 30 μM 1-naphthyl acetyl spermine (NASPM, a selective blocker of GluR2-lacking AMPARs) to brain slices prepared from $CMS_{D2\text{-}3}$ and $CTRL_{D0\text{-}1}$ mice. As expected, this reduced the amplitude of light-evoked AMPAR-mediated currents in both $CMS_{D2\text{-}3}$ and $CTRL_{D0\text{-}1}$ mice, indicating an already rectifying nature of AMPARs at the EP synapse. Importantly, the amplitude of the light-evoked AMPAR-mediated current was significantly more reduced in $CMS_{D2\text{-}3}$ compared to $CTRL_{D0\text{-}1}$ mice, suggesting an even stronger expression of GluR2-lacking AMPARs in response to CMS (**Figure 5C**). Taken together, CMS exposure predominantly affects the synaptic properties of EP synapses onto LHb→VTA neurons, which includes both increased PRP as well as increased surface expression of GluR2-lacking AMPARs.

Divergent synaptic connectivity of EP inputs with LHb subpopulations

To further examine the synaptic connectivity of EP inputs with projection-defined LHb subpopulations, we performed an additional series of experiments. First, we found that the majority of EP terminals are located in close proximity to LHb→VTA neurons, whereas there seems to be a clear anatomical separation between EP terminals and LHb→DR cells, which are mainly located in the medial LHb (**Figures 5D and S3D-S3G**). Second, we found that the majority of light-evoked EPSCs from excitatory EP inputs to LHb→DR neurons exhibit a delayed onset, and the peak response latency is significantly greater in LHb→DR neurons compared to LHb→VTA neurons (**Figures 5E and 5F**) suggesting that excitatory EP neurons may not directly target LHb→DR neurons. Third, to further test whether the EP→LHb→DR connection is indeed polysynaptic, we used a previously described technique (Cho et al., 2013; Petreanu et al., 2009) to depolarize ChR2-positive presynaptic terminals directly by blocking sodium channels using tetrodotoxin (TTX, 1 μM) and potassium channels using 4-aminopyridine (4-AP, 50 μM). As expected, bath application of TTX blocked light-evoked EPSCs in both LHb subpopulations. Subsequent application of 4-AP, however, rescued TTX-blocked EPSCs only in LHb→VTA neurons, which indicated the monosynaptic origin of these EPSCs. 4-AP did not rescue TTX-blocked polysynaptic EPSCs in LHb→DR neurons as these EPSCs would require action potential firing in local LHb neurons (**Figure 5G**). These results suggest that excitatory EP inputs make monosynaptic inputs onto LHb→VTA neurons, but their excitation of LHb→DR neurons primarily involves a feedforward excitation of local LHb neurons.

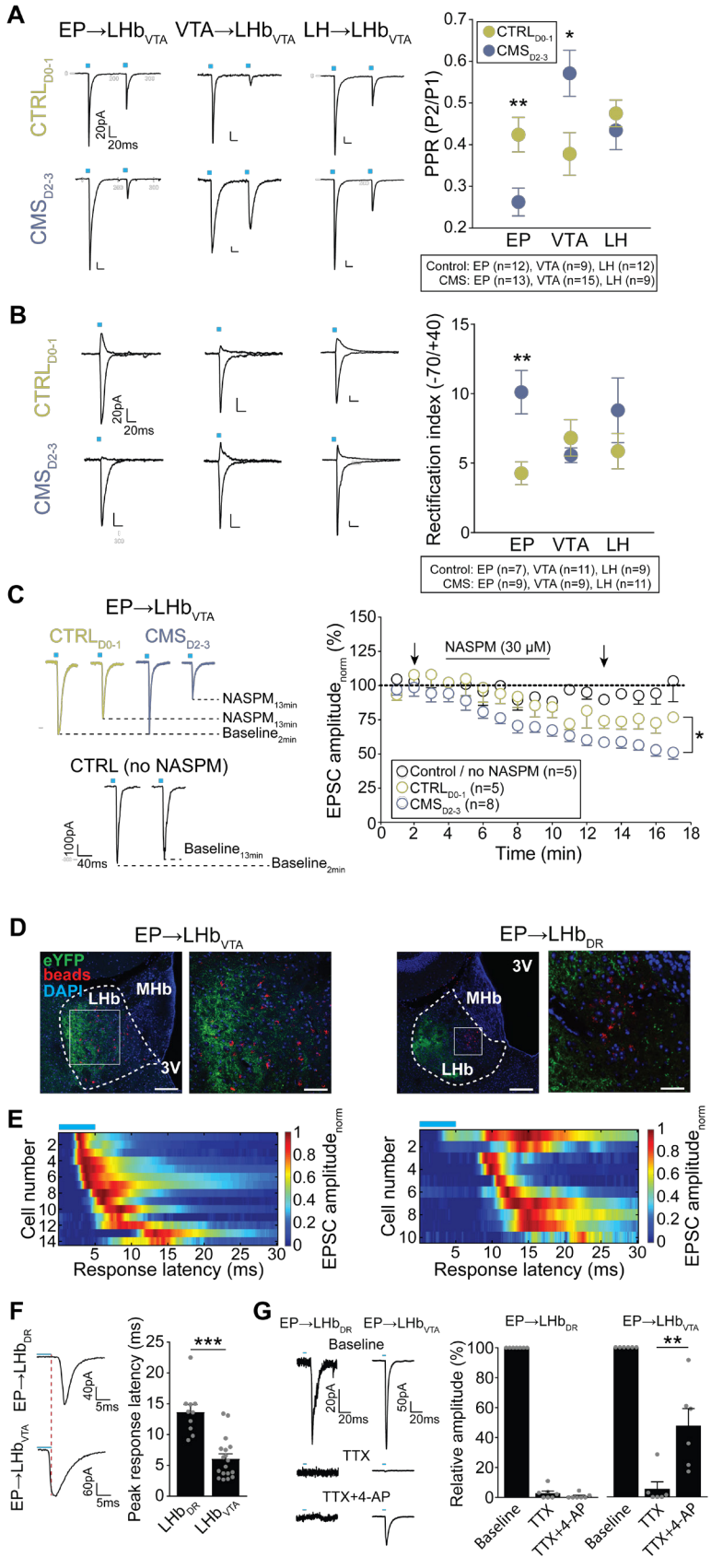

Figure 5. Chronic stress induces synaptic adaptations in excitatory EP inputs to LHb→VTA neurons

(A) Left: Paired pulse EPSCs (100 ms interval; -70 mV) in response to light stimulation of EP (left), VTA (middle) or LH (right) inputs to LHb→VTA neurons in $CTRL_{D0-1}$ (top) and CMS_{D2-3} (bottom) mice (Scale bars: 20 pA/20 ms). Right: Mean paired pulse ratios (PPR, calculated as peak2/peak1) for EP, VTA and LH inputs to LHb→VTA neurons in $CTRL_{D0-1}$ (green) and CMS_{D2-3} (blue) mice (* $p < 0.05$, ** $p < 0.01$, data represent means ± SEM).

(B) Left: AMPAR-mediated currents at +40 mV and -70 mV (in 50 µM AP5) for EP (left), VTA (middle) or LH (right) inputs to LHb→VTA neurons from $CTRL_{D0-1}$ (top) and CMS_{D2-3} (bottom) mice (Scale bars: 20 pA/20 ms). Right: Mean rectification index (peak amplitude$_{-70mV}$/peak amplitude$_{+40mV}$) for EP, VTA and LH inputs to LHb→VTA neurons from $CTRL_{D0-1}$ (green) and CMS_{D2-3} (blue) mice (** $p < 0.01$, data represent means ± SEM).

(C) Left: EPSCs (-70 mV) for stimulation of EP inputs to LHb→VTA neurons during baseline and after wash-in of 30 µM NASPM in $CTRL_{D0-1}$ (green) and CMS_{D2-3} (blue) mice. The amplitude of baseline EPSCs does not change over time when NASPM was not applied (black; Scale bar: 100 pA / 40 ms). Right: Normalized mean AMPAR-mediated EPSC amplitudes with and without bath application of NASPM for the three experimental groups. Arrows indicate sample traces shown on the left (* $p < 0.05$, data represent means ± SEM).

(D) Left: EP terminals (eYFP, green) in lateral LHb adjacent to

retrogradely labeled (beads, red) LHb→VTA neurons (DAPI: blue; Scale bars: 160 μm (left), 80 μm (right)). Right: EP terminals (eYFP, green) in lateral LHb and retrogradely labeled (beads, red) LHb→DR neurons in medial LHb. Squares indicate higher magnification images (Scale bars: 160 μm (left), 40 μm (right)).
(E) Heat map representing peak response latencies of LHb→VTA (left) and LHb→DR (right) neurons in response to light stimulation of excitatory EP terminals in the LHb. Each row represents individual cells. Color code represents normalized EPSC amplitude.
(F) Left: EPSCs from LHb→DR (top) or LHb→VTA (bottom) neurons in response to light stimulation of EP terminals in the LHb (Scale bars: 40 pA/5ms (top), 60 pA/5ms (bottom)). Right: Mean peak response latencies for light stimulation of excitatory EP inputs to LHb→DR or LHb→VTA neurons (*** $p < 0.001$, mean ± SEM).
(G) Left: EPSCs from LHb→DR (left) or LHb→VTA (right) neurons in response to light stimulation of EP terminals at baseline (top), after bath application of TTX (middle) and TTX + 4-AP (bottom; Scale bars: 20 pA/20 ms (left), 50 pA/20 ms (right)). Right: Relative amplitudes of EPSCs recorded from LHb→DR and LHb→VTA neurons in response to light stimulation of EP terminals in the LHb at baseline and after wash-in of TTX or TTX + 4-AP (** $p < 0.01$, data represent means ± SEM).

In vivo modulation of LHb circuitry selectively alters passive coping and effort-related motivated behavior

Because hyperactivity of the LHb→VTA pathway was specifically associated with increased immobility in the TST, but not anxiety or anhedonia (**Figures 2E-2G)**, we hypothesized that *in vivo* manipulations of the LHb involving downstream VTA or upstream EP projections will selectively affect transitions from active struggling to PC behavior and that this transition can become maladaptive in response to CMS exposure. Our hypothesis is supported by a recent study which reported that optogenetic stimulation of the LHb→RMTg pathway selectively increases immobility in the FST (Proulx et al., 2018), though it is likely that FST and TST are not fully represented by the same neurocircuitry. To test this, we performed a series of behavioral experiments that involve targeting of chemogenetic or optogenetic constructs to projection-defined LHb and EP neurons. First, consistent with our hypothesis, we found that optogenetic stimulation (10 Hz, 5 ms pulses) of ChR2-expressing LHb→VTA neurons in non-stressed wildtype (C57BL/6) mice was sufficient to increase immobility in the TST; this was indicated by a significant decrease in the time mice spent struggling when compared to mice that expressed eYFP in LHb→VTA neurons. In contrast, anxiety, anhedonia and locomotor activity were not significantly altered in response to optogenetic activation of LHb→VTA neurons in ChR2 mice compared to eYFP mice (**Figures S6A and S6B**). Second, chemogenetic activation (4 mg/kg CNO) of LHb→VTA neurons in non-stressed wildtype mice confirmed the selective effects on passive immobility in the TST (**Figures 6A and 6B**). Third, we found that chemogenetic silencing of LHb→VTA neurons selectively reduced immobility in the TST in CMS mice, while other behaviors were not affected (**Figures 6C and 6D**). Fourth, chemogenetic activation of EP→LHb neurons selectively increased immobility in the TST in non-stressed wildtype mice (**Figures 6E and 6F**), whereas chemogenetic silencing of EP→LHb neurons in CMS-exposed mice selectively reduced immobility in the TST without affecting other behaviors (**Figures 6G and 6H**). Fifth, chemogenetic activation of LHb→VTA or EP→LHb neurons also increased immobility in the FST in non-stressed wildtype mice (**Figures S6C and S6D**).

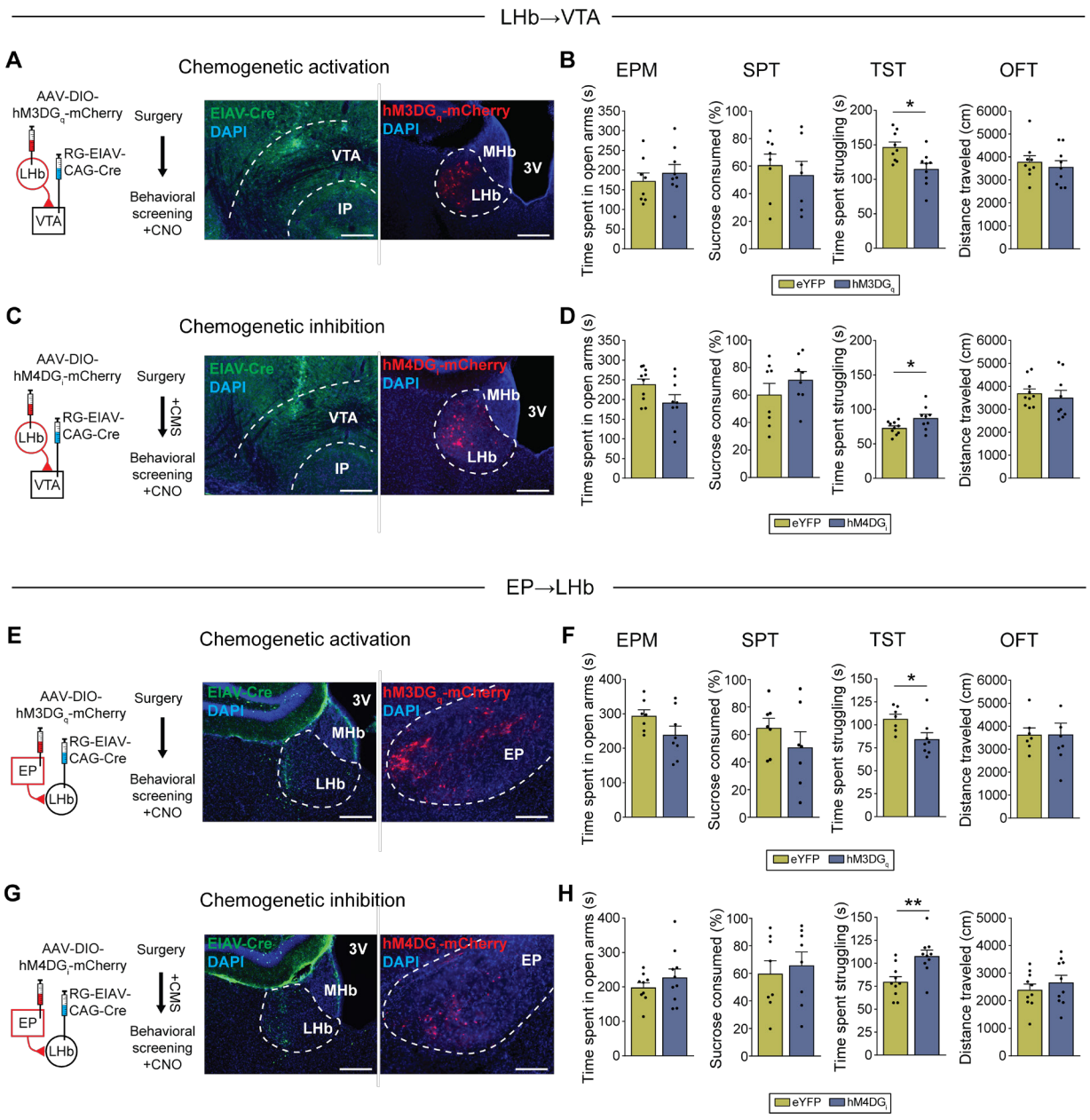

Figure 6. In vivo chemogenetic modulation of LHb circuitry selectively alters passive coping and effort-related motivation

(A) Experimental design (left) and injection-site of EIAV-Cre (green) in VTA (middle) and hM3DGq-mCherry (red) expression in LHb→VTA neurons (right) (DAPI: blue; Scale bars: 300 µm (left), 200 µm (right)).

(B) Time spent in open arms in EPM, sucrose consumption in SPT, time spent struggling in TST and total distance travelled in OFT after CNO injections for non-stressed mice expressing eYFP or hM3DGq-mCherry in LHb→VTA neurons (* $p < 0.05$, data represent means ± SEM).

(C) Experimental design (left) and injection-site of EIAV-Cre (green) in VTA (middle) and hM4DGi-mCherry (red) expression in LHb→VTA neurons (right) (DAPI: blue; Scale bars: left: 300 µm (left), 200 µm (right)).

(D) Time spent in open arms in EPM, sucrose consumption in SPT, time spent struggling in TST and total distance travelled in OFT after CNO injections for CMS mice expressing eYFP or hM4DGi-mCherry in LHb→VTA neurons (* $p < 0.05$, data represent means ± SEM).
(E) Experimental design (left) and injection-site of EIAV-Cre (green) in LHb (middle) and hM3DGq-mCherry (red) expression in EP→LHb neurons (right) (DAPI: blue; Scale bars: 300 µm (left), 200 µm (right)).
(F) Time spent in open arms in EPM, sucrose consumption in SPT, time spent struggling in TST and total distance travelled in OFT after CNO injections for non-stressed mice expressing eYFP or hM3DGq-mCherry in EP→LHb neurons (* $p < 0.05$, data represent means ± SEM).
(G) Experimental design (left) and injection-site of EIAV-Cre (green) in LHb (middle) and hM4DGi-mCherry (red) expression in EP→LHb neurons (right) (DAPI: blue; Scale bars: 300 µm (left), 200 µm (right)).
(H) Time spent in open arms in EPM, sucrose consumption in SPT, time spent struggling in TST and total distance travelled in OFT after CNO injections for CMS mice expressing eYFP or hM4DGi-mCherry in EP→LHb neurons (** $p < 0.01$, data represent means ± SEM).

The reduced ability to experience rewarding feelings and pleasure (anhedonia) and a loss of motivation are both hallmarks of depression (Nestler and Carlezon, 2006), but it is possible that these traits are represented by different neural circuits. To examine whether increased activity in LHb pathways is sufficient to decrease effort-related motivated behaviors, we tested animals in an operant task in which animals have to perform nose pokes under a fixed or progressive ratio schedule in order to receive rewards. Chemogenetic activation of LHb→VTA or EP→LHb neurons did not influence nose poking behavior of animals when the requirements to obtain a reward remained constant (i.e. under a fixed ratio; low level effort required; **Figures S6E and S6G**). In contrast, in the operant task where increasing the number of nose pokes was required to obtain a reward (i.e. progressive ratio), chemogenetic activation of LHb→VTA, significantly reduced nose poking behavior when compared to eYFP animals (**Figure S6F**). Surprisingly, activation of EP→LHb neurons did not influence effort-related motivated behaviors, which raises the possibility that other inputs or a combined activation of inputs may be necessary to elicit a behavioral response (**Figure S6H)**. Taken together, although anxiety and anhedonia are major components of chronic stress-induced behavioral syndrome, they may not be regulated through downstream VTA and upstream EP projections of the LHb, which predominantly appear to be relevant for pathological impairments in motivated behaviors.

Molecular and physiological correlates of passive coping

We then designed a multi-level approach that describes a behavioral phenotype from circuit to physiology to gene-expression profile (**Figure 7A**). Specifically, we collected electrophysiological and RNA expression data from single, projection-defined LHb neurons (**Figure S7A**) and examined their correlation with PC. Importantly, instead of pooling animals based on the number of criteria they met and separating them into CTRL and CMS groups, we pooled all animals based solely on whether they are positive or negative for prolonged immobility in the TST using our cutoff values determined in **Figure 1** (TST+ or TST-, respectively). We argue that this approach will lead to greater precision in detecting meaningful molecular biomarkers that are associated with this specific behavioral phenotype.

As expected, while the number of action potentials in response to depolarizing current injections could not be distinguished between TST- LHb→VTA and LHb→DR cells, TST+ LHb→VTA neurons consistently fired more action potentials compared to the other groups

(**Figures 7B and S7C**). In contrast, no significant difference was observed when we compared evoked firing from animals that were positive or negative in the EPM and SPT assays **(Figures S7B and S7C**). As most projection-defined LHb neurons were silent in our whole-cell recordings, we transiently hyperpolarized the cells, which resulted in action potential firing under resting conditions. We then evaluated the firing modes of cells in the three groups. 62% (n = 26/42 cells) of LHb→VTA neurons in TST- mice were predominantly bursting, whereas this number increased to 77% (n = 41/53 cells) in TST+ LHb→VTA neurons, which was similar high in TST- LHb→DR neurons (85%, n = 11/13 cells; **Figure 7C**). We further corroborated this observation by quantifying the relative and cumulative frequency of inter spike intervals (**Figures 7D and 7E**). In addition, we found that TST+ LHb→VTA cells display a more hyperpolarized resting membrane potential (RMP) compared to TST- LHb→VTA cells. By contrast, the RMP in TST+ LHb→VTA and TST- LHb→DR cells was not significantly different (**Figure 7F**). Consistent with previous studies (Weiss and Veh, 2011; Yang et al., 2018), we found that a more hyperpolarized RMP was associated with increased burst firing (**Figures 7F, 7G, S7D and S7E**).

To evaluate transcriptomic differences between different LHb subpopulations, we analyzed differential gene expression between LHb→VTA and LHb→DR neurons. Among the most significant differences, we found strong enrichment of synaptic glutamate receptors *Grik2* and *Grid2*, and the neuronal excitability-relevant potassium channel Kcnc2 (Kv3.2) in LHb→VTA (n = 16 cells, 5 mice) compared to LHb→DR neurons (n = 14 cells, 5 mice). As biomarkers, collective expression pattern of these genes sufficiently identifies the two cell populations (**Figures 7H and S7F**). We also analyzed differential gene expression between TST- (n = 16 cells, 5 mice) and TST+ (n = 37 cells, 10 mice) in LHb→VTA neurons (**Figures 7I and S7G**). We found significant upregulation of *Kcnc1* in TST+ compared to TST- neurons, making its expression similar to those we found in LHb→DR cells (**Figure 7J**). In addition, we found downregulation of synaptic regulators *Lrrtm3* and glutamate-receptor subunit *Grin1* (**Figures 7I and S7G**). Together, these transcriptomic analyses revealed the identity of select genes that collectively can serve as biomarkers to differentiate LHb→VTA and LHb→DR (*Grid2, Grik2* and *Kcnc2*), as well as TST- and TST+ LHb→VTA neurons (*Lrrtm3, Grin1* and *Kcnc1*). The contrasting nature of *Kcnc1* in differentiating TST- and TST+ LHb→VTA neurons prompted us to examine the full extent of genes that may follow similar patterns. For this, we performed regression analysis on the fold difference of gene expression in LHb→VTA and LHb→DR, and in TST- and TST+ LHb→VTA comparisons (**Figures 7K and S7H**). Surprisingly, we found that the overall gene-expression profile of TST+ LHb→VTA neurons changes towards that in TST- LHb→DR neurons. While its importance remains elusive, this finding underscores a pronounced plasticity of LHb→VTA neurons that is linked to a specific behavioral phenotype. Importantly, differential gene expression analysis made after grouping cells as CTRL (n = 26 cells, 9 mice) versus CMS (n = 27 cells, 6 mice) revealed fewer and more modest differences in LHb→VTA neurons (**Figure S8**), further highlighting the importance of phenotypic (TST- versus TST+) rather than experience-based (CTRL versus CMS) classification.

Together, these outcomes link a specific behavioral phenotype that involves increased PC to specific molecular, cellular and circuit characteristics. Because increased PC behavior may be related to the pathological motivation impairments seen in major depression in humans, our results may serve as a foundation for the development of symptom-specific therapeutic interventions as well as predictive biomarkers, both of which are severely lacking in current medicine.

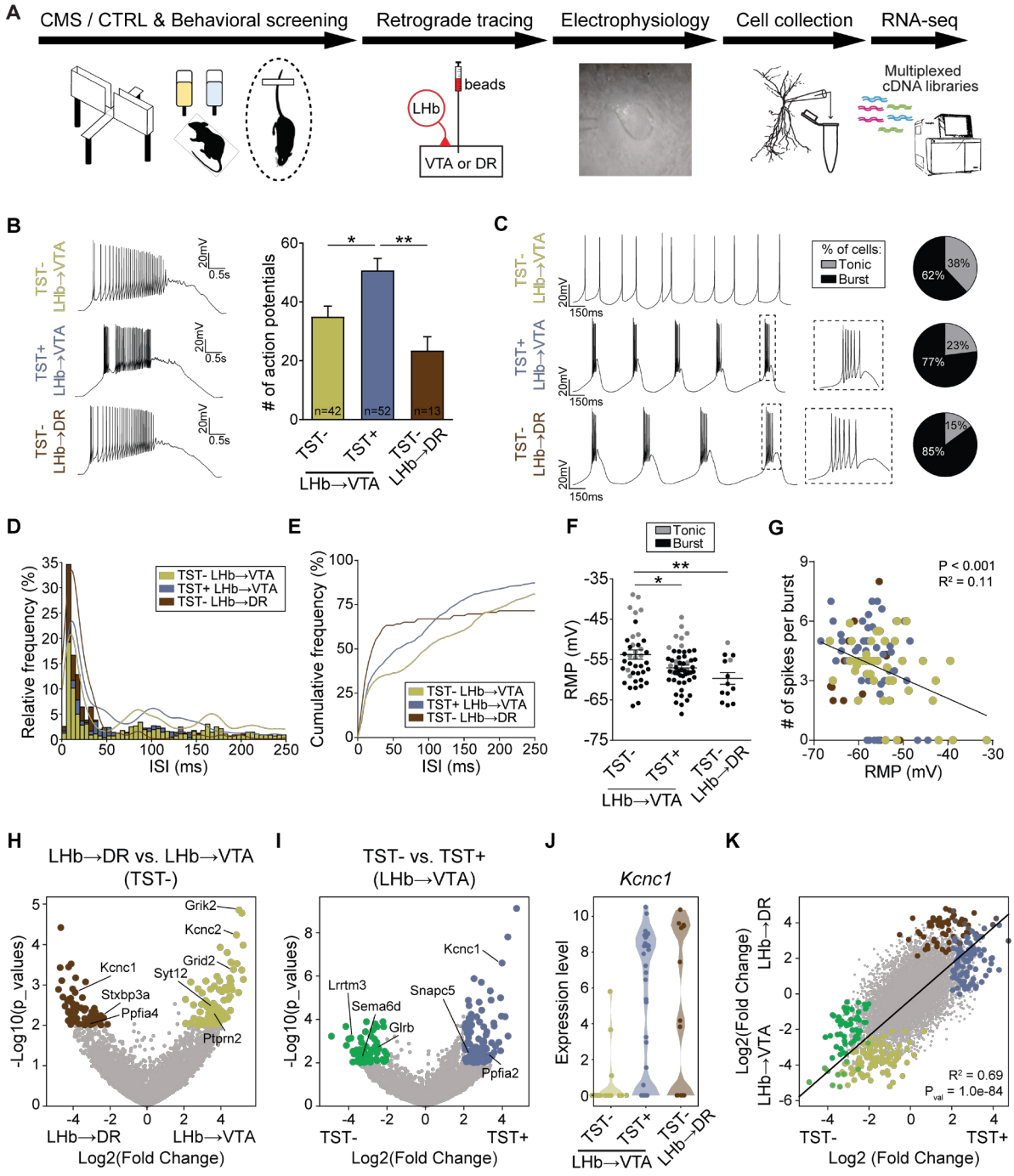

Figure 7. Molecular and physiological correlates of passive coping
(A) Experimental design.
(B) Left: Firing in response to +150 pA depolarizing current injection from LHb→VTA neurons in TST-negative (TST-, top), TST-positive (TST+, middle) mice and LHb→DR neurons (TST-, bottom; Scale bars: 20 mV/0.5 s). Right: Mean number of action potentials in response to +150 pA depolarizing current injection for the three groups (* $p < 0.05$, ** $p < 0.01$, data represent means ± SEM).

(C) Current clamp recordings and pie charts showing an increased number of cells with burst firing in TST+ LHb→VTA and TST- LHb→DR compared to TST- LHb→VTA neurons. Firing was initiated with a brief, transient injection of a hyperpolarizing current (Scale bars: 20 mV/150 ms).
(D) ISI histogram with corresponding Kernel density functions for TST+ LHb→VTA, TST- LHb→VTA and TST- LHb→DR neurons.
(E) Cumulative frequency histogram displaying a shift to shorter ISIs in TST+ LHb→VTA cells compared to TST- LHb→VTA neurons. By contrast, TST- LHb→DR neurons display the shortest ISIs.
(F) Mean resting membrane potentials (RMP) for TST+ LHb→VTA, TST- LHb→VTA and TST- LHb→DR neurons (grey: cells that displayed tonic firing, black: bursting cells; * $p < 0.05$, ** $p < 0.01$, data represent means ± SEM).
(G) Number of spikes per burst is inversely correlated with RMP. Zero spikes per burst represent data from cells that displayed only tonic, but no burst firing.
(H) Volcano plots displaying differential gene expression between single LHb→VTA and LHb→DR neurons in TST- mice. Gold and brown data points denote genes that are significantly enriched in LHb→VTA versus TST- LHb→DR neurons from TST- mice, respectively. Highlighted are the ion channel-coding and synapse-related genes. Gray data points represent genes that are not significantly enriched in either category (i.e. absolute value of Log2(Fold Change) < 2 and $p < 0.01$).
(I) Violin plot displaying differential gene expression between single LHb→VTA neurons in TST- versus TST+ mice. Green and blue data points denote genes that are significantly enriched in cells from TST- versus TST+ mice, respectively. Gray data points represent genes that are not significantly enriched in either category (i.e. absolute value of Log2(Fold Change) < 2 and $p < 0.01$).
(J) Violin plots showing upregulation of *Kcnc1* gene expression in single-cells from TST+ compared to TST- mice. *Kcnc1* is also significantly higher expressed in TST- LHb→DR versus TST- LHb→VTA neurons, but not different between TST- LHb→DR versus TST+ LHb→VTA neurons.
(K) Regression analysis of differential gene expression between TST- LHb→VTA versus TST+ LHb→VTA neurons and between TST- LHb→DR versus TST- LHb→VTA neurons. For each gene, data points represent Log2 (Fold Change) values in both comparisons; colored data points highlight the same genes as identified in panels (H) and (I).

DISCUSSION

Relevance to depression symptomatology

The clinical manifestations of depression are highly variable, and patients with different symptoms are often grouped into the same diagnostic category even if they have distinct underlying pathophysiologies (Akil et al., 2018; Drysdale et al., 2017; Waters and Mayberg, 2017). Recent years have witnessed a growing awareness of this problem, and several attempts have been made to identify valid and meaningful subtypes based on symptoms, onset, course or severity (ten Have et al., 2016; van Loo et al., 2012; Musil et al., 2018). Importantly, a recent study suggested that patients with depression can be subdivided into four symptomatic subtypes based on distinct patterns of dysfunctional connectivity in limbic and frontostriatal circuits (Drysdale et al., 2017). In basic research, this issue is particularly challenging and often neglected when working with animal models of depression (Berton et al., 2012; Monteggia et al., 2018). Over the last decades, several animal models of depression that are based on chronic stress (CS) exposure have been used (Nestler and Hyman, 2010), but these models often do not discriminate between individual behavioral phenotypes. The fact that rodents, like humans, display a high degree of individual variability in responding to CS questions whether it makes sense to consider CS-exposed animals as a homogeneous population when searching for pathophysiological mechanisms.

To address this issue, we developed an approach that involves behavioral screening and classification of both non-stressed and stressed animals before studying underlying neurobiological mechanisms. While this strategy provides insights into assigning changes in circuit function, cell firing and gene expression to discrete behavioral patterns, one should proceed with caution. First, it remains uncertain whether depression should be defined as a collection of separable behavioral symptoms or as a single disorder that manifests itself in different behavioral pathologies. Therefore, understanding how neural circuits contribute to individual depression symptoms may not solve the neural basis of depression in its entirety. However, understanding the relationship between circuit and symptom is certainly an important and much-needed step towards establishing a platform for symptom-specific treatments of depression. Second, although our behavioral screening is based on paradigms that are widely use to assess depression-related behaviors in rodents (e.g. Tye et al., 2012; Knowland et al., 2017; Yang et al., 2018; Seo et al., 2018), additional measures of depression (e.g. cortisol levels, weight gain or loss, circadian abnormalities) may be necessary to further characterize D0-D3 subgroups and their relevance to depression. It is possible that other CMS-induced pathologies that have not been assessed in this study may contribute to the cellular and circuit adaptations in the LHb. Third, it remains uncertain whether the non-stressed mice that show LHb hyperactivity and increased PC possess a bona fide depression phenotype and future studies will need to determine whether they also exhibit other depression-related phenotypic markers. However, it is conceivable that some control mice develop a depression phenotype, for example, caused by stress during transportation or fighting with littermates within the cage. Fourth, while our approach produced resilient mice that did not show a depression-related phenotype, similar to the social defeat stress model (Krishnan et al., 2007), we noticed that CMS does not induce impairments in social interaction behavior, as in social defeat stress. Conversely, social defeat stress does not affect passive immobility in the TST or FST (Krishnan et al., 2007). Thus, each animal model may recapitulate different aspects of depression. Fifth, while our approach of subdividing depression phenotypes is based on categorial differences with boundaries that are defined by statistical procedures, it neglects the fact that there is a continuum in the severity of the symptoms which lacks sharp boundaries (Figure 1D). Thus, a

model with even greater precision in detecting meaningful subtypes would consider both qualitatively distinct phenotypes as well as quantitative differences in severity along an underlying continuum (ten Have et al., 2016). Despite these limitations, given that CS is a well-known trigger for depression in humans as well as for LHb hyperactivity (Figure 2; Li et al., 2011; Lecca et al., 2016; Yang et al., 2018) which can be reversed by antidepressant treatment (Yang et al., 2018; Shabel et al., 2014), our data points to the possibility that LHb→VTA hyperactivity may be linked to a specific symptom of major depression in humans that involves motivational impairments but not anxiety or anhedonia.

Circuit mechanisms of LHb hyperactivity

Although the outputs of the LHb to dopaminergic and serotoninergic neuromodulatory centers are of high biological importance to a broad range of psychiatric diseases (Hikosaka et al., 2008), relatively little is known about the effects of CS on projection-defined LHb subpopulations. While some studies suggested that depression-related LHb neuronal hyperactivity may occur throughout the LHb (Li et al., 2013; Yang et al., 2018), others pointed to specific LHb subtypes projecting to downstream structures such as the VTA (Li et al., 2011). By performing patch clamp recordings from projection-defined LHb neurons in mice, we found that CS-induced LHb hyperactivity was directly associated with the projection to downstream VTA/RMTg structures, but not the DR. Even though evoked firing and excitatory transmission was not altered in LHb→DR neurons, we cannot rule out that other CS-induced adaptations occur in these cells. Because evidence suggests a close link between the LHb and DR circuitry in depression and LHb lesions alleviate depression-related behaviors by increasing serotonin levels (Yang et al., 2008), it may be important to further examine this LHb subtype using other types of stress (e.g. social defeat stress).

We also examined whether LHb→VTA hyperactivity can be detected in vivo in freely behaving animals (Figure 3). Importantly, our data does not support the idea put forward by Yang et al. (2018) who showed that increased burst but not tonic activity in LHb neurons is instrumental for aversion behavior and multiple depression-like symptoms such as increased PC in the FST and anhedonia in the SPT. This may explain why simply increasing the number of spikes by using low frequency optogenetic stimulation of LHb→VTA neurons was sufficient to induce both place aversion and immobility in the TST. It is possible that discrepancies are due to differences in burst detection and analysis (see methods). Alternatively, it is conceivable that pathway-specific optogenetic stimulation may generate behavioral effects that are not induced by stimulation of cell bodies independent of their projection target (Tye et al., 2011). Nonetheless, our findings are largely consistent with recordings from LHb neurons in acute brain slices demonstrating an increase in tonic firing in depression-related states (Lecca et al., 2016; Li et al., 2011; Tchenio et al., 2017). Accordingly, we propose a model in which CS-induced increased burst and tonic firing of LHb→VTA neurons directly and indirectly affects different subtypes of VTA DA neurons, which may produce symptoms that are related to reduced motivation rather than a reduced ability to experience pleasure.

Aberrant circuit-specific synaptic plasticity in the LHb

Increasing evidence suggests that imbalances in glutamate transmission play a critical role in the development of depression (Pittenger and Duman, 2008; Thompson et al., 2015). In the LHb, changes in presynaptic plasticity have been reported which involve increased release probability

at glutamatergic synapses in congenitally helplessness rats (Li et al., 2011). However, the identity of the inputs that exhibit presynaptic adaptations was unknown. By combing ex vivo electrophysiology and optogenetics, we were able to selectively examine specific inputs to LHb→VTA neurons in response to CS. As a result, we could link the effects of stress-induced changes in presynaptic release probability to a specific set of excitatory inputs that originate from the EP and make direct monosynaptic connections onto LHb→VTA neurons. In addition to these presynaptic adaptations at the EP synapse, we also discovered postsynaptic changes that involve an increased surface expression of GluR2-lacking AMPARs. These results are in line with the finding that upregulation of the beta form of calcium/calmodulin-dependent protein kinase type II resulted in increased expression of GluR1 AMPAR subunits at the plasma membrane of LHb neurons (Li et al., 2013). Strikingly, by increasing or decreasing the neural activity of EP→LHb neurons in vivo, we were able to selectively modulate immobility behavior in the TST and FST, but not anhedonia or anxiety. Although our results suggest that CS induces pre- and postsynaptic adaptations of excitatory EP inputs to LHb→VTA neurons, which may contribute to hyperactivity of these cells, our in vivo manipulations targeted all EP neurons that project to the LHb. The EP also contains a separate population of cells that co-releases GABA and glutamate in the LHb and it is possible that changes in inhibitory and excitatory inputs operate in concert to promote LHb hyperactivity and depression-related behaviors (Lecca et al., 2016; Shabel et al., 2014). Because EP neurons that release only glutamate or co-release GABA and glutamate can be differentiated based on the expression of parvalbumin or somatostatin markers, respectively, (Wallace et al., 2017) future research will be needed to investigate the precise contribution of each neuronal subtype to CS-induced LHb dysfunction.

Lastly, we found that most excitatory EP inputs do not target LHb→DR neurons directly. LHb cells that interact within the LHb through local glutamatergic connections have been reported previously (Kim and Chang, 2005; Weiss and Veh, 2011), and the idea that excitation of LHb→DR neurons by EP inputs involves a local feedforward mechanism is supported by several lines of evidence. First, we found an anatomical separation of EP terminals and LHb→DR cell bodies. Second, we detected an increased peak response latency for EP inputs to LHb→DR neurons. Third, 4-AP did not rescue TTX-blocked EPSCs from EP to LHb→DR neurons. Fourth, we found a higher number of local LHb neurons that are connected with LHb→DR compared to LHb→VTA neurons. Thus, an intriguing possibility is that LHb→DR neurons lack CS-induced hyperactivity because of fundamental differences in LHb circuit architecture. An important future research direction is to examine the precise role of local glutamatergic connectivity in the LHb in light of the differential stress susceptibility of LHb subpopulations reported here.

Identification of circuit-specific biomarkers based on behavioral phenotyping

Acute and CS-induced transcriptional dysregulations have been demonstrated in several brain regions (Akil et al., 2018; Bagot et al., 2016), but the effects of CS on the regulation of gene expression in the LHb have not yet been examined. We developed a platform based on single-cell transcriptomics that allowed us to determine potential molecular biomarkers that are associated with circuit-specific neural dysfunction (hyperactivity of LHb→VTA) and specific behavioral phenotypes (Figure 7). We argue that behavioral phenotyping in response to CS is critical because simply comparing stressed versus non-stressed animals may not identify specific biomarkers due to the heterogeneity of behavioral phenotypes. Consistent with this, we find that experience dependent classification (i.e. CTRL versus CMS; Figure S8) revealed fewer and more modest

differences in our gene expression analysis of LHb→VTA neurons compared to phenotypic classification. Because animals were analyzed solely based on whether they were positive or negative for TST, it remains uncertain, as mentioned earlier, whether the TST positive animals have a bona fide depression phenotype. Thus, future studies are needed to examine whether candidate genes discovered based on behavioral phenotyping can serve as true biomarkers for depression. For instance, cell type-specific editing of candidate genes using CRISPR-Cas9 may be a particularly fruitful approach towards understanding how molecular dysfunction gives rise to LHb hyperactivity and depression-related behaviors. These approaches will yield valuable insights for translational research, given that the LHb is a phylogenetically conserved structure that is present in virtually all vertebrate species and that depression-related LHb hyperactivity has been observed in both animals and humans.

AUTHOR CONTRIBUTIONS

Stereotactic injections - I.C. Immunohistochemistry – I.C., F.K., S.K.O. Electrophysiology - I.C., J.R.P. Behavior experiments – I.C. J.W.J., H.Y. RNASeq and bioinformatics - J.W., D.L., I.C., C.F. Critical viral reagents - V.L., B.K.L. Study design - I.C., S.L. Analysis and Interpretation - I.C., C.F. and S.L. Manuscript writing - I.C., C.F. and S.L.

METHODS

Experimental model and subject details

C57BL/6 mice (Jackson Laboratory, 25-35 g, 8-12 weeks old, male) were used for all experiments. Mice were maintained on a 12:12 hr light cycle (lights on at 07:00). All procedures complied with the animal care standards set forth by the National Institutes of Health and were approved by University of California Berkeley's Administrative Panel on Laboratory Animal Care.

Stereotaxic surgeries

As previously described (Lammel et al., 2012) all stereotaxic injections were performed under general ketamine–dexmedetomidine anesthesia using a stereotaxic instrument (Kopf Instruments, Model 1900). For red/green fluorescent retrobead labeling, mice were injected unilaterally with fluorescent retrobeads (200 nL; LumaFluor Inc.) in the ventral tegmental area (VTA, bregma: -3.4 mm, lateral: 0.4 mm, ventral: 4.4 mm) or dorsal raphe nucleus (DR, bregma: -4.55 mm, lateral: 0 mm, ventral: 3.35 mm) using a 1 µL Hamilton syringe (Hamilton). The AAVs (adeno associated virus) used in this study were from the Deisseroth laboratory (AAV5-EF1α–DIO-hChR2(H134R)-eYFP; AAV5-EF1α-DIO-eYFP; AAV5-CaMKII-ChR2-eYFP; ~10^{12} infectious units per mL, prepared by the University of North Carolina Vector Core Facility), from the Uchida laboratory (AAV5-flex-RG; AAV5-flex-TVA-mCherry; ~10^{12} infectious units per mL, prepared by the University of North Carolina Vector Core Facility), or from Addgene (AAV-DIO-hM3DGq-mCherry and AAV-DIO-hM4DGi-mCherry). ΔG-Rabies-GFP and RV-EnvA-ΔG-GFP were from Salk Institute. CAV2-Cre was from Plateforme de Vectorologie de Montpellier. RG-EIAV-Cre was from the Lim laboratory (UC San Diego). For viral injection, 300-500 nL of concentrated virus solution was injected into the lateral habenula (LHb, bregma: -1.6 mm, lateral: 0.5 mm, ventral: 3.15 mm), entopeduncular nucleus (EP, bregma: -1.2 mm, lateral: 1.85 mm, ventral: 4.4 mm), lateral hypothalamus (LH, bregma: -0.8 mm, lateral: 1.0 mm, ventral: 5.1 mm), VTA or DR (same coordinates as above) using a syringe pump (Harvard Apparatus) at 150 nL/min. The injection needle was withdrawn 5 min after the end of the infusion. For *in vivo* optogenetic experiments, mice received unilateral (**Figure S3**) or bilateral (**Figure S6**) implantation of a chronically implanted optical fiber (NA = 0.22; Doric Lenses) dorsal to the LHb (bregma: 1.65 mm, lateral: ±0.6 mm, ventral: 2.47 mm), VTA (bregma: -3.4 mm, lateral: 0.4 mm, ventral: 3.9 mm) or DR (bregma: -4.55 mm, lateral: 0 mm, ventral: 2.85 mm). One layer of adhesive cement (C&B Metabond; Parkell) was followed by acrylic (Jet Denture Repair; Lang Dental) to secure the fiber to the skull. The incision was closed with a suture and tissue adhesive (Vetbond; 3M). The animal was kept on a heating pad until it recovered from anesthesia. Experiments were performed 6-8 weeks (for AAVs) or 3 days (for retrobeads) after stereotactic injection. Injection sites and optical fiber placements were confirmed in all animals by preparing coronal sections (100 µm) of injection and implantation sites. We routinely carried out complete serial reconstruction of the injection sites and optical fiber placements.

Although fluorescent retrobeads and retrograde viruses were targeted to the VTA, it is important to mention that the caudal VTA contains at least some parts of the rostromedial tegmental nucleus (RMTg; Jhou et al., 2009). The boundary between the VTA and RMTg is difficult to determine, particularly in the caudal VTA, which makes it difficult to determine with certainty whether retrogradely labeled LHb neurons are projecting to the VTA or RMTg. Thus, when referred to in the text, the VTA includes the RMTg, which was originally termed the 'tail of the VTA' (Kaufling et al., 2009).

Chronic mild stress

The chronic mild stress (CMS) animal model of depression has been used extensively to study the pathophysiology of depression in rodents (Frisbee et al., 2015; Willner et al., 1992). This model is based on the fundamental concept that chronic exposure to stressors is an important cause for the development of depression in humans. Animals were exposed to a randomized series of mild stressors on a daily basis. Specifically, two stressors per day for 8 weeks were delivered before behavioral screening. Mice experienced one stressor during the day and a different stressor during the night. Well-validated and approved standard stressors (Frisbee et al., 2015; Willner et al., 1992; Tye et al., 2012) were randomly chosen from the following list so that they are unpredictable for the subjects: cage tilt on a 45º angle for 12 to 16 h; food deprivation for 12 to 16 h; strobe light illumination for 2 to 6 h; crowded housing for 2 to 6 h; cage shaking (100 RPM) for 2 to 6 h; individual housing for 2 to 6 h; continuous illumination for 24 to 36 h; continuous darkness for 24 to 36 h; water deprivation for 12 to 16 h; damp bedding (200 mL water poured into bedding) for 12 to 16 h; bedding removal for 12 to 16 h. When not undergoing food or water deprivation stressors, water and food were available *ad libitum*. Non-CMS (control, CTRL) animals were housed for 8 weeks under standard housing conditions with access to food and water *ad libitum*. Most CTRL and CMS mice underwent three behavioral screening tests on three consecutive days in the following order: 1. Elevated plus maze (EPM), 2. Sucrose Preference Test (SPT), 3. Tail Suspension Test (TST). However, some mice shown in **Figure 1A-1C** did not experience all three behavioral screening tests, and some animals also underwent a social interaction test (SIT; **Figure S1**). In addition, for the data shown in **Figures 6 and S6**, all mice also underwent an open field locomotor test (OFT), which was performed on the fourth day.

Electrophysiology

Ex vivo electrophysiology: Mice were deeply anaesthetized with pentobarbital (200 mg/kg IP; Vortech). Coronal slices (250 μm) were prepared after intracardial perfusion with ice-cold artificial cerebrospinal fluid (ACSF) containing (in mM) 50 sucrose, 125 NaCl, 25 $NaHCO_3$, 2.5 KCl, 1.25 NaH_2PO_4, 0.1 $CaCl_2$, 4.9 $MgCl_2$, and 2.5 glucose (oxygenated with 95% O_2/5% CO_2). After 60 min of recovery, slices were transferred to a recording chamber and perfused continuously at 2-4 mL/min with oxygenated ACSF, containing (in mM) 125 NaCl, 25 $NaHCO_3$, 2.5 KCl, 1.25 NaH_2PO_4, 11 glucose, 1.3 $MgCl_2$ and 2.5 $CaCl_2$ at ~35 ºC. For recording of excitatory postsynaptic currents (EPSCs), picrotoxin (50 μM, Sigma) was added to block inhibitory currents mediated by $GABA_A$ receptors. Miniature excitatory postsynaptic currents (mEPSCs) were recorded at -70 mV in the presence of 1 μM tetrodotoxin (TTX, Hello Bio) and 50 μM picrotoxin. Cells were visualized with a 40x water-immersion objective on an upright fluorescent microscope (BX51WI; Olympus) equipped with infrared-differential interference contrast video microscopy and epifluorescence (Olympus). Patch pipettes (3.2-4.4 MΩ) were pulled from borosilicate glass

(G150TF-4; Warner Instruments) and filled with internal solution, which consisted of (in mM) 117 $CsCH_3SO_3$, 20 HEPES, 0.4 EGTA, 2.8 NaCl, 5 TEA, 4 MgATP, 0.3 NaGTP, 5 QX314, 0.1 Spermine, pH 7.35 (270–285 mOsm). For recordings of action potential firing from retrogradely labeled LHb neurons, the internal solution contained (in mM): 135 K-gluconate, 5 KCl, 10 HEPES, 0.1 EGTA, 2 $MgCl_2$, 2 MgATP, 0.2 NaGTP, pH 7.35 (290-300 mOsm). Electrophysiological recordings were made using a MultiClamp700B amplifier and acquired using a Digidata 1550 digitizer, sampled at 10 kHz, and filtered at 2 kHz. All data acquisition was performed using pCLAMP software (Molecular Devices).

ChR2-expressing axon terminals were stimulated by flashing 473 nm light through the light path of the microscope using an ultrahigh-powered light-emitting diode (LED) powered by an LED driver (Prizmatix) under computer control. A dual lamp house adaptor (Olympus) was used to switch between fluorescence lamp and LED light source. The light intensity of the LED was not changed during the experiments and the whole slice was illuminated (5 mW/mm^2). Light-evoked EPSCs were obtained every 10 s with one pulse of 473 nm light (5 ms) with neurons voltage clamped at -70 mV, -40mV, 0 mV or +40 mV. Light-evoked EPSC amplitudes were calculated by averaging responses from 10 sweeps and then measuring the peak amplitude in a 20 ms window after the light pulse. Cells that did not show a peak in this window that exceeded the baseline noise were classified as non-responders (**Figure 4G**). Series resistance (5–25 MΩ) and input resistance were monitored online. Neurons were voltage-clamped at -70 mV to record AMPAR EPSCs and at +40 mV to record dual component EPSCs containing AMPAR and NMDAR EPSCs. To calculate the AMPAR/NMDAR ratio at +40 mV, an average of 10 consecutive EPSCs at +40 mV was computed before and after application of the NMDAR antagonist D-AP5 (50 μM for 5 min). NMDAR EPSCs were generated by subtracting the average EPSC in the presence of AP5 from that recorded in AP5's absence. The peak of the AMPAR EPSC (2 ms window compared to a 2 ms window on the baseline) was divided by the peak of the NMDAR EPSC to yield an AMPAR/NMDAR ratio. The rectification index was calculated by dividing the amplitude of the AMPAR EPSCs measured at -70 mV by the amplitude at +40 mV. The decay time constant (τ) of the AMPAR and NMDAR EPSCs at +40 mV was calculated by fitting a double exponential function to each average EPSC and using the following formula $\tau = [(A_1 \times \tau_1) + (A_2 \times \tau_2)] / (A_1 + A_2)$; where A_1 and A_2 are the amplitudes and τ_1 and τ_2 are the decay time constants of the fast and slow components respectively. Paired-pulse ratios (PPR) were recorded at -70 mV with a 100 ms interval and calculated by dividing the mean amplitude of the second peak by the mean amplitude of the first peak (i.e. averaged responses from 10 sweeps).

For recordings of action potential firing (**Figures 2 and 7**), cells were held in current clamp and 2 s ramps of depolarizing currents (+50 pA, +100 pA or +150 pA) were injected. Notably, 89.4% of all recorded LHb→VTA (n = 93/104 cells) and 92.6% of all LHb→DR (n = 50/54 cells) neurons were silent and did not fire spontaneous action potentials under resting conditions. These percentages are substantially smaller than reported previously for recordings from non-projection-defined LHb neurons (Yang et al., 2018). No differences in the number of spontaneous action potentials were observed between $CTRL_{D0\text{-}1}$ and $CMS_{D2\text{-}3}$ animals. As most projection-defined LHb neurons were silent in our whole-cell recordings, we transiently hyperpolarized the cells, which resulted in action potential firing under resting conditions. We noticed that some cells switched between burst and tonic firing. For these cells, we defined them as bursting if > 50% of spikes in a 5 s interval were in bursts or tonic if < 50% were in bursts (**Figure 7C**)

For the pharmacological experiments in **Figure 5C**, we recorded baseline responses for 4 min and bath applied 30 μM NASPM (1-naphthyl acetyl spermine, Tocris) for 6 min, which selectively blocked GluR2-lacking AMPARs. For the experiments in **Figure 5G**, we first recorded baseline EPSCs and then added the voltage-gated sodium channel antagonist TTX (1 μM) and subsequently the potassium channel antagonist 4-aminopyridine (4-AP, 50 μM, Sigma) to the bath solution in order to isolate monosynaptic inputs (Petreanu et al., 2009). All electrophysiological data were analyzed offline using Clampfit (Molecular Devices) or Matlab (MathWorks).

In vivo electrophysiology and burst analysis: Animals were implanted with a custom-built driveable optoelectrode (optrode) above the LHb, which consisted of four tetrodes (12 μm polyimide-coated NiCr wire protected by silica tubing) glued to the 200 μm optical fiber using epoxy. The tetrodes protruded from the tip of the optical fiber by ~0.5 mm. Wire tips were cut flat and gold-plated to reduce electrode impedances to ~200 kΩ at 1 kHz. A small screw fixed to the skull served as a ground electrode. Data collection began one week after the optrode implantation. Neural signals were recorded using a Digital Lynx 4SX system (Neuralynx) and HS-18-MM headstage pre-amplifier (Neuralynx). Recorded signals were filtered between 0.6 and 6 kHz and sampled at 32 kHz. Spikes were sorted offline using SpikeSort 3D (Neuralynx) software. At the end of each recording session, the optrode was moved ventrally for ~80 μm. The final recording location was verified using histology after the electrolytic lesions (12 μA, 30 s).

ChR2-tagged neurons were identified by delivering 473 nm (10 mW/mm^2, 5 ms pulses) light at 1 Hz frequency for 2 min (120 trials of 1s). A 2 ms bin with the highest number of spikes in the interval [0, +100 ms] around the laser pulse was identified. To test if the identified strongest response to light was higher than chance, we shuffled all the spike times in the same [0, +100 ms] interval 10,000 times and counted the highest number of spikes in a 2 ms bin for each iteration. If the number of spikes in the 2 ms bin from the real data exceed the 99.9th percentile value of the distribution of number of spikes in the most active 2 ms bin for the shuffled data, we classified the cell as light-responsive. Response latency was defined as the average response time in the most active 2 ms bin (**Figure S4E**; adapted from Zhang et al., 2013).

Bursts in spike trains were detected using a "Rank Surprise" burst detection algorithm (Gourévitch and Eggermont, 2007). First, all interspike intervals (ISIs) in the spontaneous spike train were assigned a rank (R_n), with the shortest ISI getting rank one and the longest ISI getting the last rank. Next, we define u as the sum of ISI ranks in a burst with q spikes, where $u = R_{n1} + R_{n2} + \ldots + R_{q-1}$. We expect a burst with q number of spikes to have ISIs with short values, i.e. small R_n sums of the ISIs in that burst. We then defined T_q as the sum of q discrete uniform random variables between 1 and N, where N is the total number of ISIs in the spike train ($N = q - 1$). Intuitively, we would expect a burst to have smaller u compared to T_q; however, this would be a *surprise* if all the spike time values were independently and uniformly distributed. This degree of surprise can be defined as rank surprise (RS) statistic:

$$RS = -\log(P(T_q \leq u)),$$

where $P(T_q \leq u)$ is the probability that burst in question have higher or equal ISI rank sum than the sum of random independent and uniformly distributed ISI ranks. To identify "true bursts" we intended to keep this probability low (i.e. make the RS high), so we would only identify bursts with such small ISIs sums that those sums would not be observed by summing random uniformly distributed ISI ranks. Once the RS statistic is defined, possible bursts were identified in the spike

trains and compared to the RS statistic. A candidate burst that has higher RS than our defined one was identified as a burst. See (Gourévitch and Eggermont, 2007) for more details on how candidate bursts are selected from the spike train. The largest acceptable interspike interval value in a burst was set to 100 ms and the minimum significance for the surprise statistic was set to 5% (i.e. RS = -log(0.05)).

The RS burst detection algorithm is preferable over a simple ISI-threshold burst detection method. In the ISI-threshold method, researchers have to define an ISI threshold for burst initiation (maximum ISI between two consecutive spikes for these spikes to be still considered as the first two spikes in the burst) and burst termination (maximum ISI between two consecutive spikes for the last of these two spikes to be still considered part of a burst). The latter parameter is particularly problematic as it heavily depends on the firing rate of a cell. A common ISI threshold for burst termination is 100 ms (Yang et al., 2018). This means that the ISI interval between the last two spikes in the burst can be up to 100 ms. If this threshold is applied to cells with mixed tonic and burst firing and these cells fire above 10 Hz (mean firing rate of LHb→VTA cells in $CMS_{D2\text{-}3}$ group: 13.8 ± 1.9 Hz), it results in many false positive additions of spikes to bursts. By chance, a cell that fires at 10 Hz may have many ISI intervals ≤ 100 ms, meaning that a lot of tonic spikes would be added to the end of identified bursts. RS burst detection solves this problem by taking the firing rate of the cell into consideration.

Behavioral Assays

All behavioral tests were performed during the light phase in a temperature (68-74°F) and humidity (40-60%) controlled room that is illuminated by eight 32 W fluorescent lights each producing 2925 lumens (TST and EPM apparatus were 7 feet away from the light source; SPT and FR/PR were carried out in boxes where light source was a single 0.6 W light bulb). All behaviors were carried out between 9 am and 6 pm. SPT and FR/PR behaviors were carried out in sound proof behavioral boxes. All behaviors were carried out without the experimenter being present in the room. Behavioral equipment was cleaned with 70% EtOH between individual animals.

Tail Suspension Test (TST): The TST (Can et al., 2012a) involves hanging the mouse by the tail using tape, where one end of the tape is secured to a horizontal bar 40 cm from the ground, thus ensuring that the animal cannot climb on other objects during the assay. Over the course of the experiment (6 min), the mouse switches from vigorous struggling behavior to increasing immobility. The experiment was recorded on video and the time spent struggling was measured by blind scoring of the video after testing was completed. Experimenters were blinded to allocation of groups and outcome assessment.

For optogenetic experiments (**Figure S6**), the animals' fiberoptic implant was connected to a 473 nm DPSS laser diode (Laserglow) using a fiberoptic cable and rotary adaptor. Laser output was controlled using a Master-8 pulse stimulator (A.M.P.I.). Power output for the cable was tested using a digital power meter (Thorlabs) and was checked before and after each experimental animal; output during light stimulation was estimated at the targeted tissue 200 μm from the fiber tip (www.optogenetics.org/calc). Animals expressing ChR2 (or eYFP) received 473 nm light stimulation (10 Hz, 5-8 mW/mm^2, 5 ms pulses) during the experiment.

For chemogenetic experiments (**Figure 6**), animals expressing DREADDs (or eYFP) were injected intraperitoneally with 4 mg/kg CNO (in 0.5% DMSO) 30 min before the start of the

experiment. Injections of 4 mg/kg CNO in C57BL/6 mice did not significantly alter struggling in the TST, sucrose preference in the SPT, time in open arms in the EPM or locomotor activity in the OFT when compared to C57BL/6 mice injected with 0.9% saline of an equivalent volume (data not shown).

Sucrose Preference Test (SPT): The SPT assesses an animal's preference for a sweet solution (1% sucrose dissolved in water) relative to plain water, and failure to do so is indicative of anhedonia, a core symptom of depression. Volume of sucrose or water consumed was measured using a computer-controlled 'lickometer'. Specifically, a Med Associates operant chamber was used to count every tongue contact made ('licks') with bottle spouts from either the 1% sucrose solution or water alone. Animals were water-restricted overnight before the experiment. Bottle side and animal group tested were counterbalanced between each trial. Testing was for 90 min and the percentage of sucrose solution over total consumption was calculated. Mice that made in total < 30 licks at any port were excluded from the experiment. Experimenters were blinded to allocation of groups and outcome assessment.

For optogenetic experiments (**Figure S6**), the stimulation parameters were identical to the TST (see above). For the chemogenetic experiments **(Figure 6**), animals expressing DREADDs (or eYFP) were injected intraperitoneally with 4 mg/kg CNO (in 0.5% DMSO) 20 min before the start of the experiment.

Elevated Plus Maze (EPM): The EPM test is used as a measure of anxiety-related behavior in rodents (Tye et al., 2011). During the test, mice explore a plus shaped maze (length of each arm: 91 cm). Two arms were closed (wall height: 38 cm) and two arms were open. Mice typically spent time exploring all arms, but a substantial amount of time spent in the closed arms compared to open arms is indicative of anxiety-related behavior. Animals were placed in the EPM for 10 min. The movement of the mice was recorded via an automated video tracking system (Biobserve) and the time spent in open and closed arms was calculated. Experimenters were blinded to allocation of groups and outcome assessment.

For optogenetic experiments (**Figure S6**), the stimulation parameters were identical to the TST (see above). For the chemogenetic experiments **(Figure 6**), animals expressing DREADDs (or eYFP) were injected intraperitoneally with 4 mg/kg CNO (in 0.5% DMSO) 30 min before the start of the experiment. Note that two mice jumped from the EPM platform during the experiment and these animals were excluded from the data shown in **Figures 6B and 6H**.

Social Interaction Test (SIT): The SIT is widely used in rodents to assess sociability and interest in social novelty. The social interaction testing apparatus was a rectangular three-chamber clear Plexiglas box (20 cm L × 40.5 cm W × 22 cm H). During the habituation phase, experimental mice were placed in the box for a 10 min session. Afterwards, an unfamiliar stranger mouse (stranger 1) was placed in a round wire cup at the corner of the box. The wire cup (7 cm L × 10 cm H) had small holes which allowed contact between mice, but prevented fighting. At the opposite corner, a second empty wire cup was located. The animals used as strangers were male C57BL/6 mice which were previously habituated to the placement in the cup. The location of strangers in the apparatus (i.e. left versus right side cups) was counterbalanced between mice and trials. In the first phase of the test (sociability test), the experimental mouse was placed in the box and allowed to

explore for 10 min. The movement of the mice was recorded via an automated video tracking system (Biobserve) and the time spent exploring the wire cups was evaluated. Sociability was defined as the preference for the cup containing a novel mouse over an empty cup. At the end of the first 10 min session, each mouse was tested in a second 10 min session to evaluate the interest in social novelty. A second, unfamiliar C57BL/6 mouse (stranger 2) was placed in the empty cup. The amount of time spent exploring the wire cups was evaluated again during the second 10 min session. Social novelty indicates the preference for cup containing the unfamiliar, newly introduced second mouse compared to the familiar mouse. Experimenters were blinded to allocation of groups and outcome assessment.

Forced swim test (FST): The FST is a behavioral challenge assay that, similar to the TST, assesses passive coping (PC; Can et al., 2012b). Mice were placed in a transparent glass beaker filled with ~25 °C tap water. The water level in the beaker was high enough so mice could not touch the bottom of the beaker while they were trying to stay afloat. The behavioral test lasted for 6 minutes and mice were recorded on video during the entire session. Typically, in the beginning of the test mice struggled vigorously, but eventually they switched to a more passive floating state. Only the last 4 minutes were analyzed due to the fact that most mice are very active in the first 2 minutes of the test. The time spent struggling was measured by blind scoring of the video after testing was completed. Experimenters were blinded to allocation of groups and outcome assessment.

For chemogenetic experiments (**Figures S6C and S6D**), animals expressing $hM3DG_q$ DREADDs (or mCherry) were injected intraperitoneally with 4 mg/kg CNO (in 0.5% DMSO) 30 min before the start of the experiment.

Fixed and progressive ratio operant tasks (FRT and PRT): FRT and PRT are commonly used to evaluate effort-related motivated behavior in rodents (Hodos, 1961). In both tasks, mice were trained to make a choice between two nose pokes, one of which was rewarded with a sugar pellet. Experiments were performed in Med Associates operant chambers. Mice were food restricted to 90-95% of their body weight prior to training and testing periods. In the FRT, mice had to make one correct nose poke to receive a sucrose pellet. Subsequently, there was a 10 s timeout period where repeated correct nose pokes were not rewarded. Each FRT session lasted for 1 hr. Mice that learned to choose the correct nose poke to receive the reward were selected for the subsequent PRT. In the PRT, mice had to make a progressively higher number of correct nose pokes to receive a sucrose pellet; the number of nose pokes required to receive a sucrose pellet was calculated based on $[5e^{(R*0.2)}] - 5$ (Richardson and Roberts, 1996). After each successful sucrose pellet delivery, there was again a 10 s timeout. Each PRT session lasted a maximum of 3 hours, or it was stopped when no correct nose pokes were made for 10 min. The total number of correct nose pokes mice made during a PRT session was used to evaluate motivated behavior. A higher number of correct nose pokes is indicative of an increased effort to obtain a reward (i.e. increased motivation).

For chemogenetic experiments, animals expressing DREADDs (or eYFP) were injected intraperitoneally with 4 mg/kg CNO (in 0.5% DMSO) or the equivalent volume of 0.9% saline solution (in 0.5% DMSO) 20 min before the start of the experiment. Experimenters were blinded to allocation of groups and outcome assessment.

Real-time Place Preference / Aversion: Mice with fiberoptic implants were connected to a fiberoptic cable and placed in a custom-made three-compartment chamber (Lammel et al., 2012). One randomly assigned side of the chamber was assigned as the initial stimulation side (Phase 1), and after 10 min the stimulation side was switched to the previously non-stimulated side of the chamber (Phase 2). The two stimulation sides were separated by a neutral middle compartment. At the start of each session, the mouse was placed in the neutral compartment, and every time the mouse crossed to the stimulation side, 473 nm laser stimulation (10 Hz, 10 mW/mm^2, 5 ms pulses) was delivered until the mouse crossed back into the neutral, non-stimulation side. There was no interruption between Phase 1 and Phase 2. The movement of the mice was recorded via a video tracking system (Biobserve) and the time spent in each area (stimulated, non-stimulated, neutral) was calculated.

Open Field Test (OFT): The open-field test was conducted to measure the effect of optogenetic or chemogenetic manipulations on general locomotor ability. The mice were placed in a custom-made open field chamber (50 cm L × 50 cm W × 50 cm H) and their movement was recorded and analyzed for 10 min using video-tracking software (Biobserve).

For optogenetic experiments (**Figure S6**), the stimulation parameters were identical to the TST (see above). For the chemogenetic experiments **(Figure 6**), animals expressing DREADDs (or eYFP) were injected intraperitoneally with 4 mg/kg CNO (in 0.5% DMSO) 30 min before the start of the experiment. Experimenters were blinded to allocation of groups and outcome assessment.

Whole brain input mapping

We used monosynaptic rabies virus tracing to map and characterize inputs to different LHb subpopulations (Osakada and Callaway, 2013). Specifically, mice were injected with 150 nL AAV-FLEX-TVA (i.e. a cellular receptor for subgroup A avian leukosis viruses) and 150 nL AAV-FLEX-RG (i.e. rabies virus glycoprotein) into the LHb and 300 nL CAV2-Cre into either VTA or DR. 4 weeks later, 300 nL RV-EnvA-ΔG-GFP (i.e. glycoprotein deficient, GFP expressing rabies virus with the envelope protein from avian ASLV type A) was injected into the LHb. 7 days after injection, mice were perfused with 4% PFA in PBS. Brains were stored in 10% sucrose in PBS at +4˚C overnight and then processed for analysis. For input mapping, 100 µm sections of the whole brain were prepared and imaged using an Axio Imager 2 microscope (Zeiss). GFP-expressing input cells to LHb→VTA or LHb→DR neurons were counted manually. Animals were randomized and investigators were blinded to group allocation (i.e. projection target).

Next-generation single-cell RNA sequencing

Sample collection: Procedure was described previously in Földy et al., 2016. To minimize interference with subsequent molecular experiments, only a small amount of intracellular solution (~1 µl; not autoclaved or treated with RNase inhibitor) was used in the glass pipette during electrophysiological recordings. Before and during recording, all surface areas - including manipulators, microscope knobs, computer keyboard, etc. - that the experimenter needed to contact during the experiment were cleaned with RNaseZAP solution (Sigma). After whole-cell patch-clamp recordings, the cell's cytosol was aspirated via the glass pipette used during the recording. Although the aspirated cytosol may have contained genomic DNA, our choice of cDNA

preparation, which involved poly-A based mRNA selection, virtually eliminated the possibility of genomic contamination in the RNAseq data. For sample collection, we quickly removed the pipette holder from the amplifier head stage and used positive pressure to expel samples into microtubes containing cell collection buffer while gently breaking the glass pipette tip. Cell collection microtubes were stored on ice until they were used.

cDNA library preparation: Described previously in Földy et al., 2016. Briefly, single-cell mRNA was processed using Clontech's SMARTer Ultra Low RNA Input v4 or SMART-Seq HT kit. As a first step, cells were collected via pipette aspiration into 1 µL of 10x collection buffer, and were spun briefly and snap frozen on dry ice. Samples were stored at −80°C until further processing, which was performed according to manufacturer's protocol. Resulting cDNA was harvested and analyzed on a Fragment Analyzer (Advanced Analytical). Library preparation was performed using Nextera XT DNA Sample Preparation Kit (Illumina) as described in the protocol. Following library preparation, cells were pooled and sequenced using NextSeq 150 high-output kit in an Illumina NextSeq 500 System with 2x75 paired-end reads.

Processing of RNA sequencing data: After sequencing, raw reads were de-multiplexed and pre-processed using Trimmomatic and Flexbar. Then, raw sequencing reads were aligned to the Ensembl GRCm38 reference transcriptome (Version-2015-06-25), using the STAR aligner with the following parameters: trimLeft=10, minTailQuality=15, minAverageQuality=20 and minReadLength=30. 'Single-end/paired-end' and 'sense/antisense/both' options. Gene counts were calculated using featureCounts. For convenience, Ensembl gene IDs were converted to gene symbols using the mouse GRCm38 gtf file (ftp://ftp.ensembl.org/pub//release 86/gtf/mus_musculus/Mus_musculus.GRCm38.86.gtf.gz) as a reference. In the few cases where different Ensembl gene IDs identified the same gene symbol, average gene counts were used.

Gene categories: Altogether, expression of N = 22,800 genes were analyzed ('All'). This list was generated using Ensemble Biomart, with the following specifications "Database=Ensembl Genes 85, Dataset=Mus Musculus genes (GRCm38.p4), Attributes=Ensemble Gene ID and Associated Gene Name". 'CAM' (N = 396) and 'ion channel' (N = 207): these categories included genes as described previously (Földy et al., 2016).

Quality control: All data analysis was performed using Python. First, for each cell, we calculated the number of unique genes and the fraction of aligned reads. Second, we calculated the mean and standard deviation of these two values across all cells. Cells that had both values less than 1 standard deviation below the mean, or had one value above the mean and the other less than 1.5 standard deviations below the mean were considered to pass quality control. For the rest, we calculated their correlation (minimum of Pearson and Spearman) against the average of all cells within their respective cell type that passed quality control. Cells with correlation >0.4 were considered to pass quality control, otherwise they failed quality control.

Normalization of gene expression: After quality control, cells (represented by raw gene count vectors) were pooled together and normalized using *scran* (Lun et al., 2016), with sizes 20, 40, 60, 80, 100. Cells that had negative or zero size were removed. For further analysis, gene counts were

converted into log-space by the $g_i' = ln(1 + g_i)$ transformation, where g_i was the normalized gene count of the i-th gene.

Histology and microscopy

Immunofluorescence and confocal microscopy were performed as described previously in Lammel et al., 2012. Briefly, after intracardial perfusion with 4% paraformaldehyde in PBS, pH 7.4, the brains were post-fixed overnight and coronal brain sections (100 or 50 μm) were prepared. Sections were stained overnight in a primary antibody solution (mouse anti-Cre (1:200, Sigma). Twenty-four hours later, sections were stained for 4 hours in secondary antibody solution (goat anti-mouse Alexa Fluor 488, Thermo Fisher). Image acquisition was performed with Zeiss LSM710 laser scanning confocal microscope using 20x or 40x objectives and on a Zeiss Axio Imager 2 upright widefield fluorescence/differential interference contrast microscope with charge-coupled device camera using 5x or 10x objectives. Confocal images were analyzed using ImageJ. Sections were labeled relative to bregma using landmarks and neuroanatomical nomenclature as described in "*The Mouse Brain in Stereotaxic Coordinates*" (Franklin and Paxinos, 2013).

Quantification and statistical analysis

In order to determine whether individual animals were positive or negative for a specific behavioral phenotype as measured in the EPM, SPT and TST, we used receiver operating characteristic (ROC) curves (Zou et al., 2007). ROC curve analysis has been used extensively in clinical epidemiology for the assessment of diagnostic ability of biomarkers and imaging tests in classification of diseased from healthy subjects (Metz, 1978; Swets, 1988; Zweig and Campbell, 1993). It is considered the most objective method for evaluating and comparing classification performances and recommended for the evaluation of binary classifiers (Berrar and Flach, 2012; Søreide, 2009). ROC curves are uninfluenced by decision biases and prior probabilities and they depict a classifier's performance over the range of thresholds for sensitivity and specificity. Youden J Index was calculated from ROC curves in order to identify the optimal cutoff value that gives the lowest false positive rate (FPR) and the highest true positive rate (TPR). Youden J index maximizes the difference between TPR (sensitivity) and FPR (1 – specificity):

$$\text{Youden J Index} = \text{TPR} - \text{FPR} = \text{Sensitivity} + \text{Specificity} - 1.$$

Thus, by maximizing (Sensitivity + Specificity) across various cutoff points, the optimal cutoff point was calculated.

In order to determine statistical differences for anatomical, behavioral and electrophysiological data, we performed Student's t tests (paired and unpaired), and one- and two-way ANOVAs using Prism 7 (Graphpad). Bonferroni, Tukey's or Sidak's post hoc analysis was applied, when applicable, to correct for multiple comparisons. Statistical significance was * $p < 0.05$, ** $p < 0.01$, *** $p < 0.001$. All data are presented as means ± SEM. Investigators were blinded to allocation of groups and outcome assessment for all experiments except for data shown in Figures 4E-4H, 5D-5G and S3A-S3O.

SUPPLEMENTARY DATA

Supplementary data table

Figure 1A, left panel	CTRL: 195.7 ± 9.4 s, n = 30 mice, CMS: 135.6 ± 5.6 s, n = 70 mice; $p < 0.001$, unpaired Student's t-test
Figure 1B, left panel	CTRL: 73.6 ± 2.5%, n = 33 mice; CMS: 63.3 ± 2%, n = 112 mice; $p < 0.01$, unpaired Student's t-test
Figure 1C, left panel	CTRL: 114.5 ± 3.8 s, n = 43 mice, CMS: 89.6 ± 2.4 s, n = 120 mice; $p < 0.001$, unpaired Student's t-test
Figure 1E	EPM: $R^2 = 0.33$, $p < 0.001$, SPT: $R^2 = 0.29$, $p < 0.001$, TST: $R^2 = 0.12$, $p = 0.004$; linear correlation
Figure 1F	EPM: $R^2 = 0.19$, $p < 0.001$, SPT: $R^2 = 0.11$, $p < 0.001$, TST: $R^2 = 0.29$, $p < 0.001$; linear correlation
Figure 2D	+150 pA: $CTRL_{D0-1}$: 38.4 ± 3.9 spikes, n = 37 cells; CMS_{D2-3}: 50.8 ± 4.3 spikes, n = 38 cells; CMS_{D0-1}: 32.3 ± 3.9 spikes, n = 29 cells; $CTRL_{D2-3}$: 43.1 ± 5.8 spikes, n = 28 cells; $CTRL_{D0-1}$ vs. CMS_{D2-3} $p = 0.022$, CMS_{D0-1} vs. CMS_{D2-3} $p = 0.007$, $CTRL_{D2-3}$ vs. CMS_{D2-3} $p = 0.64$, $CTRL_{D2-3}$ vs. $CTRL_{D0-1}$ $p = 0.66$; two-way ANOVA $p = 0.014$, Sidak's post hoc test
Figure 2E	+150 pA: EPM_{CTRL}: neg: 44.6 ± 6 spikes, n = 23 cells, pos: 38.2 ± 4 spikes, n = 42 cells, $p = 0.60$; EPM_{CMS}: neg: 45.8 ± 5.9 spikes, n = 24 cells, pos: 41.1 ± 4.3 spikes, n = 43 cells, $p = 0.76$; two-way ANOVA $p = 0.27$, Sidak's post hoc test;
Figure 2F	+150 pA: SPT_{CTRL}: neg: 38.4 ± 3.9 spikes, n = 37 cells, pos: 43.1 ± 5.8 spikes, n = 28 cells, $p = 0.99$; SPT_{CMS}: neg: 42.47 ± 4.6 spikes, n = 43 cells, pos: 43.5 ± 5 spikes, n = 24 cells, $p = 0.99$; two-way ANOVA $p = 0.57$, Sidak's post hoc test;
Figure 2G	+150 pA: TST_{CTRL}: neg: 35 ± 3.6 spikes, n = 42 cells, pos: 50.5 ± 6.4 spikes, n = 23 cells, $p = 0.052$; TST_{CMS}: neg: 32.3 ± 5.1 spikes, n = 29 cells, pos: 50.8 ± 4.3 spikes, n = 38 cells, $p = 0.011$; two-way ANOVA $p < 0.001$, Sidak's post hoc test
Figure 2K	+150 pA: $CTRL_{D0-1}$: 24.7 ± 5.2 spikes, n = 16 cells; CMS_{D2-3}: 22.8 ± 5.5 spikes, n = 23 cells; $p = 0.81$, unpaired Student's t-test
Figure 2M	Frequency: $CTRL_{D0-1}$: 2.3 ± 0.4 Hz, n = 11 cells; CMS_{D2-3}: 2.8 ± 0.6 Hz, n = 16 cells; $p = 0.5$; Amplitude: $CTRL_{D0-1}$: 33.1 ± 4.1 pA, n = 11 cells; CMS_{D2-3}: 27.8 ± 3.1 pA, n = 16 cells; $p = 0.3$; both unpaired Student's t-test
Figure 3C	$CTRL_{D0-1}$: 0.24 ± 0.01 ms, n = 5 cells; CMS_{D2-3}: 0.25 ± 0.03 ms, n = 5 cells; $p = 0.74$, unpaired Student's t-test
Figure 3F-I	Spikes in bursts: $CTRL_{D0-1}$: 22.5 ± 1.4%, n = 6 cells; CMS_{D2-3}: 27.8 ± 0.9%, n = 6 cells; $p = 0.012$; Spikes per burst: $CTRL_{D0-1}$: 3.5 ± 0.2, n = 6 cells; CMS_{D2-3}: 4.8 ± 0.4, n = 6 cells; $p = 0.016$; Interburst freq.: $CTRL_{D0-1}$: 0.4 ± 0.05 Hz, n = 6 cells; CMS_{D2-3}: 0.8 ± 0.1 Hz, n = 6 cells; $p = 0.004$; Intraburst freq.: $CTRL_{D0-1}$: 161.3 ± 11.9 Hz, n = 6 cells; CMS_{D2-3}: 184.2 ± 22 Hz , n = 6 cells; $p = 0.38$; tonic: $CTRL_{D0-1}$: 4.4 ± 0.6 Hz, n = 6 cells; CMS_{D2-3}: 9.9 ± 1.3 Hz , n = 6 cells; $p = 0.004$; all unpaired Student's t-test
Figure 3J	$CTRL_{D0-1}$: 5.8 ± 0.9 Hz, n = 6 cells; CMS_{D2-3}: 13.8 ± 1.9 Hz, n = 6 cells; $p = 0.003$; unpaired Student's t-test
Figure 4D	EP→LHb→VTA: 13.6 ± 2.9%, EP→LHb→DR: 4.8 ± 0.7%, LH→LHb→VTA: 32 ± 2.5%, LH→LHb→DR: 41.9 ± 2.5%, VTA→LHb→VTA: 6.6 ± 1.6%, VTA→LHb→DR: 13.2 ± 1.4%; VTA: n = 7

	mice, DR n = 6 mice; two-way ANOVA interaction $p < 0.001$; $p < 0.001$ for all three comparisons, Bonferroni post hoc test
Figure 4G	EP: -336.1 ± 81 pA, n = 16/24 cells (67%); VTA: -143.3 ± 18.1 pA, n = 36/45 cells (80%); LH: -907 ± 127.4 pA, n = 14/16 cells (88%); one-way ANOVA $p < 0.001$, LH vs. EP p = 0.03, LH vs. VTA p = 0.009, EP vs. VTA p = 0.77, Tukey's post hoc test
Figure 4H	NMDAR decay time: EP: 36.4 ± 7.8 ms, n = 10 cells; VTA: 16.5 ± 4.9 ms, n = 7 cells; LH: -102.4 ± 35.7 ms, n = 11 cells; one-way ANOVA interaction p = 0.24, EP vs. LH p = 0.03, VTA vs. LH p = 0.009, EP vs. VTA p = 0.77, Tukey's post hoc test
Figure 5A	EP: $CTRL_{D0\text{-}1}$: 0.44 ± 0.04, n = 12 cells; $CMS_{D2\text{-}3}$: 0.26 ± 0.03, n = 13 cells; p = 0.002; VTA: $CTRL_{D0\text{-}1}$: 0.38 ± 0.05, n = 9 cells; $CMS_{D2\text{-}3}$: 0.57 ± 0.05, n = 15 cells; p = 0.028; LH: $CTRL_{D0\text{-}1}$: 0.48 ± 0.03, n = 12 cells; $CMS_{D2\text{-}3}$: 0.43 ± 0.05, n = 9 cells; p = 0.48; all unpaired Student's t-test
Figure 5B	EP: $CTRL_{D0\text{-}1}$: 4.27 ± 0.8, n = 7 cells; $CMS_{D2\text{-}3}$: 10.11 ± 1.6, n = 9 cells; p = 0.009; VTA: $CTRL_{D0\text{-}1}$: 6.8 ± 1.3, n = 11 cells; $CMS_{D2\text{-}3}$: 5.57 ± 0.5, n = 9 cells; p = 0.42; LH: $CTRL_{D0\text{-}1}$: 5.86 ± 1.3, n = 9 cells; $CMS_{D2\text{-}3}$: 8.80 ± 2.3, n = 11 cells; p = 0.31; all unpaired Student's t-test
Figure 5C	CTRL no NASPM: n = 5 cells, $CTRL_{D0\text{-}1}$: n = 5 cells, $CMS_{D2\text{-}3}$: n = 8 cells; $CTRL_{D0\text{-}1}$ vs. $CMS_{D2\text{-}3}$, two-way ANOVA interaction p = 0.047
Figure 5F	DR: 13.7 ± 1.2 ms, n = 10 cells; VTA: 6.1 ± 0.8 ms, n = 18 cells; $p < 0.001$, unpaired Student's t-test
Figure 5G	DR: baseline: 100%, TTX: 2.83 ± 1.5%, TTX+4AP: 0.84 ± 0.6%, n = 7 cells; VTA: baseline: 100%, TTX: 5.4 ± 4.6 %, TTX+4AP: 47.6 ± 11.5%, n = 6 cells; DR_{TTX} vs. $DR_{TTX+4AP}$ p = 0.29, VTA_{TTX} vs. $VTA_{TTX+4AP}$ p = 0.004; both paired Student's test
Figure 6B	EPM: eYFP: 172.4 ± 20.3 s, n = 8 mice, hM3DGq: 193 ± 21.2 s, n = 9 mice, p = 0.5; SPT: eYFP: 60.8 ± 8%, n = 8 mice, hM3DGq: 53.6 ± 9.9%, n = 7 mice, p = 0.58; TST: eYFP: 146.9 ± 7.1 s, n = 9 mice, hM3DGq: 115.1 ± 8.2 s, n = 9 mice, p = 0.01; OFT: eYFP: 3787 ± 266 cm, n = 9 mice, hM3DGq: 3566 ± 274 cm, n = 9 mice, p = 0.57; all unpaired Student's t-test
Figure 6D	EPM: eYFP: 238.7 ± 13.4 s, n = 10 mice, hM4DGi: 192.2 ± 20.3 s, n = 9 mice, p = 0.068; SPT: eYFP: 60.4 ± 8.1%, n = 8 mice, hM4DGi: 71.1 ± 5.4%, n = 8 mice, p = 0.31; TST: eYFP: 73.2 ± 2.9 s, n = 10 mice, hM4DGi: 87.4 ± 5.7 s, n = 9 mice, p = 0.035; OFT: eYFP: 3703 ± 189 cm, n = 10 mice, hM4DGi: 3508 ± 322 cm, n = 9 mice, p = 0.6; all unpaired Student's t-test
Figure 6F	EPM: eYFP: 294.4 ± 17.3 s, n = 7 mice, hM3DGq: 239.1 ± 25.3 s, n = 8 mice, p = 0.1; SPT: eYFP: 64.8 ± 7%, n = 7 mice, hM3DGq: 50.8 ± 11.2%, n = 7 mice, p = 0.31; TST: eYFP: 106.4 ± 5.1 s, n = 7 mice, hM3DGq: 84.4 ± 7 s, n = 8 mice, p = 0.027; OFT: eYFP: 3633 ± 291 cm, n = 7 mice, hM3DGq: 3645 ± 490 cm, n = 8 mice, p = 0.98; all unpaired Student's t-test
Figure 6H	EPM: eYFP: 198.5 ± 14.2 s, n = 9 mice, hM4DGi: 227.4 ± 24.8 s, n = 10 mice, p = 0.34; SPT: eYFP: 59.8 ± 9.5%, n = 8 mice, hM4DGi: 65.8 ± 9.7%, n = 8 mice, p = 0.66; TST: eYFP: 79.9 ± 5.5 s, n = 10 mice, hM4DGi: 107.9 ± 6.4 s, n = 10 mice, p = 0.004; OFT: eYFP: 2400 ± 207 cm, n = 10 mice, hM4DGi: 2665 ± 258 cm, n = 10 mice, p = 0.43; all unpaired Student's t-test
Figure 7B	TST- VTA: 35 ± 3.6 spikes, n = 42 cells; TST+ VTA: 50.7 ± 4 spikes, n = 52 cells; TST- DR: 23.5 ± 4.7 spikes, n = 13 cells; one-way ANOVA, $p < 0.001$, TST- VTA vs. TST+ VTA p = 0.011, TST+ VTA vs. TST- DR p = 0.003, TST- VTA vs. TST- DR p = 0.34, Tukey's post hoc test

Figure 7F	TST- VTA: -53.8 ± 1.2 mV, n = 42 cells; TST+ VTA: -57.1 ± 0.7 mV, n = 53 cells; TST- DR: -59.7 ± 1.5 mV, n = 13 cells; one-way ANOVA, p = 0.003, TST- VTA vs. TST+ VTA, p = 0.026, TST- VTA vs. TST- DR, p = 0.008, TST+ VTA vs. TST- DR p = 0.35, Tukey's post hoc test

Supplementary figures

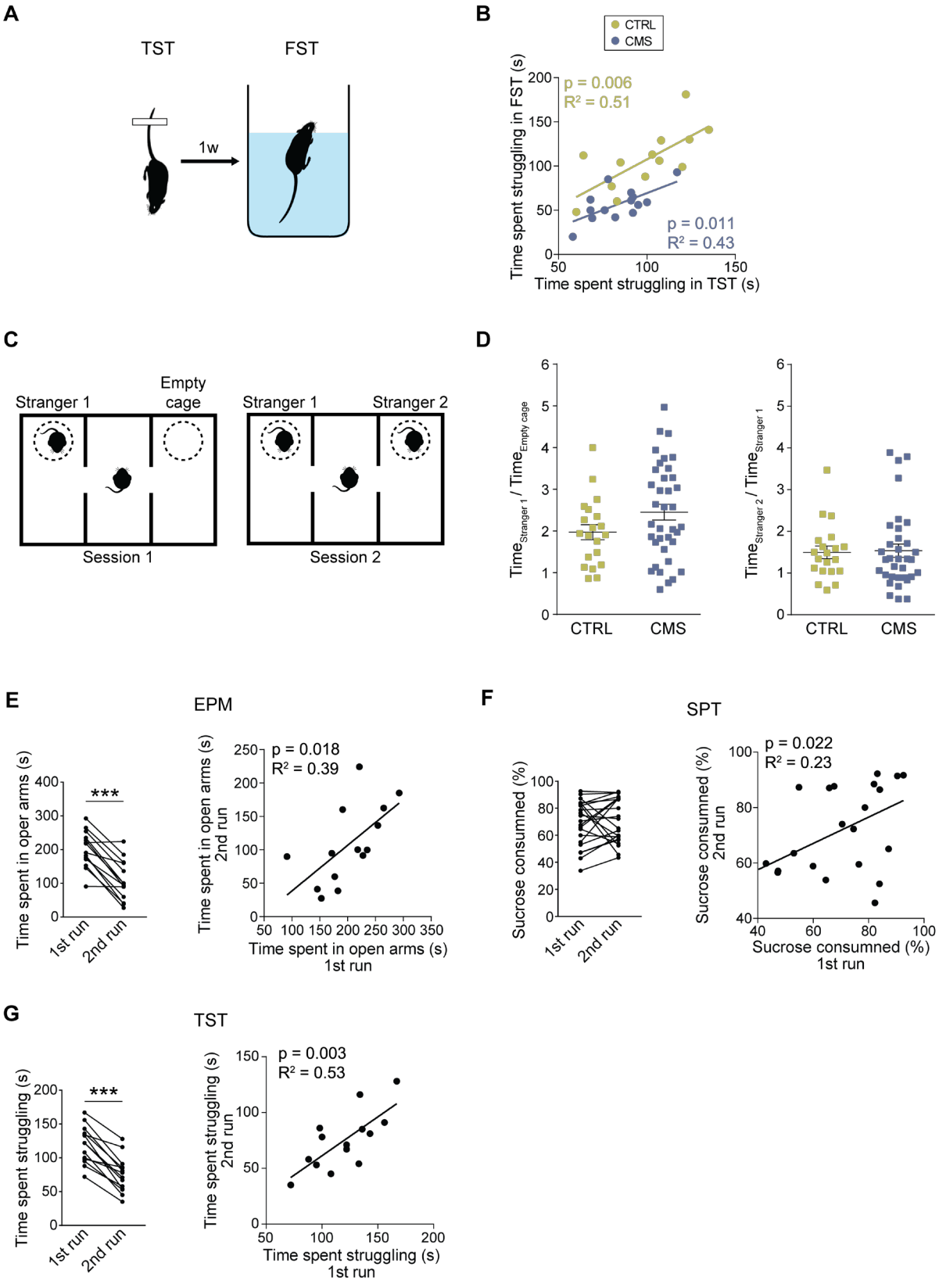

Figure S1. Analysis of chronic stress-induced behavioral phenotypes, Related to Figure 1.
(A) Schematic showing C57BL/6 mice in the tail suspension test (TST) and one week later in the forced swim test (FST).
(B) Correlation of struggling behavior between TST and FST for CTRL (green) and CMS (blue) mice (CTRL: n = 13 mice, $R^2 = 0.51$, $p = 0.006$; CMS: n = 14 mice, $R^2 = 0.43$, $p = 0.011$; linear correlations).
(C) Schematic of experimental design. Session 1 evaluates the social interaction behavior between a subject and an unfamiliar mouse (Stranger 1). Session 2 evaluates the interest of a subject in social novelty by introducing another unfamiliar mouse (Stranger 2).
(D) Graphs showing measures of sociability (left; CTRL: 1.97 ± 0.2, n = 20 mice, CMS: 2.45 ± 0.2, n = 37 mice; $p = 0.1$, unpaired Student's t-test) and social novelty (right; CTRL: 1.5 ± 0.2, n = 20 mice, CMS: 1.54 ± 0.2, n = 37 mice; $p = 0.86$, unpaired Student's t-test) for CTRL and CMS mice (data represent means ± SEM).
(E) Left bar graphs shows time spent in open arms for C57BL/6 mice tested in the elevated plus maze (EPM) for the 1st time (1st run) and then re-tested two weeks later (2nd run) (1st run: 201.8 ± 14.3 s, n = 14 mice; 2nd run: 108.0 ± 15.7 s, n = 14 mice; $p < 0.001$, paired Student's t-test). Right bar graph shows linear correlation between 1st run and 2nd run for time spent in open arms for individual mice (n = 14 mice, $R^2 = 0.39$, $p = 0.018$; linear correlation).
(F) Left bar graphs shows sucrose consumption for C57BL/6 mice tested in the sucrose preference test (SPT) for the 1st time (1st run) and then re-tested two weeks later (2nd run) (1st run: 69.2 ± 3.4 %, n = 23 mice; 2nd run: 71.4 ± 3.4 %, n = 23 mice; $p = 0.53$, paired Student's t-test). Right bar graph shows linear correlation between 1st run and 2nd run for sucrose consumption for individual mice (n = 23 mice, $R^2 = 0.23$, $p = 0.022$; linear correlation).
(G) Left bar graphs shows time spent struggling for C57BL/6 mice tested in TST for the 1st time (1st run) and then re-tested two weeks later (2nd run) (1st run: 119.6 ± 7.3 s, n = 14 mice; 2nd run: 74.9 ± 7.0 s, n = 14 mice; $p < 0.001$, paired Student's t-test). Right bar graph shows linear correlation between 1st run and 2nd run for struggling time for individual mice (n = 14 mice, $R^2 = 0.53$, $p = 0.003$; linear correlation).

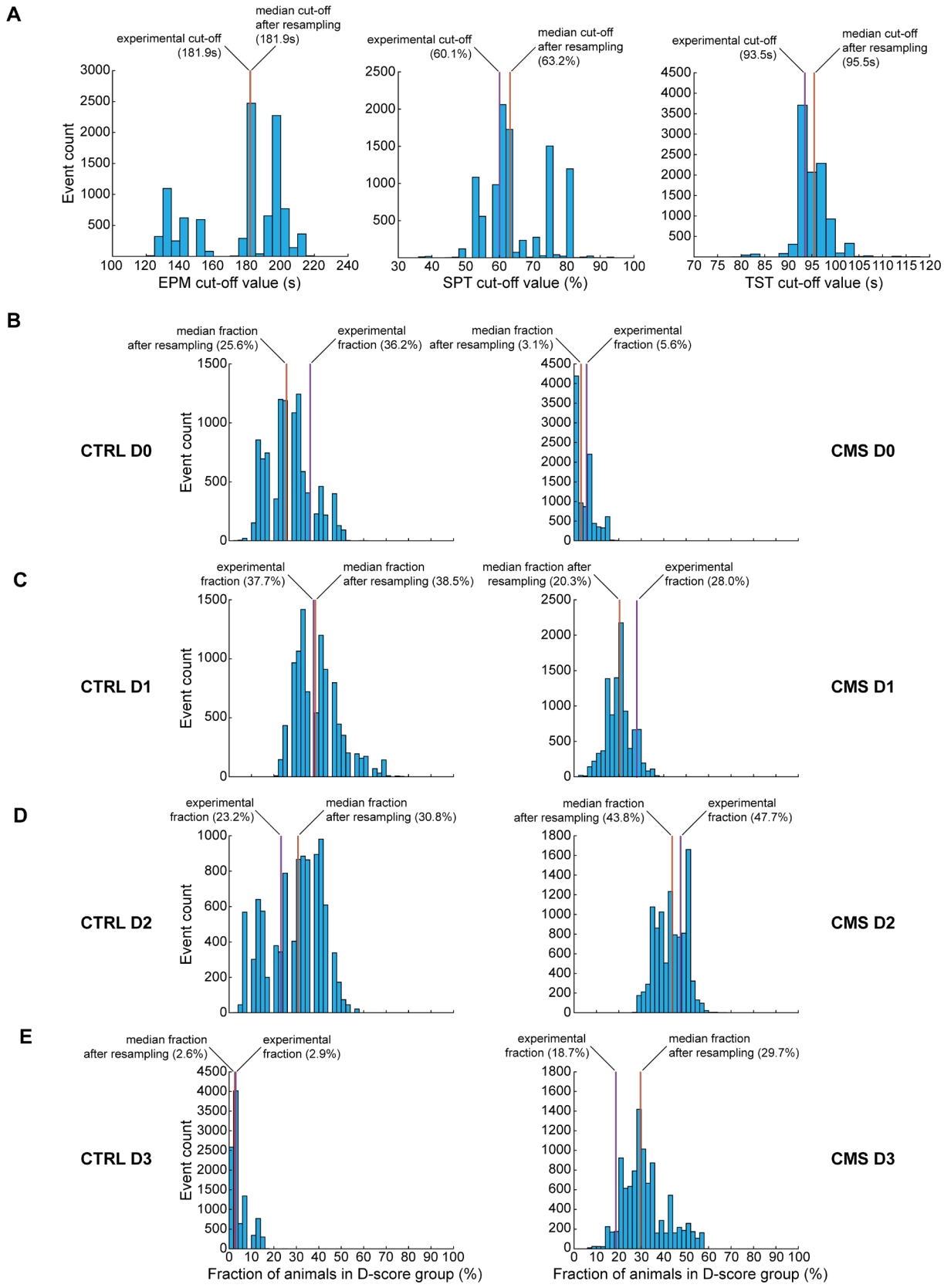
A
experimental cut-off (181.9s)
median cut-off after resampling (181.9s)
Event count
EPM cut-off value (s)
experimental cut-off (60.1%)
median cut-off after resampling (63.2%)
SPT cut-off value (%)
experimental cut-off (93.5s)
median cut-off after resampling (95.5s)
TST cut-off value (s)
B
CTRL D0
median fraction after resampling (25.6%)
experimental fraction (36.2%)
median fraction after resampling (3.1%)
experimental fraction (5.6%)
CMS D0
C
CTRL D1
experimental fraction (37.7%)
median fraction after resampling (38.5%)
median fraction after resampling (20.3%)
experimental fraction (28.0%)
CMS D1
D
CTRL D2
experimental fraction (23.2%)
median fraction after resampling (30.8%)
median fraction after resampling (43.8%)
experimental fraction (47.7%)
CMS D2
E
CTRL D3
median fraction after resampling (2.6%)
experimental fraction (2.9%)
experimental fraction (18.7%)
median fraction after resampling (29.7%)
CMS D3
Fraction of animals in D-score group (%)

Figure S2. Bootstrapping suggests that experimentally-determined cutoff values and D-score subgroups are stable representations, Related to Figure 1.

Based on the large sample sizes used to determine cutoff values in **Figures 1A-1C** (EPM: n = 100 mice; SPT: n = 145 mice; TST = 163 mice), we assumed that these samplings are appropriate representations of real CTRL and CMS distributions for EPM, SPT and TST behavioral tests. First, we sampled with replacement from our experimental data 10,000 times. For example, we drew 43 samples (original experimental sample size) with replacement from TST CTRL group and 120 samples (same reason) from TST CMS group. Then we applied ROC curves to determine a cutoff value from this subsample. Repeating this procedure 10,000 times gave us bootstrapped distributions of cutoff values for anxiety, anhedonia and immobility shown in **Figure S2A**. We observed that our experimentally determined cutoff values were very close to median cutoff values from bootstrapped distributions (EPM: 181.9 s versus 181.9 s; SPT: 60.1% versus 63.2%; TST: 93.5 s versus 95.5 s). Second, we applied our bootstrapped cutoff values to our experimental CTRL and CMS populations from Figures 1E and 1F. For example, we applied one set of bootstrapped EPM, SPT and TST cutoff values to CTRL and CMS mice from Figures 1E and 1F and classified those mice to D-score categories accordingly. After repeating this procedure 10,000 times, we had distributions of D-scores for CTRL and CMS mice (**Figures S2B-S2E**). After comparing our experimentally-determined D-score distributions (**Figures 1G and 1H**) with median bootstrapped D-score distribution values, we again saw close correspondence between the two (CTRL D0: 36.2% versus 25.6%, CTRL D1: 37.7% versus 38.5%, CTRL D2: 23.2% versus 30.8%, CTRL D3: 2.9% versus 2.6%; CMS D0: 5.6% versus 3.1 %, CMS D1: 28.0% versus 20.3%, CMS D2: 47.7% versus 43.8%, CMS D3: 18.7% versus 29.7%).

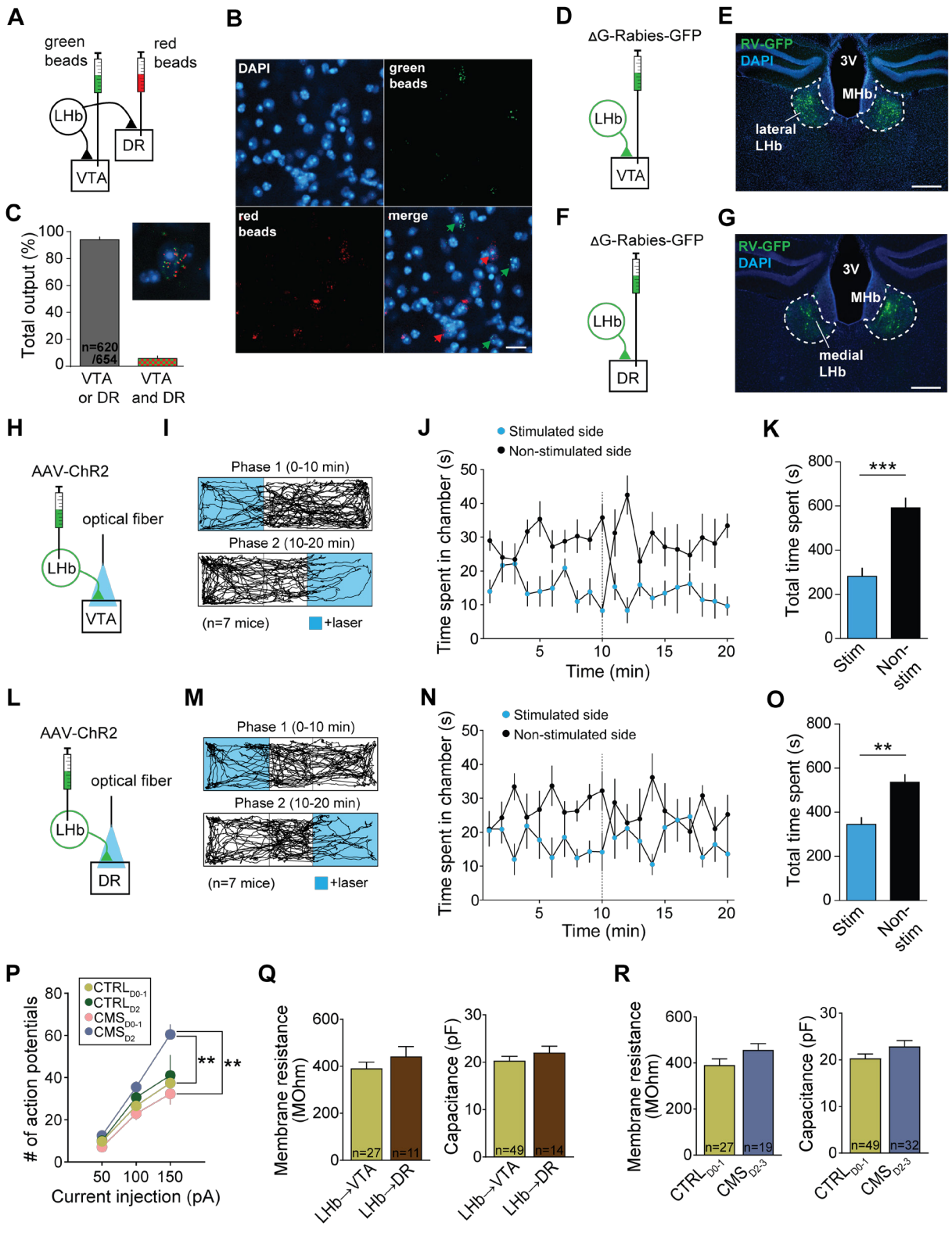

Figure S3. Comparison of LHb→VTA and LHb→DR subpopulations, Related to Figure 2.
(A) Schematic of experimental design showing dual retrograde tracing of LHb→VTA (red beads) and LHb→DR (green beads) subpopulations.

(B) Sample confocal image showing no overlap between retrogradely labeled LHb→VTA (green arrows) and LHb→DR (red arrows) cells in the LHb (DAPI: blue; Scale bar: 20 μm)
(C) Bar graph showing that the majority of retrogradely labeled cells harbor either red or green fluorescent beads and only a small portion of cells contains both red and green beads (VTA or DR: 94.2 ± 1.9 % (620/654 cells), VTA and DR co-labeled: 5.8 ± 1.9 % (34/654 cells), n = 3 mice; data represent means ± SEM). Inset shows sample confocal image of a cell that is co-labeled with red and green beads.
(D) Schematic of experimental design showing retrograde tracing of LHb→VTA neurons by injection of a glycoprotein-deleted rabies virus expressing GFP into the VTA.
(E) Fluorescent image showing retrogradely labeled (RV-GFP, green) LHb→VTA cells in the lateral part of the LHb (DAPI: blue, MHb: medial habenula, 3V: 3rd ventricle; Scale bar: 200 μm).
(F) Schematic of experimental design showing retrograde tracing of LHb→DR neurons by injection of a glycoprotein-deleted rabies virus expressing GFP into the DR.
(G) Fluorescent image showing retrogradely labeled (RV-GFP, green) LHb→DR cells in the medial part of the LHb (DAPI: blue, MHb: medial habenula, 3V: 3rd ventricle; Scale bar: 200 μm).
(H) Schematic of experimental design showing injection of an AAV expressing ChR2 (using CaMKII promoter) into the LHb and optogenetic stimulation of excitatory LHb terminals in the VTA.
(I) Trajectory of a typical animal that received 10 Hz light stimulation of LHb terminals in the VTA in one compartment (Phase 1, blue, top panel) for the initial 10 min period followed by stimulation in the other compartment (Phase 2, blue, lower panel) for an additional 10 min.
(J) Time spent in individual compartments (non-stimulated side: black; stimulated side: blue) plotted as a function of time over the course of the experiment (1 min intervals) for LHb terminal stimulation in the VTA. Dashed line indicates switching of compartment stimulation after 10 min (data represent means ± SEM).
(K) Bar graph showing total time spent in stimulated and non-stimulated compartments for light stimulation of LHb terminals in the VTA (Stim.: 282.2 ± 35.6 s, Non-stim: 592.3 ± 43.8 s, n = 8 mice; *** $p < 0.001$, unpaired Student's t-test, data represent means ± SEM).
(L) Schematic of experimental design showing injection of an AAV expressing ChR2 (using CaMKII promoter) into the LHb and optogenetic stimulation of excitatory LHb terminals in the DR.
(M) Trajectory of a typical animal that received 10 Hz light stimulation of LHb terminals in the DR in one compartment (Phase 1, blue, top panel) for the initial 10 min period followed by stimulation in the other compartment (Phase 2, blue, lower panel) for an additional 10 min.
(N) Time spent in individual compartments (non-stimulated side: black; stimulated side: blue) plotted as a function of time over the course of the experiment (1 min intervals) for LHb terminal stimulation in the DR. Dashed line indicates switching of compartment stimulation after 10 min (data represent means ± SEM).
(O) Bar graph showing total time spent in stimulated and non-stimulated compartments for light stimulation of LHb terminals in the DR (Stim.: 344.9 ± 30.1 s, Non-stim: 536.2 ± 34 s, n = 7 mice; ** $p < 0.01$, unpaired Student's t-test, data represent means ± SEM).
(P) Statistical comparison of evoked firing in LHb→VTA neurons for CMS_{D2} and $CTRL_{D2}$ versus $CTRL_{D0\text{-}1}$ and $CMS_{D0\text{-}1}$ mice. LHb→VTA neurons in CMS_{D2} mice showed significantly increased evoked firing when compared to $CTRL_{D0\text{-}1}$ and $CMS_{D0\text{-}1}$ mice. On average, $CTRL_{D2}$ mice showed higher evoked firing rates compared to $CTRL_{D0\text{-}1}$ mice. However, there was no statistically significant difference for comparison of $CTRL_{D2}$ versus CMS_{D2}, $CMS_{D0\text{-}1}$ or $CTRL_{D0\text{-}1}$ mice. Evoked firing rates in response to +150 pA current injections: $CTRL_{D0\text{-}1}$: 37.4 ± 3.9 spikes, n = 37 cells; CMS_{D2}: 60.5 ± 4.8 spikes, n = 26 cells; $CMS_{D0\text{-}1}$: 32.3 ± 3.9 spikes, n = 29 cells; $CTRL_{D2}$: 41.1 ± 9.7 spikes, n = 14 cells; $CTRL_{D0\text{-}1}$ versus CMS_{D2} $p = 0.006$, $CMS_{D0\text{-}1}$ versus CMS_{D2} $p = 0.001$, $CTRL_{D2}$ versus CMS_{D2} $p = 0.14$, $CTRL_{D2}$ versus $CTRL_{D0}$ $p = 0.97$; one-way ANOVA $p = 0.001$, Tukey's post hoc test.
(Q) Bar graphs showing mean membrane resistances (left) and mean capacitances (right) for LHb→VTA and LHb→DR cells (membrane resistance: LHb→VTA: 391.2 ± 26.7 MOhm, n = 27 cells (11 mice), LHb→DR: 442.2 ± 41.6 MOhm, n = 11 cells (3 mice); $p = 0.31$; membrane capacitance: LHb→VTA:

20.3 ± 0.9 pF, n = 49 cells (11 mice), LHb→DR: 22.1 ± 1.3 pF, n = 14 cells (3 mice); p = 0.36; unpaired Student's t-tests; data represent means ± SEM).
(R) Bar graphs showing mean membrane resistances (left) and mean capacitances (right) in LHb→VTA neurons from $CTRL_{D0\text{-}1}$ and $CMS_{D2\text{-}3}$ mice (membrane resistance: $CTRL_{D0\text{-}1}$: 391.2 ± 26.7 MOhm, n = 27 cells (11 mice), $CMS_{D2\text{-}3}$: 456.8 ± 27.6 MOhm, n = 19 cells (9 mice); p = 0.1; membrane capacitance: $CTRL_{D0\text{-}1}$: 20.3 ± 0.9 pF, n = 49 cells (11 mice), $CMS_{D2\text{-}3}$: 22.9 ± 1.2 pF, n = 32 cells (9 mice); p = 0.09; unpaired Student's t-tests; data represent means ± SEM).

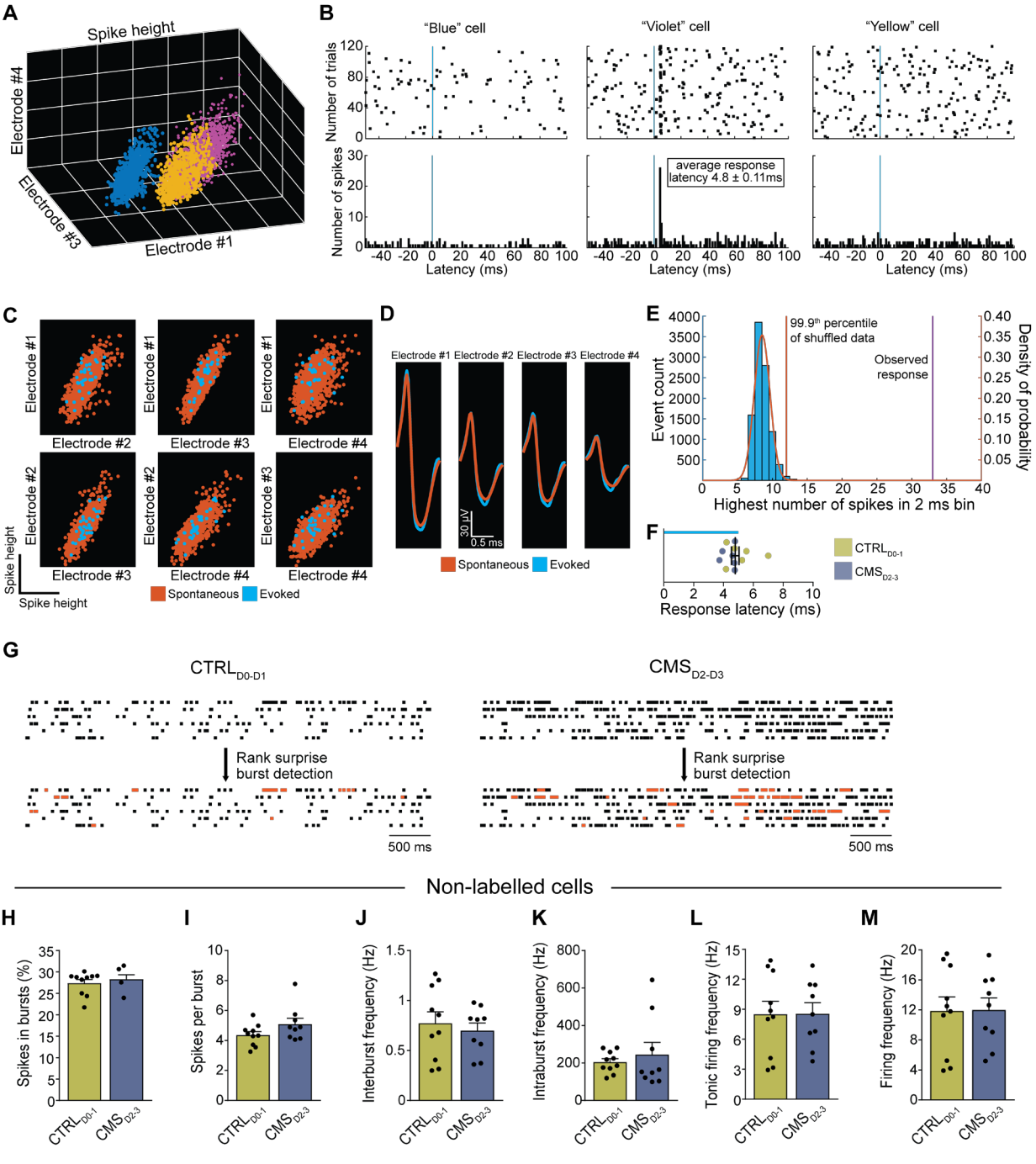

Figure S4. *In vivo* electrophysiology of LHb→VTA neurons, Related to Figure 3.
(A) 3D plot showing samples of three concurrently-recorded units that are plotted according to their action potential height; different colors indicate action potentials that belong to different units.
(B) Top: spike raster plots showing unit firing 50 ms before and 100 ms after the 5 ms laser pulse with each row representing one stimulation trial. The blue line indicates the start of the laser pulse. Bottom: corresponding spike histograms. Cell labeling corresponds to the color scheme in panel A (data represent means ± SEM).
(C) Isolated unit and its spontaneous (orange) and light evoked (blue) action potentials shown across different electrode pairs and plotted according to the action potential height.
(D) Isolated unit and its spontaneous (orange) and light evoked (blue) action potential shapes shown across different electrodes (Scale bar: 30 μV/0.5 ms).
(E) Histogram (blue) showing the distribution (orange) of number of spikes in the most active 2 ms bin for the shuffled data with the 99.9^{th} percentile indicated by an orange vertical line. The number of spikes in the most active 2 ms bin for the observed data is indicated by vertical purple line. See methods for further details.
(F) Graph showing mean response latency to laser stimulation for ChR2-tagged LHb→VTA neurons in $CTRL_{D0\text{-}1}$ (green) and $CMS_{D2\text{-}3}$ (blue) mice (4.79 ± 0.25 ms, n = 12 cells (6 mice); data represent means ± SEM).
(G) Top: spontaneous spike raster plots from $CTRL_{D0\text{-}1}$ (left) and $CMS_{D2\text{-}3}$ (right) mice. Bottom: spikes identified by rank surprise burst detection algorithm that belong to a burst are highlighted in orange (Scale bars: 500 ms).
(H) Mean percentage of spikes in bursts in non-labeled LHb cells from $CTRL_{D0\text{-}1}$ and $CMS_{D2\text{-}3}$ mice ($CTRL_{D0\text{-}1}$: 27.4 ± 0.8 %, n = 10 cells (3 mice), $CMS_{D2\text{-}3}$: 28.3 ± 1 %, n = 9 cells (3 mice); p = 0.5, unpaired Student's t-test; data represent means ± SEM).
(I) Mean number of spikes per burst in non-labeled LHb cells from $CTRL_{D0\text{-}1}$ and $CMS_{D2\text{-}3}$ mice ($CTRL_{D0\text{-}1}$: 4.4 ± 0.2 spikes, n = 10 cells (3 mice), $CMS_{D2\text{-}3}$: 5.1 ± 0.4 spikes, n = 9 cells (3 mice); p = 0.11, unpaired Student's t-test; data represent means ± SEM).
(J) Mean interburst frequencies in non-labeled LHb cells from $CTRL_{D0\text{-}1}$ and $CMS_{D2\text{-}3}$ mice ($CTRL_{D0\text{-}1}$: 0.77 ± 0.1 Hz, n = 10 cells (3 mice), $CMS_{D2\text{-}3}$: 0.7 ± 0.1 Hz, n = 9 cells (3 mice); p = 0.6, unpaired Student's t-test; data represent means ± SEM).
(K) Mean intraburst frequencies in non-labeled LHb cells from $CTRL_{D0\text{-}1}$ and $CMS_{D2\text{-}3}$ mice ($CTRL_{D0\text{-}1}$: 205.3 ± 18.1 Hz, n = 10 cells (3 mice), $CMS_{D2\text{-}3}$: 245 ± 64.8 Hz, n = 9 cells (3 mice); p = 0.54, unpaired Student's t-test; data represent means ± SEM).
(L) Mean tonic firing frequencies in non-labeled LHb cells from $CTRL_{D0\text{-}1}$ and $CMS_{D2\text{-}3}$ mice ($CTRL_{D0\text{-}1}$: 8.5 ± 1.3 Hz, n = 10 cells (3 mice), $CMS_{D2\text{-}3}$: 8.55 ± 1.1 Hz, n = 9 cells (3 mice); p = 0.98, unpaired Student's t-test; data represent means ± SEM).
(M) Mean firing frequencies in non-labeled LHb cells from $CTRL_{D0\text{-}1}$ and $CMS_{D2\text{-}3}$ mice ($CTRL_{D0\text{-}1}$: 11.9 ± 1.9 Hz, n = 10 cells (3 mice), $CMS_{D2\text{-}3}$: 12 ± 1.6 Hz, n = 9 cells (3 mice); p = 0.96, unpaired Student's t-test; data represent means ± SEM).

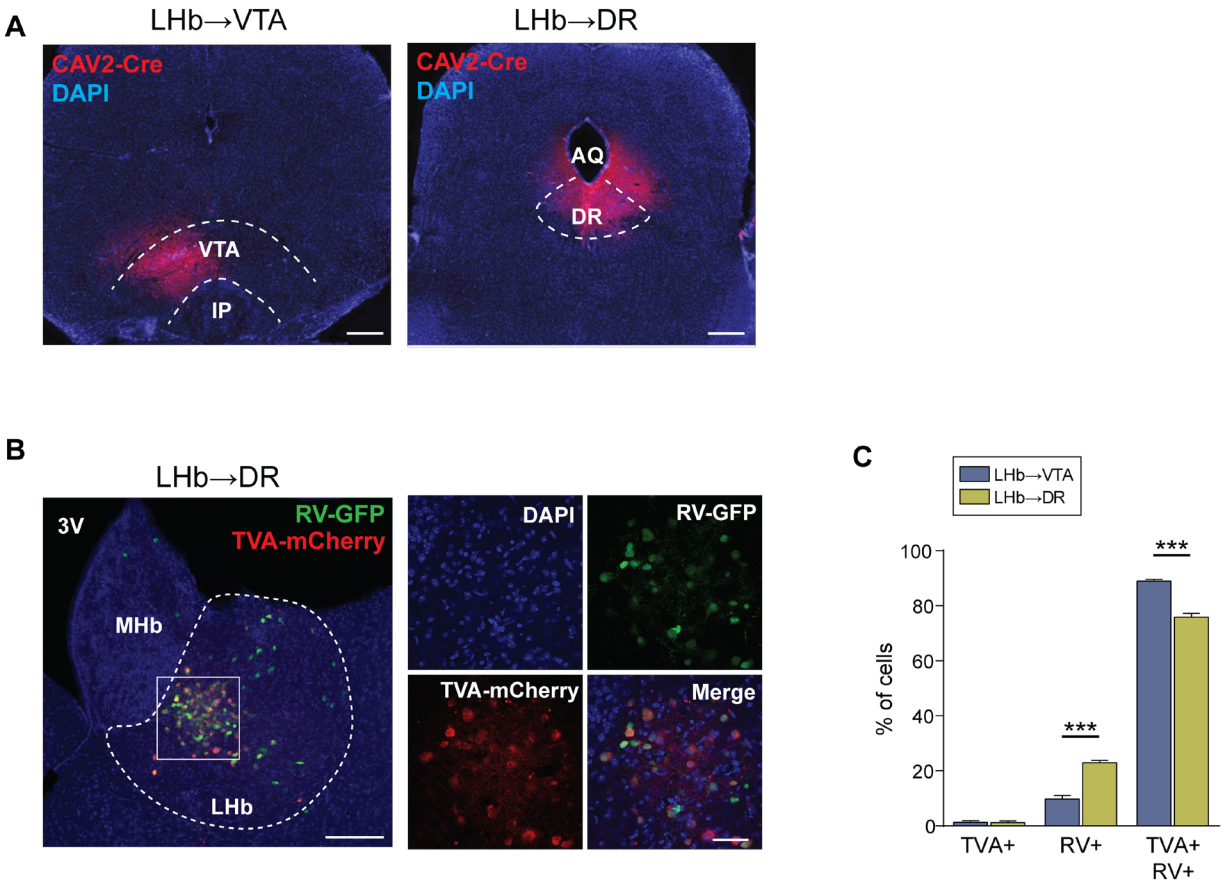

Figure S5. Mapping of monosynaptic inputs to LHb→VTA and LHb→DR neurons, Related to Figure 4.

(A) Representative samples showing injection-site of CAV2-Cre (red) in the VTA (left) or DR (right) (DAPI: blue; IP: interpeduncular nucleus, AQ: cerebral aqueduct; Scale bars: 450 µm).

(B) Left: Confocal image showing the anatomical distribution of starter cells in the LHb for mapping inputs to LHb→DR neurons. Starter cells are defined as cells that co-express RV-GFP (green) and TVA-mCherry (red; Scale bar: 150 µm). Right: Higher magnification confocal image of the region highlighted in the left image (DAPI: blue; Scale bar: 60 µm).

(C) Percentage of the cells that are either TVA-mCherry positive or RV-GFP positive or cells that co-express TVA-mCherry and RV-GFP in the LHb for mapping of inputs to LHb→VTA (blue; n = 2 mice) and LHb→DR (green; n = 2 mice) neurons (TVA-mCherry-positive: LHb→VTA: 1.28 ± 0.4 %, LHb→DR: 1.18 ± 0.4 %, p = 0.99; RV-GFP-positive: LHb→VTA: 9.74 ± 0.9 %, LHb→DR: 22.98 ± 0.6 %, *** $p < 0.001$; TVA-mCherry and RV-GFP co-expression: LHb→VTA: 88.98 ± 0.5 %, LHb→DR TVA+/RV+: 75.84 ± 1 %, *** $p < 0.001$; two-way ANOVA interaction $p < 0.001$, Sidak's post hoc test; data represent means ± SEM).

Abbreviations used in **Figure 4D**: PFC: prefrontral cortex, ACC: anterior cingulate cortex, STR: striatum, EP: entopeduncular nucleus, PALc: caudal pallidum, PALm: medial pallidum, PALv: ventral pallidum, LSX: lateral septal complex, LPO: lateral preoptic area, PVX: paraventricular hypothalamic nucleus, LH: lateral hypothalamus, MEZ: hypothalamic medial zone, other HY: other hypothalamic areas, DORpm: polymodal association cortex related thalamus, other MB: other midbrain, VTA: ventral tegmental area, SN: substantia nigra, MRN: median raphe nucleus, DR: dorsal raphe nucleus, PAG: periaqueductal gray, SC: superior colliculus.

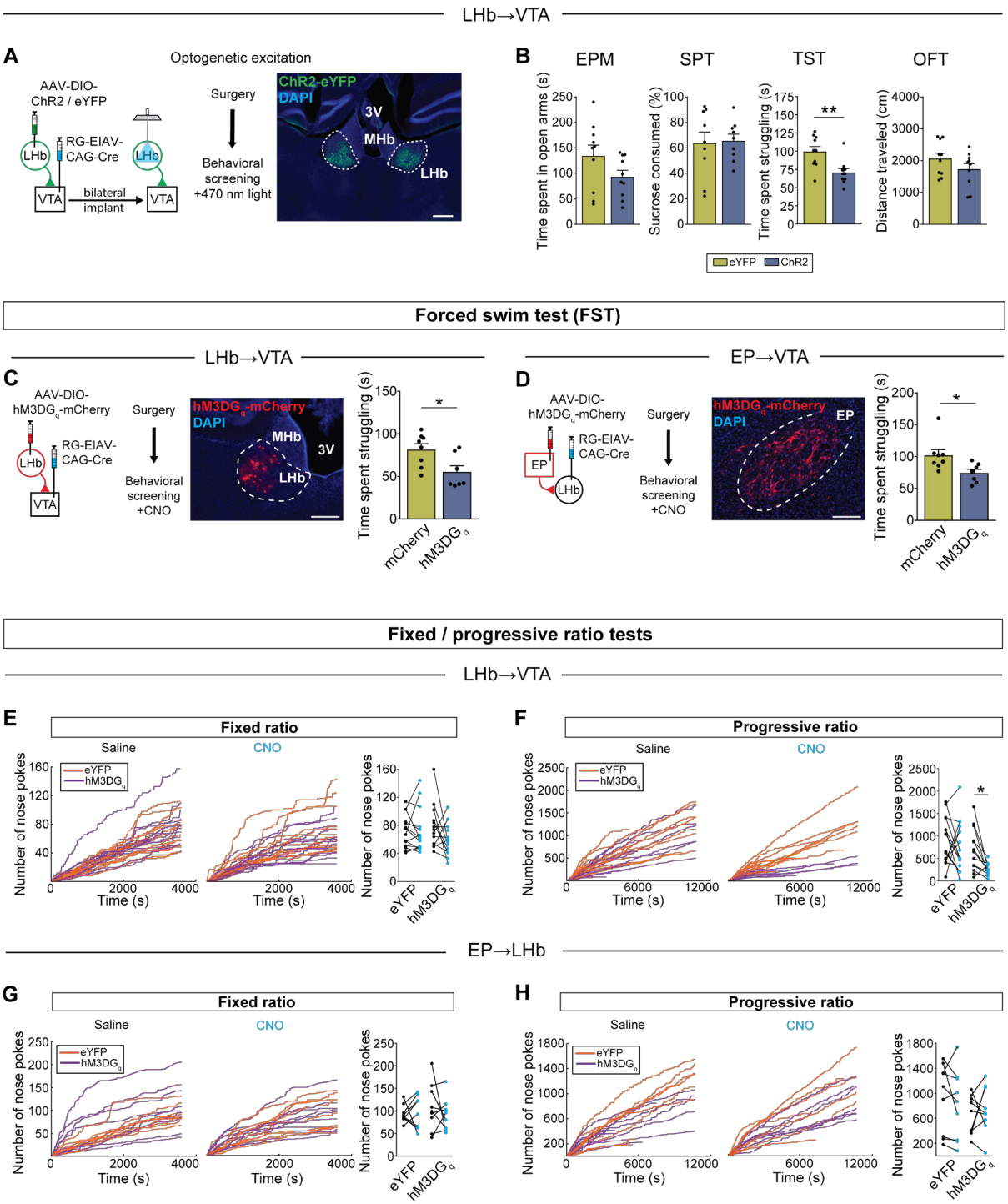

Figure S6. Role of LHb→VTA and EP→LHb neurons in passive coping and effort-related motivated behavior, Related to Figure 6.

(A) Left: Schematic of experimental design showing optogenetic stimulation of LHb→VTA neurons in non-stressed mice. Right: Coronal brain section showing ChR2-eYFP (green) expression in a subset of LHb neurons projecting to VTA (3V: 3rd ventricle, MHb: medial habenula; DAPI: blue; Scale bar: 300 µm).

(B) Bar graphs showing time spent in open arms in EPM, sucrose consumption in SPT, time spent

struggling in TST and total distance travelled in OFT for mice expressing eYFP or ChR2 in LHb→VTA neurons (EPM: eYFP: 134.4 ± 21 s, n = 10 mice, ChR2: 93.4 ± 12.7 s, n = 10 mice, p = 0.11; SPT: eYFP: 63.6 ± 8.9 %, n = 9 mice, ChR2: 65.6 ± 5.2 %, n = 9 mice, p = 0.85; TST: eYFP: 99.5 ± 6.9 s, n = 10 mice, ChR2: 70.7 ± 5.3 s, n = 10 mice, ** p = 0.004; OFT: eYFP: 2063 ± 170.8 cm, n = 10 mice, ChR2: 1731 ± 172 cm, n = 10 mice, p = 0.19; all unpaired Student's t-test; data represent means ± SEM).
(C) Left: Schematic of experimental design showing chemogenetic activation of LHb→VTA neurons in non-stressed mice. Middle: Coronal brain section showing hM3DGq-mCherry (red) expression in a subset of LHb neurons projecting to VTA (DAPI: blue; Scale bar: 200 µm). Right: Bar graphs showing time spent struggling in the forced swim test (FST) after CNO injections for mice expressing eYFP or hM3DGq-mCherry in LHb→VTA neurons (mCherry: 81.5 ± 6.8 s, n = 8 mice; hM3DGq: 55.1 ± 7.4 s, n = 7 mice; p = 0.021, unpaired Student's t-test; data represent means ± SEM).
(D) Left: Schematic of experimental design showing chemogenetic activation of EP→LHb neurons in non-stressed mice. Middle: Coronal brain section showing hM3DGq-mCherry (red) expression in a subset of EP neurons projecting to LHb (DAPI: blue; Scale bar: 200 µm). Right: Bar graphs showing time spent struggling in the FST after CNO injections for mice expressing eYFP or hM3DGq-mCherry in EP→LHb neurons (mCherry: 101.9 ± 9.0 s, n = 8 mice; hM3DGq: 74.3 ± 5.8 s, n = 7 mice; p = 0.026, unpaired Student's t-test; data represent means ± SEM).
(E) Number of nose pokes over time in fixed ratio operant behavior after saline (left) and CNO (middle) injections for mice expressing eYFP or hM3DGq in LHb→VTA neurons. Right: Graph showing total number of nose pokes for saline (black) and CNO (blue) injected eYFP and hM3DGq mice ($eYFP_{saline}$: 71.7 ± 6.3 pokes, $eYFP_{CNO}$: 72.4 ± 8.4 pokes, n = 14 mice, p = 0.94; $hM3DGq_{saline}$: 78.8± 8.8 pokes, $hM3DGq_{CNO}$: 59± 6.3 pokes, n = 13 mice, p = 0.09; two-way RM ANOVA, there was no saline / CNO effect (p = 0.16) and no eYFP / hM3DGq effect (p = 0.72), Holm-Sidak's post hoc test).
(F) Number of nose pokes over time in progressive ratio operant behavior after saline (left) and CNO (middle) injections for mice expressing eYFP or hM3DGq in LHb→VTA neurons. Right: Graph showing total number of nose pokes for saline (black) and CNO (blue) injected eYFP and hM3DGq mice ($eYFP_{saline}$: 912.3 ± 141.4 pokes, $eYFP_{CNO}$: 773.8 ± 153 pokes, n = 14 mice, p = 0.4; $hM3DGq_{saline}$: 686.5 ± 132.8 pokes, $hM3DGq_{CNO}$: 254.8± 37.6 pokes, n = 13 mice, * p = 0.035; two-way RM ANOVA, there was saline / CNO effect (p = 0.023) and eYFP / hM3DGq effect (p = 0.011), Holm-Sidak's post hoc test).
(G) Number of nose pokes over time in fixed ratio operant behavior after saline (left) and CNO (middle) injections in mice expressing eYFP or hM3DGq in EP→LHb neurons. Right: Graph showing total number of nose pokes for saline (black) and CNO (blue) injected eYFP and hM3DGq mice ($eYFP_{saline}$: 93.1 ± 6.4 pokes, $eYFP_{CNO}$: 95 ± 12.1 pokes, n = 9 mice, p = 0.92; $hM3DGq_{saline}$: 109 ± 17.4 pokes, $hM3DGq_{CNO}$: 92.2 ± 11.7 pokes, n = 9 mice, p = 0.58; two-way RM ANOVA, there was no saline / CNO effect (p = 0.56) and no eYFP / hM3DGq effect (p = 0.61), Holm-Sidak's post hoc test).
(H) Number of nose pokes over time in progressive ratio operant behavior after saline (left) and CNO (middle) injections in mice expressing eYFP or hM3DGq in EP→LHb neurons. Right: Bar graph showing total number of nose pokes for saline (black) and CNO (blue) injected eYFP and hM3DGq mice ($eYFP_{saline}$: 937 ± 182.4 pokes, $eYFP_{CNO}$: 815.4 ± 185.4 pokes, n = 9 mice, p = 0.58; $hM3DGq_{saline}$: 655.4 ± 102.8 pokes, $hM3DGq_{CNO}$: 743.3 ± 125.4 pokes, n = 9 mice, p = 0.58; two-way RM ANOVA, there was no saline / CNO effect (p = 0.85) and no eYFP / hM3DGq effect (p = 0.38), Holm-Sidak's post hoc test).

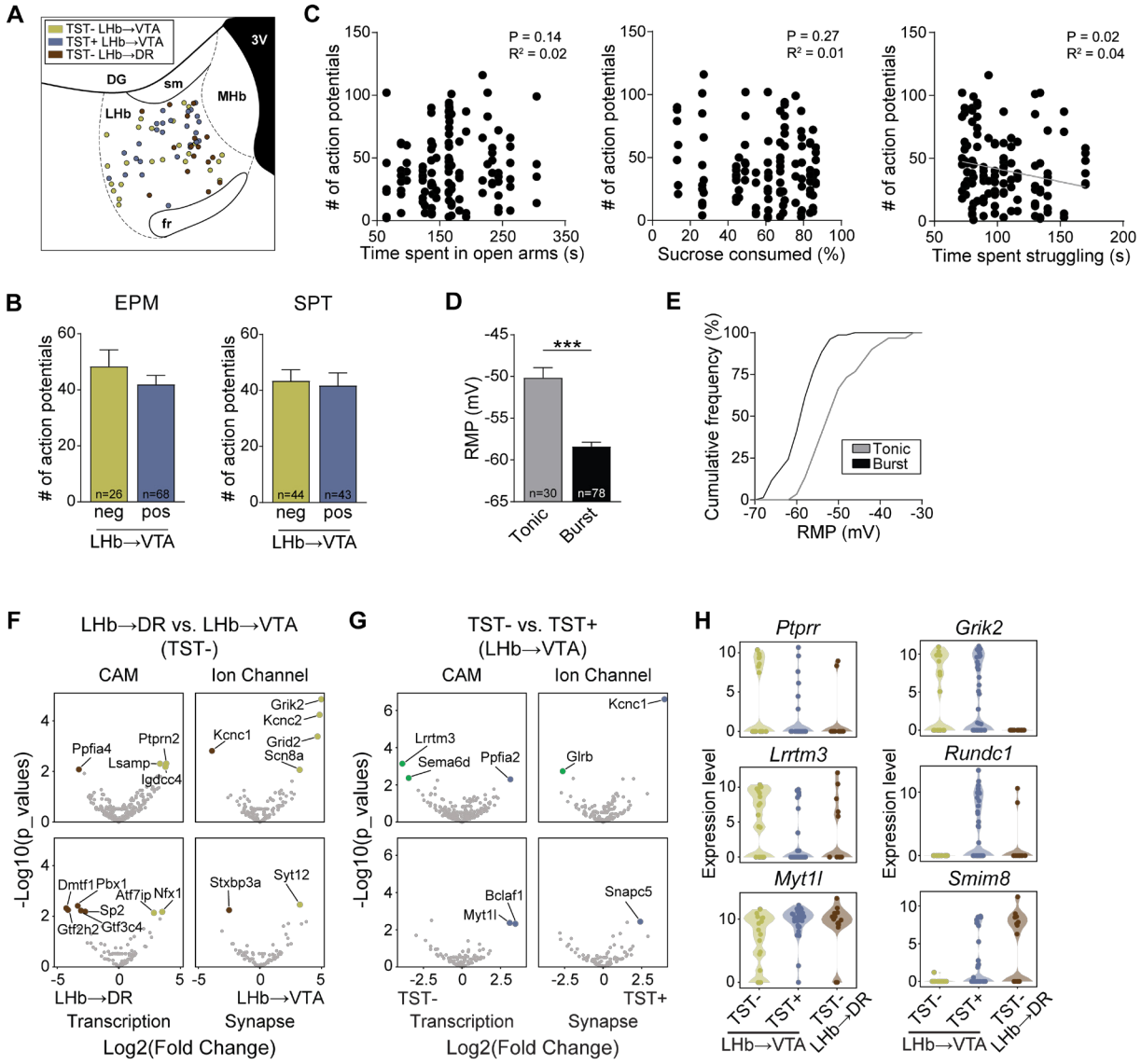

Figure S7. Molecular and physiological correlates of passive coping, Related to Figure 7.
(A) Schematic showing the anatomical location of TST- LHb→VTA (green), TST+ LHb→VTA (blue) and TST- LHb→DR (brown) cells in the LHb (MHb: medial habenula, DG: dentate gyrus, 3V: 3rd ventricle, sm: stria medullaris, fr: fasciculus retroflexus).
(B) Mean number of action potentials in response to injection of a +150 pA depolarizing current in LHb→VTA neurons from mice that were pooled according to whether they were positive or negative for a specific behavioral phenotype (i.e. anxiety assessed in EPM (left), anhedonia assessed in SPT (right)). Animals were considered positive if they scored below the corresponding cutoff value defined in **Figures 1A-1C** (EPM: neg: 48.4 ± 5.9 spikes, n = 26 cells (5 mice), pos: 41.9 ± 3.2 spikes, n = 68 cells (11 mice), p = 0.32; SPT: neg: 43.4 ± 4 spikes, n = 44 cells (6 mice), pos: 41.8 ± 4.5 spikes, n = 43 cells (10 mice), p = 0.78; all unpaired Student's t-test).
(C) Graphs showing evoked number of action potentials in response to injection of a +150 pA depolarizing ramp current in LHb→VTA neurons and their correlation with time spent in open arms in EPM (left), sucrose consumed in SPT (middle) and time spent struggling in TST (right; EPM: $R^2 = 0.02$, p = 0.14, SPT: $R^2 = 0.27$, p = 0.01, TST: $R^2 = 0.02$, p = 0.04).

(D) Mean resting membrane potential recorded from cells that predominantly fire tonically or in bursts (Tonic: -50.1 ± 1.2 mV, n = 30 cells (14 mice), burst: -58.4 ± 0.5 mV, n = 78 cells (17 mice); *** $p < 0.001$, unpaired Student's t-test; data represent means ± SEM).
(E) Cumulative frequency of resting membrane potential recorded from cells that predominantly fire tonically (grey) or in bursts (black).
(F) Volcano plots show differential gene expression between single LHb→VTA (n = 16 cells, 5 mice) and LHb→DR neurons (n = 14 cells, 5 mice) in TST- mice. Gold and brown data points denote genes that are significantly enriched in TST- LHb→VTA versus TST- LHb→DR neurons, respectively. Highlighted are the cell adhesion molecule-coding (CAM; top left), ion channel-coding (top right), transcription factor-coding (bottom left) and synapse-related (bottom right) genes. Gray data points represent genes that are not significantly enriched in either category (i.e. absolute value of Log2(Fold Change) < 2 and $p < 0.01$).
(G) Volcano plots show differential gene expression between single LHb→VTA neurons in TST- (n = 16 cells, 5 mice) versus TST+ (n = 37 cells, 10 mice) mice. Green and blue data points denote genes that are significantly enriched in cells from TST- versus TST+ mice, respectively. Highlighted are the cell adhesion molecule-coding (CAM; top left), ion channel-coding (top right), transcription factor-coding (bottom left) and synapse-related (bottom right) genes. Gray data points represent genes that are not significantly enriched in either category (i.e. absolute value of Log2(Fold Change) < 2 and $p < 0.01$).
(H) Violin plots show expression of *Ptprr* (top left), *Grik2* (top right), *Lrrtm3* (middle left), *Rundc1* (middle right), *Myt1l* (bottom left) and *Smim8* (bottom right) as examples from TST- (n = 16 cells, 5 mice) and TST+ LHb→VTA (n = 37 cells, 10 mice) and TST- LHb→DR (n = 14 cells, 5 mice) mice.

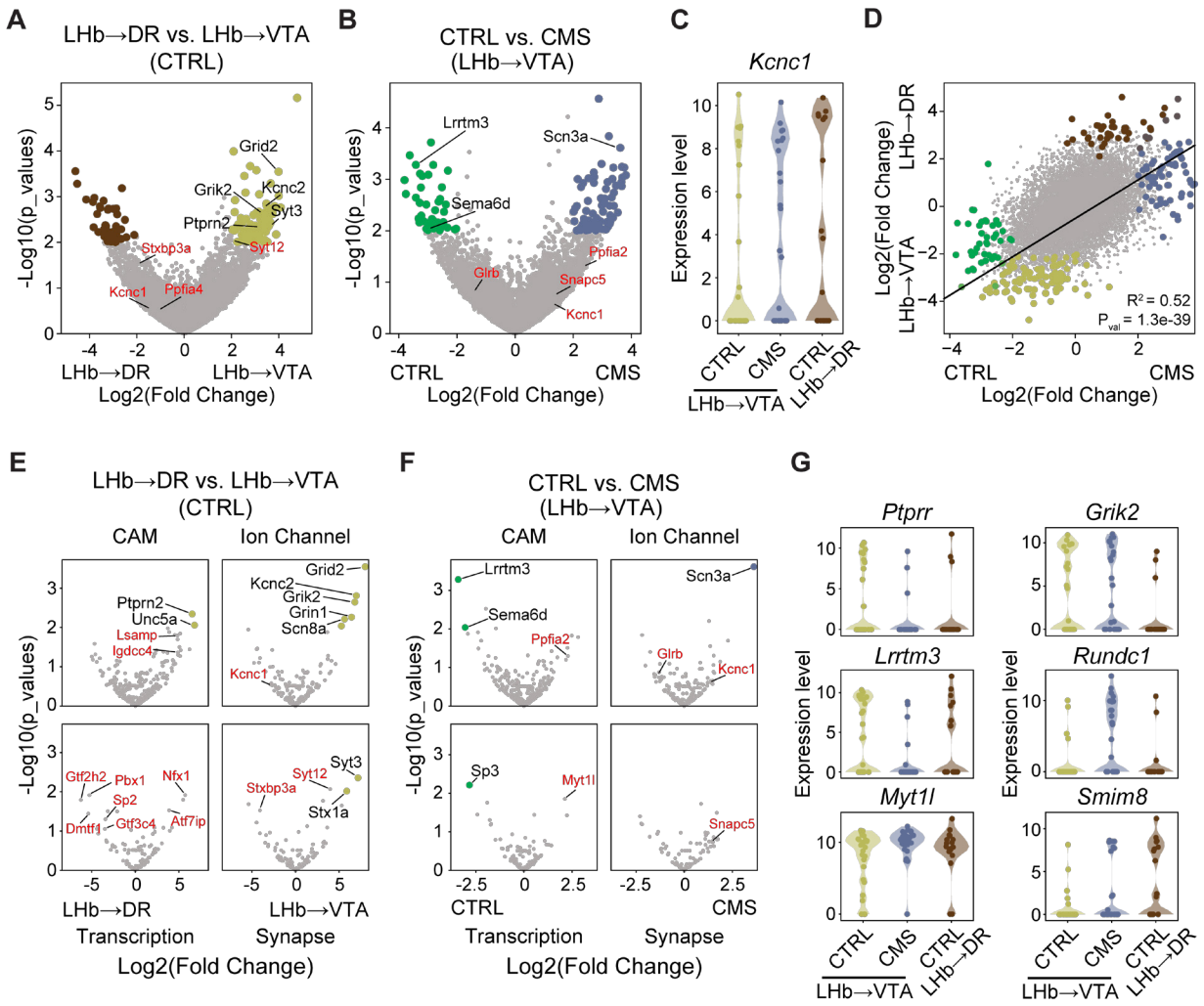

Figure S8. Single-cell transcriptomic analysis for comparison of CTRL and CMS mice, Related to Figure 7.

(A) Volcano plots displaying differential gene expression between single LHb→VTA (n = 26 cells, 9 mice) and LHb→DR (n = 18 cells, 6 mice) neurons in CTRL mice. Gold and brown data points denote genes that are significantly enriched in LHb→VTA versus LHb→DR neurons from CTRL mice, respectively. Highlighted in black are the ion channel-coding and synapse-related genes. Highlighted in red are the genes that are detected as significantly differently expressed in LHb→VTA versus LHb→DR neurons from TST- but not from CTRL mice (see **Figure 7**). Gray data points represent genes that are not significantly enriched in either category (i.e. absolute value of Log2(Fold Change) < 2 and p < 0.01).

(B) Violin plot displaying differential gene expression between single LHb→VTA neurons in CTRL (n = 26 cells, 9 mice) versus CMS (n = 27 cells, 6 mice) mice. Green and blue data points denote genes that are significantly enriched in cells from CTRL versus CMS mice, respectively. Highlighted in black are the ion channel-coding and synapse-related genes. Highlighted in red are the genes that are detected as significantly differently expressed in LHb→VTA versus LHb→DR neurons from TST- but not from CTRL mice (see **Figure 7**). Gray data points represent genes that are not significantly enriched in either category (i.e. absolute value of Log2(Fold Change) < 2 and p < 0.01).

(C) Violin plots show *Kcnc1* gene expression in single-cells from CTRL compared to CMS mice. *Kcnc1* is also significantly higher expressed in TST- LHb→DR versus TST- LHb→VTA neurons (see **Figure 7J**), but not different between CTRL LHb→DR versus CTRL LHb→VTA neurons, highlighting that

experienced-based classification (CTRL versus CMS) masks transcriptomic correlates of phenotype-based classification (TST- versus TST+) in studying depression.
(D) Regression analysis of differential gene expression between CTRL LHb→VTA (n = 26 cells, 9 mice) versus CMS LHb→VTA (n = 27 cells, 6 mice) neurons and between CTRL LHb→DR (n = 27 cells, 6 mice) versus CTRL LHb→VTA (n = 26 cells, 9 mice) neurons. For each gene, data points represent Log2 (Fold Change) values in both comparisons; colored data points highlight the same genes as identified in panels (A) and (B). This analysis based on experience-based classification revealed less stringent regression and lower statistical significance compared to that based on phenotypic classification (see **Figure 7K**).
(E) Volcano plots show differential gene expression between single LHb→VTA (n = 26 cells, 9 mice) and LHb→DR neurons (n = 18 cells, 6 mice) in CTRL mice. Gold and brown data points denote genes that are significantly enriched in CTRL LHb→VTA versus CTRL LHb→DR neurons, respectively. Highlighted in black are the cell adhesion molecule-coding (CAM; top left), ion channel-coding (top right), transcription factor-coding (bottom left) and synapse-related (bottom right) genes. Highlighted in red are the genes that are detected as significantly differently expressed in LHb→VTA versus LHb→DR neurons from TST- but not from CTRL mice (see **Figures 7H and S7F**). Gray data points represent genes that are not significantly enriched in either category (i.e. absolute value of Log2(Fold Change) < 2 and $p < 0.01$).
(F) Volcano plots show differential gene expression between single LHb→VTA neurons in CTRL (n = 26 cells, 9 mice) versus CMS (n = 27 cells, 6 mice) mice. Green and blue data points denote genes that are significantly enriched in cells from CTRL versus CMS mice, respectively. Highlighted are the cell adhesion molecule-coding (CAM; top left), ion channel-coding (top right), transcription factor-coding (bottom left) and synapse-related (bottom right) genes. Highlighted in red are the genes that are detected as significantly differently expressed in LHb→VTA versus LHb→DR neurons from TST- but not from CTRL mice (see **Figures 7I and S7G**). Gray data points represent genes that are not significantly enriched in either category (i.e. absolute value of Log2(Fold Change) < 2 and $p < 0.01$).
(G) Violin plots show expression of *Ptprr* (top left), *Grik2* (top right), *Lrrtm3* (middle left), *Rundc1* (middle right), Myt1l (bottom left) and *Smim8* (bottom right) as examples from CTRL (n = 26 cells, 9 mice) and CMS LHb→VTA (n = 27 cells, 6 mice) and CTRL LHb→DR (n = 18 cells, 6 mice) mice.

CHAPTER 3: DISCUSSION

The work described above delineates a distinct habenula subcircuit, namely EP→LHb→VTA, which modulates a specific depression-related behavior. We established an animal model of depression which enables individual behavioral phenotyping of each subject. Using this approach we identified that only LHb→VTA subpopulation becomes hyperactive, whereas LHb→DR subcircuit remains unaffected by exposure to chronic mild stress. Moreover, we were able to associate this aberrant LHb→VTA neuronal activity specifically with passive coping behavioral phenotype, but not with anhedonic or anxious behavioral states. By combing whole brain input tracing and slice electrophysiology, we showed that one of the major inputs to LHb, EP, undergoes synaptic adaptations in our model of depression that might contribute to LHb→VTA hyperactivity. Chemogenetic activation and inhibition of EP→LHb→VTA neuronal pathway were able to increase or ameliorate behavioral despair. Lastly, using single cell RNA-sequencing we were able to identify potential gene targets associated with increased LHb→VTA activity in mice with passive coping phenotype. Even though this study provide a set of biological markers at the level of genes, synapses, cells, and circuits that define a distinctive behavioral phenotype, it also raises additional questions and opens new possible venues of investigation.

We chose chronic mild stress (CMS) as our animal model of depression, where mice are exposed to two unpredictable stressors per day, one during the light phase and one during the dark phase. CMS has been chosen as our model because chronic stress is a major risk factor for the development of depression in humans (Hill et al., 2012; Mazure and Maciejewski, 2003; Willner et al., 2013). Moreover, the model has good predictive validity (behavioral changes are reversed by chronic, but not acute, treatment with a wide variety of antidepressants), face validity (exposure to CMS promotes behavioral and physiological changes that are observed in major depression disorder), and construct validity (CMS causes a generalized decrease in responsiveness to rewards, comparable to anhedonia, the core symptom of major depressive disorder; Willner, 1997). After 8 weeks of CMS, we tested for anxiety, using elevated plus maze, anhedonia, using sucrose preference test, passive coping / despair phenotype, using tail suspension test, and social withdrawal, suing social interaction test. After re-testing mice on the same behavioral assays under the same experimental conditions 2 weeks after they performed the test for the first time, we observed a linear correlation between the first and second test in all three behavioral assays, suggesting that animals exhibit persistent behavioral phenotypes that do not change over time (**Figure S1E-G**). This suggests that depression-like phenotypes induced by stress exposure are not just stochastic variability and represent robust behavioral phenotypes that persevere over time, indicating persistent neuronal changes underlying the behavioral adaptations.

Even though we tested for depression-like behaviors that are most commonly checked in the field, that also imposes some limitations for our study. We forego other depression-like behaviors and phenotypes that also observable in animals models of depression, such as psychomotor retardation, body weight gain or loss, sleep disturbances, stress hormone level changes in blood plasma, etc. That biases our study towards the behaviors we tested, meaning that we can associate LHb hyperactivity only with behaviors we tested for but we cannot be sure that LHb does not play a role in stress induced phenotypes we have not tested. Moreover, we observed

that CMS did not induce social deficits that are induced using other animal models of depression, for example social defeat stress (**Figure 1SC and 1SD**; Krishnan et al., 2007). This presents an interesting dilemma that different depression models affect different neural circuits or could possibly lead to different circuit adaptions in the same brain structures. That would mean that by choosing CMS as our animal model of depression, we biased our study to certain phenotypic changes in the LHb that might not be observable if the animals would have been exposed to, for example, social defeat stress. Lastly, behavioral results from our sucrose preference test showed high variability, as evident by low true positive rate (~40%) for our cut-off value for the test we established using receiver operatic characteristic curves (**Figure 1B**). Most likely this high variability was due to the way we performed our sucrose preference test, i.e. counting the number of licks from water and sucrose bottles over the period of 1.5 hours. That introduces variability because mice are not trained prior to behavioral testing and sucrose preference values obtained might not necessarily reflect true hedonic phenotype but instead represent stochastic variability. We chose this approach so we would be able to carry out optogenetic and chemogenetic manipulations, which are only feasible over a short time frame. Nonetheless, this high variability could probably be resolved by measuring sucrose preference over the period of 12 hours instead of 1.5 hours, however, that would make functional circuit manipulations overtly complicated.

Using the aforementioned stress model, we employed slice electrophysiology to investigate neuronal adaptions in LHb subcircuits, namely LHb→VTA and LHb→DR. Even though we observed that optogenetic stimulation of these LHb subpopulations induced behavioral aversion (**Figure S3H-O**), we were surprised to see that exposure to chronic mild stress led to hyperexcitability of LHb→VTA but not LHb→DR population, as evident by depolarizing current injections (**Figure 2A-D, 2H-K**). Our findings of LHb→VTA hyperexcitability are consistent with previously published work (Lecca et al., 2016; Tchenio et al., 2017), albeit these two studies recorded from all LHb neurons, not discriminating them based on their projection targets. It is important to mention, that this LHb hyperexcitability is observable in three different animal models of depression (chronic mild stress, repeated foot shock exposure, and maternal separation), suggesting that increased excitability in LHb in depression is a robust electrophysiological phenotype. Moreover, we also detected increased mEPSCs frequency, which is a proxy of increased excitatory synaptic drive, onto LHb→VTA neurons (data not shown), but not LHb→DR neurons (**Figure 2L and 2M**). Such presynaptic adaption in LHb→VTA subpopulation were also previously reported in congenitally helpless rats (Li et al., 2011), which shows that phenotype might be present across different animal species. Notwithstanding that we recorded from retrogradely labelled LHb cells projecting to VTA, we cannot be certain if these LHb cells target dopamine or GABAergic cells in the VTA itself or GABAergic neuronal population in the tail of the VTA, also known as RMTg. This is due to the spread of retrograde tracer, which most likely is taken up by LHb axonal terminals in the VTA and RMTg. Therefore, the actual effects of LHb→VTA hyperexcitability are difficult to interpret as it might lead to either increased or decreased dopamine neuron firing in the VTA, depending on if these LHb neurons target dopamine neurons directly or through feedforward inhibition, respectively. Furthermore, it has been previously demonstrated that RMTg also sends projections to DR, meaning that LHb is capable of serotonin neuron inhibition in DR through disynaptic mechanism (Sego et al., 2013). Consequently, lack of excitability we observed in LHb→DR subpopulation only means that there

is not direct effect on serotonergic neurons in DR, while indirect influence is still probable through LHb→RMTg→DR pathway.

To further investigate LHb→VTA neuronal firing in mice exposed to chronic mild stress, we performed *in vivo* electrophysiology recordings from optogenetically tagged LHb→VTA cells. In agreement with our *in vitro* electrophysiology results, we observed increase both in tonic and burst firing in LHb→VTA cells in stressed mice while they were freely exploring their home cage. Similar results were published by Yang et al.; however, they reported only increase in burst, but not tonic, firing and proposed that burst firing alone in LHb drives aversive behaviors (Yang et al., 2018). We find such findings hard to explain, as we (**Figure S3H, S6A**) and numerous other investigators (Li et al., 2011, Lammel et al., 2012; Stamatakis and Stuber, 2012) were able to induce aversive behaviors by increasing tonic firing in the LHb or its axon terminals. One possible explanation might be that Yang et al. used ISI-threshold burst detection method. In the ISI-threshold method, researchers have to define an ISI threshold for burst initiation and burst termination. The latter parameter is particularly problematic as it heavily depends on the firing rate of a cell. A common ISI threshold for burst termination is 100 ms (Yang et al., 2018b). This means that the ISI interval between the last two spikes in the burst can be up to 100 ms. If this threshold is applied to cells with mixed tonic and burst firing and these cells fire above 10 Hz (mean firing rate of LHb→VTA cells in $CMS_{D2\text{-}3}$ group: 13.8 ± 1.9 Hz), it results in many false positive additions of spikes to bursts. By chance, a cell that fires at 10 Hz may have many ISI intervals <100 ms, meaning that a lot of tonic spikes would be added to the end of identified bursts.

We argued that differences in LHb→VTA and LHb→DR excitabilities after chronic stress exposure might be explained by different synaptic drives onto these subpopulations, as LHb→VTA neurons showed increased mEPSCs frequency (data not shown), whereas LHb→DR cells (**Figure 2L and 2M**) lacked the aforementioned phenotype. After mapping whole brain monosynaptic inputs to these populations, we observed that LHb→VTA neurons received strongest inputs from EP, LH, and VTA itself. Interestingly, the only significant differences in anatomical input strength to LHb→DR subpopulation were only at the aforementioned inputs. Because of that, and because it has been previously demonstrated that stimulation of EP (Shabel et al., 2012), VTA (Root et al., 2014), and LH (Stamatakis et al., 2016) terminals in the LHb promotes aversive behavioral phenotypes, we decided to further investigate synaptic adaptations of these inputs in mice with depression-like phenotype. Functional analysis of input strength (**Figure 4G**) corresponded with our anatomical tracing results (**Figure 4D**), i.e. percentage of total inputs correlated with evoked EPSC size and response rate from these distinct inputs.

Using slice electrophysiology recordings, we compared synaptic properties of EP, VTA, and LH inputs between wild type and stressed mice. Presynaptically, we observed increased synaptic release probability at EP synapse onto LHb→VTA cells (**Figure 5A**), indicating stronger synaptic drive from EP. This presynaptic potentiation might explain increased mEPSCs frequency onto LHb→VTA neurons observed by us (data not shown) and others (Li et al., 2011). Interestingly, we also observed decreased release probability at VTA synapse onto LHb→VTA cells (**Figure 5A**). This suggests an interesting feedback loop, where increased LHb→VTA neuronal activity drives persistent dampening of VTA activity, which in turn leads to

depotentiation and reduced excitatory drive of LHb neurons from VTA. However, caution should be taken while interpreting these results, as the paired pulses used to evaluate release probability at these inputs were evoked using ChR2, which, once activated, is permeable to Ca^{2+} ions, strong regulators of vesicle release (Südhof, 2012) and therefore could confound paired pulse ratio results. Postsynaptically, we saw an increase in AMPAR rectification again only at EP synapse onto LHb→VTA neurons. This increase was mediated by higher insertion of GluR2-lacking AMPAR subunits (**Figure 5B and 5C**). Our findings are in agreement with the results from Li et al. study, which showed that upregulation of βCaMKII in the LHb in wild type mice leads to higher insertion GluR2-lacking AMPARs into synapses, which in turn promotes depression-related behaviors in mice (Li et al., 2013). Increased insertion of GluR2-lacking AMPAR subunits is of significant importance, as such AMPAR become more permeable to Ca^{2+}, which is a potent signaling molecule with numerous end-point effects (Clapham, 2012). Moreover, expression of these AMPARs leads to an increase of mEPSCs frequency (Groth et al., 2010), which presumably could promote stronger excitatory output of LHb neurons. We argue that these synaptic adaptations at EP synapse might drive neural activity in LHb→VTA neurons in animals with depression-lie phenotype. The LHb→DR subpopulation might be spared by these circuit adaptions as it receives significantly weaker monosynaptic input from the EP as demonstrated by our slice electrophysiology recordings (**Figure 5D-G**) and monosynaptic rabies tracing results (**Figure 4A-D**). The aforementioned results together with starter cell analysis of rabies tracing experiment (**Figure S5B and S5C**) highlighted a strong local LHb input map onto LHb→DR subcircuit, whose function and significance remains to be investigated.

Synaptic potentiation of EP inputs to LHb after chronic stress exposure complements previously published findings relating to EP→LHb pathway's role in aversive information processing. First of all, EP axon terminals in the LHb are positioned to target specifically LHb neurons that project to RMTg (Quina et al., 2014). Therefore, increased excitatory synaptic drive from EP is likely lead to inhibition of dopamine and serotonin release from VTA and DR, respectively, through RMTg mediated disynaptic inhibition (Jhou et al., 2009; Kaufling et al, 2009; Sego et al., 2013). Second, research from Sabatini's laboratory identified a unique population of EP neurons that are somatostatin (Sst) and parvalbumin (Pvalb) positive and project exclusively to the LHb. This population of EP neurons receive input biased toward limbic-associated regions of striatum (patches), suggesting that these EP→LHb neurons are relevant to emotional processing, which is in contrast to classical solely-motor function previously assigned to basal ganglia output nuclei (Wallace et al., 2016). Third, habenula-projecting EP neurons are essential for evaluating action outcomes and are regulated by a specific set of inputs from the basal ganglia. Stephenson et al. showed that in a classical conditioning task individual EP→LHb neurons bidirectionally encode whether an outcome is better or worse than expected. Mimicking these evaluation signals with optogenetic inhibition or excitation was sufficient to reinforce or discourage actions in a decision-making task. This suggests that an increase in EP→LHb subpopulation activity when an outcome is worse than expected increases the excitatory drive onto the LHb to inhibit dopamine neurons in VTA and discourage actions. Similarly, decrease in the activity of the EP→LHb pathway when an outcome is better than expected, removes the tonic excitation of the LHb to increase dopaminergic activity and reinforce actions (Stephenson et al., 2016). These studies propose that potentiation and hyperactivity of EP→LHb pathway in

depression might predispose patients towards negative emotional processing, in which neutral or positive situations would be processed more negatively.

The aforementioned experiments delineated distinct adaptions in EP→LHb→VTA neural circuit in mice exposed to chronic mild stress. To further investigate the role of this subcircuit in depression related behaviors, we performed *in vivo* chemogenetic and optogenetic excitation and inhibition experiments targeting EP→LHb and LHb→VTA projections during EPM, SPT and TST. We observed that both EP→LHb and LHb→VTA subpopulations selectively modulated passive coping phenotype but not anxiety or anhedonia, while not affecting motor activity in OFT (**Figure 6 and S6A-D**). Moreover, LHb→VTA neuronal activation reduced motivated behavior, whereas activation EP→LHb pathway had no such effect (**Figure S6E-H**). That raises a possibility that LHb neurons targeted by EP terminals are not exactly the same LHb subpopulation projecting to the VTA or additional local LHb circuit mechanisms might control input / output of this nucleus. Our findings of EP→LHb→VTA pathway's involvement in passive coping and motivated behaviors are in agreement with previously published work. Yang et al. showed that rats exposed to chronic mild stress developed passive coping behavior as tested by forced swim test and that LHb lesions were able to rescue the phenotype (Yang et al., 2008). Furthermore, there is an upregulation βCaMKII in the LHb of animals displaying despair phenotype. Upregulation βCaMKII also promotes insertion of GluR2-lacing AMPAR subunits, a synaptic adaption we also observed at EP synapses onto LHb after stress. Overexpression or knock down of βCaMKII promoted or ameliorated passive coping phenotype, respectively (Li et al., 2013). Activation or inhibition of VP terminals in the LHb using optogenetics selecting promoted or rescued passive coping phenotype, respectively, but did not affect social interaction behavior (Knowland et al., 2017). Lastly, our results were corroborated by a study from Malinow's lab, where they both recorded and manipulated LHb→RMTg pathway during depression-related behaviors. By performing fiber photometry recordings from this population, they showed that the neuronal activity coincided with immobility bouts in the FST. Moreover, activating or inhibiting this pathway modulated despair behavior and motivation of rats, but did not affect hedonic phenotype in SPT (Proulx et al., 2018).

Finally, we performed single cell RNA sequencing from LHb→VTA neurons from animals displaying passive coping phenotype. We observed significant gene expression changes associated with cell adhesion molecules, ion channel function, transcription factors, and synaptic function (**Figures 7, S7, and S8**). We hope this database of transcriptomic changes in specific LHb subcircuit and associated with distinct depression-related behavior will promote future translational studies. We think one gene, *Kcnc1*, which codes for potassium channel Kv3.1, is of particular interest. First, *Kcnc1* was one the highest upregulated genes in LHb→VTA cells from animals with despair phenotype (**Figure 7I**). Second, Kv3.1 is selectively expressed in fast spiking neurons throughout the hippocampus and cortex (Weiser et al., 1995; Du et al., 1996; Chow et al., 1999). Third, Kv3.1 channels produce fast and large repolarization during action potential firing, which promotes Na+ channel recovery from inactivation and K+ channel deactivation, important physiological features to sustain high firing rates (Erisir et al., 1999). Lastly, expression of Kv3.1 channels in cultured neurons alone is enough to convert regular spiking neurons into fast spiking phenotype (Gu et al., 2018). Altogether, these and our studies suggest that overexpression of Kv3.1

in LHb→VTA neurons might be underlying their hyperactivity and lead to depression-like phenotypes. Cell-type-specific editing of such candidate genes may be a particularly fruitful approach toward understanding how molecular dysfunction gives rise to LHb hyperactivity and depression-related behaviors.

In summary, out study identifies a LHb subcircuit involved in chronic stress-induced increased passive coping and reduced motivated behaviors. Single-cell transcriptomics reveal potential gene targets associated with this specific behavioral phenotype. Identifying and targeting this and similar circuits can lead to breakthrough discoveries in depression research and generation of novel patient-tailored antidepressants.

BIBLIOGRAPHY

Agudelo, L.Z., Femenía, T., Orhan, F., Porsmyr-Palmertz, M., Goiny, M., Martinez-Redondo, V., Correia, J.C., Izadi, M., Bhat, M., Schuppe-Koistinen, I., et al. (2014). Skeletal muscle PGC-1α1 modulates kynurenine metabolism and mediates resilience to stress-induced depression. Cell *159*, 33–45.

Akil, H., Gordon, J., Hen, R., Javitch, J., Mayberg, H., McEwen, B., Meaney, M.J., and Nestler, E.J. (2018). Treatment resistant depression: A multi-scale, systems biology approach. Neurosci. Biobehav. Rev. *84*, 272–288.

Andalman, A.S., Burns, V.M., Lovett-Barron, M., Broxton, M., Poole, B., Yang, S.J., Grosenick, L., Lerner, T.N., Chen, R., Benster, T., et al. (2019). Neuronal Dynamics Regulating Brain and Behavioral State Transitions. Cell *177*, 970-985.e20.

Bagot, R.C., Cates, H.M., Purushothaman, I., Lorsch, Z.S., Walker, D.M., Wang, J., Huang, X., Schlüter, O.M., Maze, I., Peña, C.J., et al. (2016). Circuit-wide Transcriptional Profiling Reveals Brain Region-Specific Gene Networks Regulating Depression Susceptibility. Neuron *90*, 969–983.

Bernard, R., and Veh, R.W. (2012). Individual neurons in the rat lateral habenular complex project mostly to the dopaminergic ventral tegmental area or to the serotonergic raphe nuclei. J. Comp. Neurol. *520*, 2545–2558.

Berrar, D., and Flach, P. (2012). Caveats and pitfalls of ROC analysis in clinical microarray research (and how to avoid them). Brief. Bioinform. *13*, 83–97.

Berton, O. and Nestler, E. (2006) New approaches to antidepressant drug discovery: beyond monoamines. Nat. Rev. Neurosci. *7*, 137–151.

Berton, O., Hahn, C.G., and Thase, M.E. (2012). Are we getting closer to valid translational models for major depression? Science *338*, 75–79.

Brown, P.L., Palacorolla, H., Brady, D., Riegger, K., Elmer, G.I. and Shepard, P.D. (2017) Habenula-induced inhibition of midbrain dopamine neurons is diminished by lesions of the rostromedial tegmental nucleus. J. Neurosci. *37*, 217-225.

Can, A., Dao, D.T., Arad, M., Terrillion, C.E., Piantadosi, S.C., and Gould, T.D. (2012b). The mouse forced swim test. J. Vis. Exp. JoVE e3638.

Can, A., Dao, D.T., Terrillion, C.E., Piantadosi, S.C., Bhat, S., and Gould, T.D. (2012a). The tail suspension test. J. Vis. Exp. JoVE e3769.

Carragher, N., Adamson, G., Bunting, B., and McCann, S. (2009). Subtypes of depression in a nationally representative sample. J. Affect. Disord. *113*, 88–99.

Castagné, V., Moser, P., Roux, S., and Porsolt, R.D. (2011). Rodent models of depression: forced swim and tail suspension behavioral despair tests in rats and mice. Curr. Protoc. Neurosci. *Chapter 8*, Unit 8.10A.

Cho, J.-H., Deisseroth, K., and Bolshakov, V.Y. (2013). Synaptic Encoding of Fear Extinction in mPFC-amygdala Circuits. Neuron *80*, 1491–1507.

Chow, A., Erisir, A., Farb, C., Nadal, M.S., Ozaita, A., Lau, D., Welker, E. and Rudy B. (1999) K(+) channel expression distinguishes subpopulations of parvalbumin- and somatostatin-containing neocortical interneurons. J. Neurosci. *19*, 9332-45.

Clapham, D.E. (2007) Calcium signaling. Cell *131*, 1047-58.

Concha, M.L. and Wilson, S.W. (2001) Asymmetry in the epithalamus of vertebrates. J Anat. *199*, 63–84.

Cools, R., Nakamura, K. and Daw, N.D. (2011) Serotonin and dopamine: unifying affective, activational, and decision functions. Neuropsychopharmacology *36*, 98–113.

Cui, Y., Hu, S., and Hu, H. (2019). Lateral Habenular Burst Firing as a Target of the Rapid Antidepressant Effects of Ketamine. Trends Neurosci. *42*, 179–191.

Cui, Y., Yang, Y., Ni, Z., Dong, Y., Cai, G., Foncelle, A., Ma, S., Sang, K., Tang, S., Li, Y., et al. (2018). Astroglial Kir4.1 in the lateral habenula drives neuronal bursts in depression. Nature *554*, 323–327.

Czéh, B., Fuchs, E., Wiborg, O., and Simon, M. (2016). Animal models of major depression and their clinical implications. Prog. Neuropsychopharmacol. Biol. Psychiatry *64*, 293–310.

Dafny, N. and Qiao, J.T. (1990) Habenular neuron responses to noxious input are modified by dorsal raphe stimulation. Neurol. Res. *12*, 117–121.

Delgado, P.L. (2000) Depression: The Case for a Monoamine Deficiency. J Clin Psychiatry *61*, 7-11.

Drysdale, A.T., Grosenick, L., Downar, J., Dunlop, K., Mansouri, F., Meng, Y., Fetcho, R.N., Zebley, B., Oathes, D.J., Etkin, A., et al. (2017). Resting-state connectivity biomarkers define neurophysiological subtypes of depression. Nat. Med. *23*, 28–38.

Du, J., Zhang, L., Weiser, M., Rudy, B. and McBain, C.J. (1996) Developmental expression and functional characterization of the potassium-channel subunit Kv3.1b in parvalbumin-containing interneurons of the rat hippocampus. J. Neurosci. *16*, 506-18.

Erisir, A., Lau, D., Rudy, B. and Leonard, C.S. (1999) Function of specific K(+) channels in sustained high-frequency firing of fast-spiking neocortical interneurons. J. Neurophysiol. 82, 2476-89.

Fergusson, J. M. (2001) SSRI Antidepressant Medications: Adverse Effects and Tolerability. Prim. Care Companion .J Clin. Psychiatry *3*, 22–27.

Flanigan, M.E., Aleyasin, H., Li, L., Burnett, C.J., Chan, K.L., LeClair, K.B., Lucas, E.K., Matikainen-Ankney, B., Janssen, W., Takahashi, A., Menard, C., Pfau, M.L., Golden, S.A., Bouchard, S., Calipari, E.S., Nestler, E.J., DiLeone, R.J., Yamanaka, A., Huntley, G.W., Clem,

R.L. and Russo, S.J. (2019) Orexin signaling in GABAergic lateral habenula neurons modulates aggressive behavior. bioRxiv *811265*.

Földy, C., Darmanis, S., Aoto, J., Malenka, R.C., Quake, S.R., and Südhof, T.C. (2016). Single-cell RNAseq reveals cell adhesion molecule profiles in electrophysiologically defined neurons. Proc. Natl. Acad. Sci. U. S. A. *113*, E5222-5231.

Franklin, K.B.J., and Paxinos, G. (2013). Paxinos and Franklin's The mouse brain in stereotaxic coordinates (Amsterdam: Academic Press, an imprint of Elsevier).

Fried, E. (2017) Moving forward: how depression heterogeneity hinders progress in treatment and research. Expert Rev. Neurother. *17*, 423-425.

Frisbee, J.C., Brooks, S.D., Stanley, S.C., and d'Audiffret, A.C. (2015). An Unpredictable Chronic Mild Stress Protocol for Instigating Depressive Symptoms, Behavioral Changes and Negative Health Outcomes in Rodents. J. Vis. Exp. JoVE.

Golden, S.A., Heshmati, M., Flanigan, M., Christoffel, D.J., Guise, K., Pfau, M.L., Aleyasin, H., Menard, C., Zhang, H., Hodes, G.E., Bregman, D., Khibnik, L., Tai, J., Rebusi, N., Krawitz, B, Chaudhury, D., Walsh, J.J., Han, M.H., Shapiro, M.L., Russo, S.J. (2016) Basal forebrain projections to the lateral habenula modulate aggression reward. Nature *534*, 688–692.

Good, C.H., Wang, H., Chen, Y.H., Mejias-Aponte, C.A., Hoffman, A.F. and Lupica, C.R. (2013) Dopamine D4 receptor excitation of lateral habenula neurons via multiple cellular mechanisms. J. Neurosci. *43*, 16853–16864.

Gourévitch, B., and Eggermont, J.J. (2007). A nonparametric approach for detection of bursts in spike trains. J. Neurosci. Methods *160*, 349–358.

Groth, R.D., Lindskog, M., Thiagarajan, T.C., Li, L. and Tsien, R.W. (2011) Beta Ca2+/CaM-dependent kinase type II triggers upregulation of GluA1 to coordinate adaptation to synaptic inactivity in hippocampal neurons. Proc. Natl. Acad. Sci. *108*, 828-33.

Gruber, C., Kahl, A., Lebenheim, L., Kowski, A., Dittgen, A. and Veh, R.W. (2007) Dopaminergic projections from the VTA substantially contribute to the mesohabenular pathway in the rat. Neurosci. Lett. *427*, 165–170.

Gu, Y., Servello, D., Han, Z., Lalchandani, R.R., Ding, J.B., Huang, K. and Gu, C. (2018) Balanced Activity between Kv3 and Nav Channels Determines Fast-Spiking in Mammalian Central Neurons. iScience. *9*, 120-137.

Herkenham, M., and Nauta, W.J. (1977). Afferent connections of the habenular nuclei in the rat. A horseradish peroxidase study, with a note on the fiber-of-passage problem. J. Comp. Neurol. *173*, 123–146.

Hikosaka, O., Sesack, S.R., Lecourtier, L., and Shepard, P.D. (2008). Habenula: Crossroad between the Basal Ganglia and the Limbic System. J. Neurosci. *28*, 11825–11829.

Hill, M.N., Hellemans, K.G.C., Verma, P., Gorzalka, B.B., and Weinberg, J. (2012). Neurobiology of chronic mild stress: parallels to major depression. Neurosci. Biobehav. Rev. *36*, 2085–2117.

Hirschfeld, R.M.A (2000) History and Evolution of the Monoamine Hypothesis of Depression. J Clin. Psychiatry *61*, 4-6.

Hodos, W. (1961). Progressive ratio as a measure of reward strength. Science *134*, 943–944.

Hollmann, M., Hartley, M., and Heinemann, S. (1991). Ca2+ permeability of KA-AMPA--gated glutamate receptor channels depends on subunit composition. Science *252*, 851–853.

Hong, S., and Hikosaka, O. (2008) The globus pallidus sends reward-related signals to the lateral habenula. Neuron *60*, 720–729.

Jennings, J.H., Rizzi, G., Stamatakis, A.M., Ung, R.L. and Stuber, G.D. (2013) The inhibitory circuit architecture of the lateral hypothalamus orchestrates feeding. Science *341*, 1517–1521.

Jhou, T.C., Fields, H.L., Baxter, M.G., Saper, C.B., and Holland, P.C. (2009). The Rostromedial Tegmental Nucleus (RMTg), a GABAergic Afferent to Midbrain Dopamine Neurons, Encodes Aversive Stimuli and Inhibits Motor Responses. Neuron *61*, 786–800.

Jhou, T.C., Good, C.H., Rowley, C.S., Xu, S.P., Wang, H., Burnham, N.W., Hoffman, A.F., Lupica, C.R. and Ikemoto, S. (2013) Cocaine drives aversive conditioning via delayed activation of dopamine-responsive habenular and midbrain pathways. J. Neurosci. *33*, 7501-7512.

Kaufling, J., Veinante, P., Pawlowski, S.A., Freund-Mercier, M.J., and Barrot, M. (2009). Afferents to the GABAergic tail of the ventral tegmental area in the rat. J Comp Neurol *513*, 597–621.

Kiening, K., and Sartorius, A. (2013). A new translational target for deep brain stimulation to treat depression: A new target for DBS to treat depression. EMBO Mol. Med. *5*, 1151–1153.

Kim, U. and Lee, T. (2012) Topography of descending projections from anterior insular and medial prefrontal regions to the lateral habenula of the epithalamus in the rat. Eur J Neurosci. *35*, 1253-69.

Kim, U., and Chang, S.-Y. (2005). Dendritic morphology, local circuitry, and intrinsic electrophysiology of neurons in the rat medial and lateral habenular nuclei of the epithalamus. J. Comp. Neurol. *483*, 236–250.

Knowland, D., Lilascharoen, V., Pacia, C.P., Shin, S., Wang, E.H.-J., and Lim, B.K. (2017). Distinct Ventral Pallidal Neural Populations Mediate Separate Symptoms of Depression. Cell *170*, 284-297.e18.

Koolhaas, J.M., Korte, S.M., De Boer, S.F., Van Der Vegt, B.J., Van Reenen, C.G., Hopster, H., De Jong, I.C., Ruis, M.A., and Blokhuis, H.J. (1999). Coping styles in animals: current status in behavior and stress-physiology. Neurosci. Biobehav. Rev. *23*, 925–935.

Krishnan, V., Han, M.-H., Graham, D.L., Berton, O., Renthal, W., Russo, S.J., Laplant, Q., Graham, A., Lutter, M., Lagace, D.C., et al. (2007). Molecular adaptations underlying susceptibility and resistance to social defeat in brain reward regions. Cell *131*, 391–404.

Lammel, S., Lim, B.K., Ran, C., Huang, K.W., Betley, M.J., Tye, K.M., Deisseroth, K., and Malenka, R.C. (2012). Input-specific control of reward and aversion in the ventral tegmental area. Nature *491*, 212–217.

Lammel, S., Steinberg, E.E., Földy, C., Wall, N.R., Beier, K., Luo, L. and Malenka, R.C. (2015) Diversity of transgenic mouse models for selective targeting of midbrain dopamine neurons. Neuron *85*, 429-38.

Lammel, S., Tye, K.M., and Warden, M.R. (2014). Progress in understanding mood disorders: optogenetic dissection of neural circuits. Genes Brain Behav. *13*, 38–51.

Lecca, S., Meye, F.J., and Mameli, M. (2014). The lateral habenula in addiction and depression: an anatomical, synaptic and behavioral overview. Eur. J. Neurosci. *39*, 1170–1178.

Lecca, S., Pelosi, A., Tchenio, A., Moutkine, I., Lujan, R., Hervé, D., and Mameli, M. (2016). Rescue of GABAB and GIRK function in the lateral habenula by protein phosphatase 2A inhibition ameliorates depression-like phenotypes in mice. Nat. Med. *22*, 254–261.

Li, B., Piriz, J., Mirrione, M., Chung, C., Proulx, C.D., Schulz, D., Henn, F., and Malinow, R. (2011). Synaptic potentiation onto habenula neurons in the learned helplessness model of depression. Nature *470*, 535–539.

Li, K., Zhou, T., Liao, L., Yang, Z., Wong, C., Henn, F., Malinow, R., Yates, J.R., and Hu, H. (2013). βCaMKII in lateral habenula mediates core symptoms of depression. Science *341*, 1016–1020.

Liu, S.J., and Zukin, R.S. (2007). Ca2+-permeable AMPA receptors in synaptic plasticity and neuronal death. Trends Neurosci. *30*, 126–134.

Lun, A.T.L., McCarthy, D.J., and Marioni, J.C. (2016). A step-by-step workflow for low-level analysis of single-cell RNA-seq data with Bioconductor. F1000Research *5*, 2122.

Matsumoto, M. and Hikosaka, O. (2007) Lateral habenula as a source of negative reward signals in dopamine neurons. Nature *447*, 1111–1115.

Matsumoto, N., Yahata, F., Kawarada, K., Kamata, K. and Suzuki, T.A. (1994)Tooth pulp stimulation induces c-fos expression in the lateral habenular nucleus of the cat. Neuroreport *5*, 2397–2400.

Mazure, C.M., and Maciejewski, P.K. (2003). A model of risk for major depression: effects of life stress and cognitive style vary by age. Depress. Anxiety *17*, 26–33.

Meng, H., Wang, Y., Huang, M., Lin, W., Wang, S. and Zhang, B. (2011) Chronic deep brain stimulation of the lateral habenula nucleus in a rat model of depression. Brain Res. *8*, 32-8.

Metz, C.E. (1978). Basic principles of ROC analysis. Semin. Nucl. Med. *8*, 283–298.

Mirrione, M.M., Schulz, D., Lapidus, K.A.B., Zhang, S., Goodman, W., and Henn, F.A. (2014). Increased metabolic activity in the septum and habenula during stress is linked to subsequent expression of learned helplessness behavior. Front. Hum. Neurosci. *8*, 29.

Monteggia, L.M., Heimer, H., and Nestler, E.J. (2018). Meeting Report: Can We Make Animal Models of Human Mental Illness? Biol. Psychiatry *84*, 542–545.

Moreines, J.L., Owrutsky, Z.L., and Grace, A.A. (2017). Involvement of Infralimbic Prefrontal Cortex but not Lateral Habenula in Dopamine Attenuation After Chronic Mild Stress. Neuropsychopharmacology *42*, 904–913.

Morris, J.S., Smith, K.A., Cowen, P.J., Friston, K.J. and Dolan, R.J. (1999) Covariation of activity in habenula and dorsal raphé nuclei following tryptophan depletion. Neuroimage. *10*, 163-72.

Musil, R., Seemüller, F., Meyer, S., Spellmann, I., Adli, M., Bauer, M., Kronmüller, K.-T., Brieger, P., Laux, G., Bender, W., et al. (2018). Subtypes of depression and their overlap in a naturalistic inpatient sample of major depressive disorder. Int. J. Methods Psychiatr. Res. *27*, e1569.

Nestler, E.J., and Carlezon, W.A. (2006). The Mesolimbic Dopamine Reward Circuit in Depression. Biol. Psychiatry *59*, 1151–1159.

Nestler, E.J., and Hyman, S.E. (2010). Animal models of neuropsychiatric disorders. Nat. Neurosci. *13*, 1161–1169.

Osakada, F., and Callaway, E.M. (2013). Design and generation of recombinant rabies virus vectors. Nat. Protoc. *8*, 1583–1601.

Petreanu, L., Mao, T., Sternson, S.M., and Svoboda, K. (2009). The subcellular organization of neocortical excitatory connections. Nature *457*, 1142–1145.

Pittenger, C., and Duman, R.S. (2008). Stress, depression, and neuroplasticity: a convergence of mechanisms. Neuropsychopharmacol. Off. Publ. Am. Coll. Neuropsychopharmacol. *33*, 88–109.

Poller, W.C., Madai, V.I., Bernard, R., Laube, G. and Veh, R.W. (2013) A glutamatergic projection from the lateral hypothalamus targets VTA-projecting neurons in the lateral habenula of the rat. Brain Res. *1507*, 45–60.

Porsolt, R.D., Bertin, A., and Jalfre, M. (1978). "Behavioural despair" in rats and mice: strain differences and the effects of imipramine. Eur. J. Pharmacol. *51*, 291–294.

Proulx, C.D., Aronson, S., Milivojevic, D., Molina, C., Loi, A., Monk, B., Shabel, S.J., and Malinow, R. (2018). A neural pathway controlling motivation to exert effort. Proc. Natl. Acad. Sci. *115*, 5792–5797.

Proulx, C.D., Hikosaka, O., and Malinow, R. (2014). Reward processing by the lateral habenula in normal and depressive behaviors. Nat. Neurosci. *17*, 1146–1152.

Quina, L.A., Tempest, L., Ng, L., Harris, J.A., Ferguson, S., Jhou, T.C. and Turner, E.E. (2014) Efferent pathways of the mouse lateral habenula. J. Comp. Neurol. *523*, 32-60.

Ramirez, S., Liu, X., MacDonald, C.J., Moffa, A., Zhou, J., Redondo, R.L., and Tonegawa, S. (2015). Activating positive memory engrams suppresses depression-like behaviour. Nature *522*, 335–339.

Richardson, N.R., and Roberts, D.C. (1996). Progressive ratio schedules in drug self-administration studies in rats: a method to evaluate reinforcing efficacy. J. Neurosci. Methods *66*, 1–11.

Root, D.H., Mejias-Aponte, C.A., Qi, J. and Morales, M. (2014) Role of glutamatergic projections from ventral tegmental area to lateral habenula in aversive conditioning. J. Neurosci. *34*, 13906-10.

Root, D.H., Mejias-Aponte, C.A., Zhang, S., Wang, H.L., Hoffman, A.F., Lupica, C.R. and Morales, M. (2014) Single rodent mesohabenular axons release glutamate and GABA. Nat. Neurosci. *17*, 1543–1551.

Rush, A.J. (2007) STAR*D: What Have We Learned? Am. J. Psychiatry *164*, 2.

Sartorius, A., and Henn, F.A. (2007). Deep brain stimulation of the lateral habenula in treatment resistant major depression. Med. Hypotheses *69*, 1305–1308.

Sartorius, A., Kiening, K.L., Kirsch, P., von Gall, C.C., Haberkorn, U., Unterberg, A.W., Henn, F.A., and Meyer-Lindenberg, A. (2010). Remission of major depression under deep brain stimulation of the lateral habenula in a therapy-refractory patient. Biol. Psychiatry *67*, e9–e11.

Schultz, W. (2016) Dopamine reward prediction error coding. Dialogues Clin. Neurosci. *18*, 23–32.

Schweizer, M.C., Henniger, M.S.H., and Sillaber, I. (2009). Chronic Mild Stress (CMS) in Mice: Of Anhedonia, 'Anomalous Anxiolysis' and Activity. PLoS ONE *4*, e4326.

Sego, C., Gonçalves, L., Lima, L., Furigo, I.C., Donato, J. Jr and Metzger, M. (2013) Lateral habenula and the rostromedial tegmental nucleus innervate neurochemically distinct subdivisions of the dorsal raphe nucleus in the rat. J. Comp. Neurol. *522*, 1454-84.

Seo, J.-S., Zhong, P., Liu, A., Yan, Z., and Greengard, P. (2018). Elevation of p11 in lateral habenula mediates depression-like behavior. Mol. Psychiatry *23*, 1113–1119.

Shabel, S.J., Proulx, C.D., Piriz, J., and Malinow, R. (2014). GABA/glutamate co-release controls habenula output and is modified by antidepressant treatment. Science *345*, 1494–1498.

Shabel, S.J., Proulx, C.D., Trias, A., Murphy, R.T. and Malinow R (2012) Input to the lateral habenula from the basal ganglia is excitatory, aversive, and suppressed by serotonin. Neuron *74*, 475

Shumake, J., Edwards, E., and Gonzalez-Lima, F. (2003). Opposite metabolic changes in the habenula and ventral tegmental area of a genetic model of helpless behavior. Brain Res. *963*, 274–281.

Søreide, K. (2009). Receiver-operating characteristic curve analysis in diagnostic, prognostic and predictive biomarker research. J. Clin. Pathol. *62*, 1–5.

Stamatakis, A.M., and Stuber, G.D. (2012). Activation of lateral habenula inputs to the ventral midbrain promotes behavioral avoidance. Nat Neurosci *15*, 1105–1107.

Stamatakis, A.M., Jennings, J.H., Ung, R.L., Blair, G.A., Weinberg, R.J., Neve, R.L., Boyce, F., Mattis, J., Ramakrishnan, C., Deisseroth, K. and Stuber, G.D. (2013) A unique population of ventral tegmental area neurons inhibits the lateral habenula to promote reward. Neuron *4*, 1039–1053-81.

Stamatakis, A.M., Van Swieten, M., Basiri, M.L., Blair, G.A., Kantak, P. and Stuber G.D. (2016) Lateral Hypothalamic Area Glutamatergic Neurons and Their Projections to the Lateral Habenula Regulate Feeding and Reward. J. Neurosci. *36*, 302-11.

Stephenson-Jones, M., Yu, K., Ahrens, S., Tucciarone, J.M., van Huijstee, A.N., Mejia, L.A., Penzo, M.A., Tai, L.H., Wilbrecht, L and Li, B. (2016) A basal ganglia circuit for evaluating action outcomes. Nature *539*, 289-293.

Südhof, T.C. (2012) Calcium control of neurotransmitter release. Cold Spring Harb. Perspect. Biol. *4*, a011353.

Swets, J.A. (1988). Measuring the Accuracy of Diagnostic Systems. Sci. New Ser. *240*, 1285–1293.

Tchenio, A., Lecca, S., Valentinova, K., and Mameli, M. (2017). Limiting habenular hyperactivity ameliorates maternal separation-driven depressive-like symptoms. Nat. Commun. *8*, 1135.

Tchenio, A., Valentinova, K. and Mameli, M. (2016) Can the Lateral Habenula Crack the Serotonin Code? Front Synaptic Neurosci. *8*, 34.

ten Have, M., Lamers, F., Wardenaar, K., Beekman, A., de Jonge, P., van Dorsselaer, S., Tuithof, M., Kleinjan, M., and de Graaf, R. (2016). The identification of symptom-based subtypes of depression: A nationally representative cohort study. J. Affect. Disord. *190*, 395–406.

Thase, M.E. and Schwartz T.L. (2015) Choosing medications for treatment-resistant depression based on mechanism of action. J Clin. Psychiatry *76*, 720-7.

Thompson, S.M., Kallarackal, A.J., Kvarta, M.D., Van Dyke, A.M., LeGates, T.A., and Cai, X. (2015). An excitatory synapse hypothesis of depression. Trends Neurosci. *38*, 279–294.

Tye, K.M., Mirzabekov, J.J., Warden, M.R., Ferenczi, E.A., Tsai, H.-C., Finkelstein, J., Kim, S.-Y., Adhikari, A., Thompson, K.R., Andalman, A.S., et al. (2012). Dopamine neurons modulate neural encoding and expression of depression-related behaviour. Nature *493*, 537–541.

Tye, K.M., Prakash, R., Kim, S.Y., Fenno, L.E., Grosenick, L., Zarabi, H., Thompson, K.R., Gradinaru, V., Ramakrishnan, C., and Deisseroth, K. (2011). Amygdala circuitry mediating reversible and bidirectional control of anxiety. Nature *471*, 358–362.

Ullsperger, M. and von Cramon, D. Y. (2003) Error monitoring using external feedback: specific roles of the habenular complex, the reward system, and the cingulate motor area revealed by functional magnetic resonance imaging. J. Neurosci. *23*, 4308–4314.

van Loo, H.M., de Jonge, P., Romeijn, J.-W., Kessler, R.C., and Schoevers, R.A. (2012). Data-driven subtypes of major depressive disorder: a systematic review. BMC Med. *10*.

Viswanath H., Carter A.Q., Baldwin P.R., Molfese D.L. and Salas R. (2014) The medial habenula: still neglected. Front. Hum. Neurosci. *7*, 931.

Wallace, M.L., Saunders, A., Huang, K.W., Philson, A.C., Goldman, M., Macosko, E.Z., McCarroll, S.A., and Sabatini, B.L. (2017). Genetically Distinct Parallel Pathways in the Entopeduncular Nucleus for Limbic and Sensorimotor Output of the Basal Ganglia. Neuron *94*, 138-152.e5.

Wang, R.Y. and Aghajanian, G.K. (1977) Physiological evidence for habenula as major link between forebrain and midbrain raphe. Science *197*, 89–91.

Warden, M.R., Selimbeyoglu, A., Mirzabekov, J.J., Lo, M., Thompson, K.R., Kim, S.-Y., Adhikari, A., Tye, K.M., Frank, L.M., and Deisseroth, K. (2012). A prefrontal cortex-brainstem neuronal projection that controls response to behavioural challenge. Nature *492*, 428–432.

Waters, A.C., and Mayberg, H.S. (2017). Brain-Based Biomarkers for the Treatment of Depression: Evolution of an Idea. J. Int. Neuropsychol. Soc. *23*, 870–880.

Weiser, M., Bueno, E., Sekirnjak, C., Martone, M.E., Baker, H., Hillman, D., Chen, S., Thornhill, W., Ellisman, M. and Rudy, B. (1995) The potassium channel subunit KV3.1b is localized to somatic and axonal membranes of specific populations of CNS neurons. J. Neurosci. *15*, 4298-314.

Weiss, T., and Veh, R.W. (2011). Morphological and electrophysiological characteristics of neurons within identified subnuclei of the lateral habenula in rat brain slices. Neuroscience *172*, 74–93.

Willner, P. (1997) Validity, reliability and utility of the chronic mild stress model of depression: a 10-year review and evaluation. Psychopharmacology *134*, 319-29

Willner, P. (2005). Chronic mild stress (CMS) revisited: consistency and behavioural-neurobiological concordance in the effects of CMS. Neuropsychobiology *52*, 90–110.

Willner, P. (2017). The chronic mild stress (CMS) model of depression: History, evaluation and usage. Neurobiol. Stress *6*, 78–93.

Willner, P., Muscat, R., and Papp, M. (1992). Chronic mild stress-induced anhedonia: A realistic animal model of depression. Neurosci. Biobehav. Rev. *16*, 525–534.

Willner, P., Scheel-Krüger, J., and Belzung, C. (2013). The neurobiology of depression and antidepressant action. Neurosci. Biobehav. Rev. *37*, 2331–2371.

Winter, C., Vollmayr, B., Djodari-Irani, A., Klein, J. and Sartorius A. (2011) Pharmacological inhibition of the lateral habenula improves depressive-like behavior in an animal model of treatment resistant depression. Behav. Brain Res. *216*, 463-5.

Wise, R.A. (2004) Dopamine, learning and motivation. Nat. Rev. Neurosci. *5*, 483–494.

Yang, L.-M., Hu, B., Xia, Y.-H., Zhang, B.-L., and Zhao, H. (2008). Lateral habenula lesions improve the behavioral response in depressed rats via increasing the serotonin level in dorsal raphe nucleus. Behav. Brain Res. *188*, 84–90.

Yang, L.M., Yu, L., Jin, H.J. and Zhao, H. (2014) Substance P receptor antagonist in lateral habenula improves rat depression-like behavior. Brain Res. Bull. *100*, 22-8.

Yang, Y., Cui, Y., Sang, K., Dong, Y., Ni, Z., Ma, S., and Hu, H. (2018). Ketamine blocks bursting in the lateral habenula to rapidly relieve depression. Nature *554*, 317–322.

Yang, Y., Wang, H., Hu, J. and Hu, H. (2018) Lateral habenula in the pathophysiology of depression. Curr Opin Neurobiol. *48*, 90-96.

Yang, Y., Wang, H., Hu, J., and Hu, H. (2017). Lateral habenula in the pathophysiology of depression. Curr. Opin. Neurobiol. *48*, 90–96.

Yilmaz, A., Schulz, D., Aksoy, A., and Canbeyli, R. (2002). Prolonged effect of an anesthetic dose of ketamine on behavioral despair. Pharmacol. Biochem. Behav. *71*, 341–344.

Youden, W.J. (1950). Index for rating diagnostic tests. Cancer *3*, 32–35.

Zhang, L., Hernández, V.S., Swinny, J.D., Verma, A.K., Giesecke, T., Emery, A.C., Mutig, K., Garcia-Segura, L.M. and Eiden, L.E. (2018) A GABAergic cell type in the lateral habenula links hypothalamic homeostatic and midbrain motivation circuits with sex steroid signaling. Transl Psychiatry *8*, 50.

Zhang, S.-J., Ye, J., Miao, C., Tsao, A., Cerniauskas, I., Ledergerber, D., Moser, M.-B., and Moser, E.I. (2013). Optogenetic dissection of entorhinal-hippocampal functional connectivity. Science *340*, 1232627.

Zhou, L., Liu, M.Z., Li, Q., Deng, J., Mu, D. and Sun, Y.G. (2017) Organization of functional long-range circuits controlling the activity of serotonergic neurons in the dorsal raphe nucleus. Cell Rep. *18*, 3018-3032.

Zou, K.H., O'Malley, A.J., and Mauri, L. (2007). Receiver-Operating Characteristic Analysis for Evaluating Diagnostic Tests and Predictive Models. Circulation *115*, 654–657.

Zweig, M.H., and Campbell, G. (1993). Receiver-operating characteristic (ROC) plots: a fundamental evaluation tool in clinical medicine. Clin. Chem. *39*, 561–577.